Design and heat treatment of 3D printed spinal cages

Erik Smedes

Master thesis
A colaboration with Amber Implants

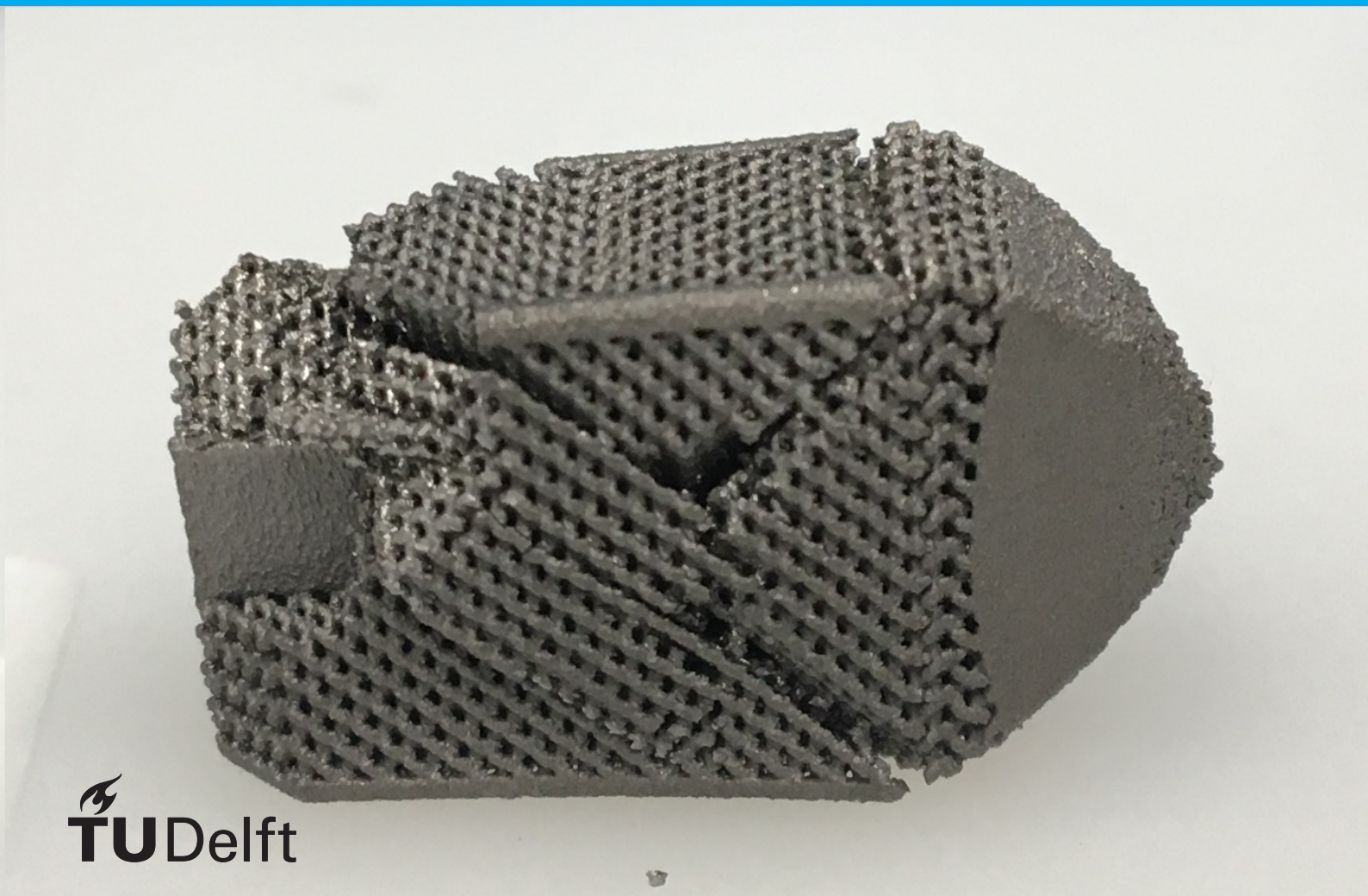

TU Delft

Design and heat treatment of 3D printed spinal cages

by

Erik Smedes

to obtain the degree of Master of Science
at the Delft University of Technology,
to be defended publicly on Thursday September 10, 2020 at 01:00 PM.

Student number:	4262492	
Project duration:	July, 2019 – September, 2020	
Thesis committee:	Dr. J. Zhou,	TU Delft, supervisor
	Dr. V. Popovich,	TU Delft, supervisor
	Dr. C. D. Rans,	TU Delft
	Ir. P. Pellikaan,	Amber Implants

An electronic version of this thesis is available at http://repository.tudelft.nl/.

TU Delft

Abstract

Back pain and back instability affect close to 80% of the population at some point during their life. One solution is to insert a spinal cage, which results in spinal fusion, meaning two vertebrae fuse together to create one big vertebra. This study focuses on the investigation of both the processing aspects as the design aspects of producing a functional spinal cage.

The spinal cage investigated is made of 3D printed Ti6Al4V using selective laser melting (SLM). The original design showed some undesirable qualities, which are a higher apparent Young's modulus compared to the surrounding bone, causing stress shielding; and the creation of high stress concentrations due to the implant design, which reduces the fatigue life. A new design is created and tested using a combination of FEM software and mechanical testing. Comparing the new spinal cage to the original spinal cage it was found that the Young's modulus is 4 times lower; the yield strength 27% lower, but does not yield when a force of 4 kN is applied as required; and the fatigue life 2.2 times higher.

Currently, implants are post treated using hot isostatic pressing (HIP), which is an expensive procedure. One of the objectives of this research is to investigate the effectiveness of a vacuum oven as an alternative heat treatment method. This is done with SLM 3D printed Ti6Al4V samples with a porosity of 59%, which are heat treated at 850 and 1050 °C for 2 hours. When comparing the vacuum heat treatment performed at 1050 with 850 °C, the α grain thickness is increased 2.8 times, the Young's modulus with 13% and the yield strength with 7%. The vacuum heat treatments increase the fatigue life with 20% due to the removal of residual stresses and the transformation of the 'α-martensite to an α + β microstructure as is required. Between the two heat treatments no significant difference in fatigue life is found. Comparing the fatigue life of the vacuum heat treatments with HIP at 920 °C for 2 hours, it was observed that at 10,000 cycles the fatigue life of HIP is 20% better and at 1,000,000 cycles 1% worse. The main difference between the heat treatments is the reduction of internal pore size after HIP. The internal porosity affects the fatigue life. However, the effect of internal porosity will reduce faster compared to the effect of surface quality resulting in a similar fatigue life at high cycle fatigue. For spinal cages high cycle fatigue is more interesting to look at.

Finally, commercial spinal implants are universally designed based on the requirements and life-style of a 30 year old male. In order to improve the success-rate of spinal fusion, more patient-specific implants can be designed and produced using additive manufacturing. In this research five different patient specific groups are defined based on expected load and bone density. Using these requirements five different spinal cages are designed based on different porosities. Using FEM software the minimum apparent Young's modulus which can be achieved for every patient group is found. The apparent Young's modulus found for every group ranges between 1.40 and 3.17 GPa. Finally, the fatigue graph and apparent Young's modulus obtained from the mechanical tests are used to validate the simulation. The simulated fatigue life was around three times lower compared to the actual fatigue life and the apparent Young's modulus was 6.3% higher compared to the actual apparent Young's modulus. These findings are used to correct the simulations and the new apparent Young's modulus for every patient group lies between 1.32 and 2.98 GPa which is even closer to the Young's modulus of the surrounding bone.

Contents

Nomenclature

Symbols

$\Delta\sigma_w$	Stress threshold
ΔK_{th}	Crack propagation threshold
δ	Deformation
ϵ	Strain
μ	Expected average
$\overline{X}$	Measured average
ρ	Density
σ	Stress
σ_y	Yield stress
θ	angle between strut and horizontal plane
A	Area
a	Unit cell size
D	Diameter of sample
d	Grainsize
d	Strut diameter
E	Young's modulus
F	Force
I	Moment of inertia
k	Stiffness
L	Strut length
M	Bending moment
m	Mass
N	Number of cycles
n	Number of nodes
V	Volume

Abbreviations

AC Air cooling

AM Additive manufacturing

AP As-processed

CE Chemical etching

CRF-PEEK Carbon-fibre-reinforced polyether ether ketone

EBM Electron beam melting

ED Electron deposition

ELI Extra low interstitials

FC Furnace cooling

FDA Food and Drug Administration

FEM Finite element method

HCF High cycle fatigue

HIP Hot isostatic pressing

LCF Low cycle fatigue

MSC Mesenchymal stem cell

PBF Powder bed fusion

PEEK Polyether ether ketone

PLIF Posterior lumber inter-body fusion

POM Polyoxymethylene

SB Sandblasting

SD Standard deviation

SEM Scanning electron microscope

SLM Selective laser melting

UTS Ultimate tensile strength

WQ Water quenching

XLIF eXtreme lateral inter-body fusion

XRD X-ray diffraction

List of Figures

List of Tables

1

Introduction

Back pain and back instability affect close to 80% of the population at some time during their life. The three main causes of back pain and instability are fracture, excessive motion between vertebrae and spondylosis. There are many possibilities to treat back pain, such as placing an artificial disc or a more innovative method involving stem cell therapy [92]. However, this study focuses on the use of a spinal cage in order to treat back pain and back instability. A spinal cage can be used to perform a spinal fusion, in which two vertebrae fuse together to create one new vertebra. During this procedure parts of the spinal disc are removed and one or multiple spinal cages are inserted between the vertebrae. Finally, the vertebrae are fixed together with two rods to add stability as shown in Figure 1.1.

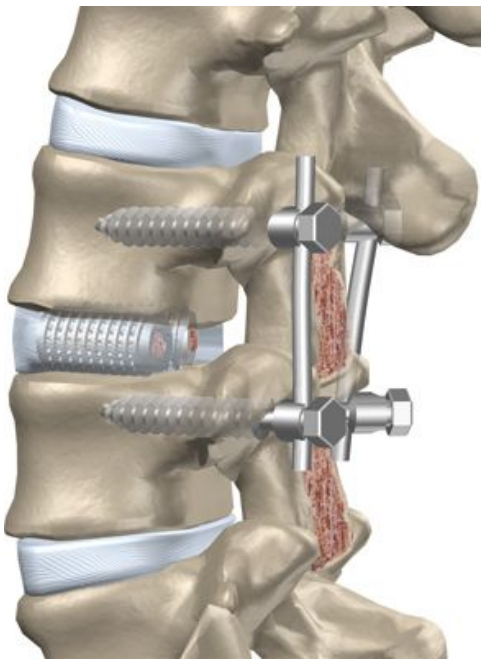

Figure 1.1: Simulated images of a spinal cage implantation [1].

There are different types of spinal cages, of which posterior lumbar inter-body fusion (PLIF) spinal cages are most common [68]. PLIF involves the spine being approached from the back, and is often performed on the lower spine. The spinal cage itself can be made from a porous material which bone can grow into, or use allo and auto grafts or a combination in order to

support bone formation. In Figure 1.2 a few examples of different types of PLIF spinal cages are given.

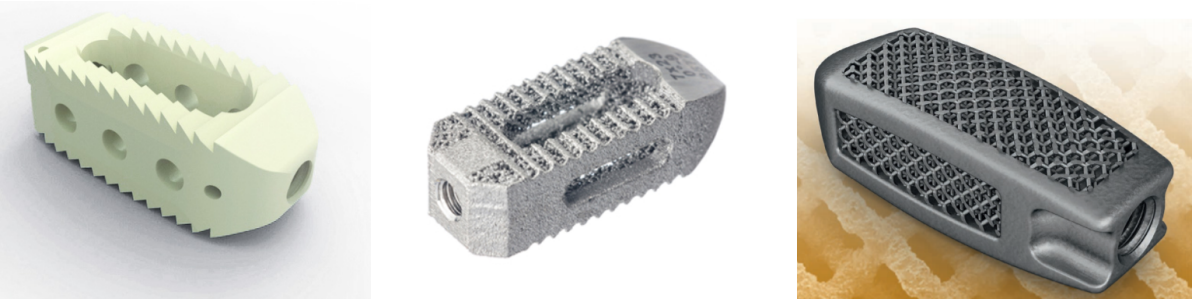

Figure 1.2: PLIF spinal cage using (a) allo or auto grafts for spinal fusion [64], (b) allo or auto grafts and a porous structure for spinal fusion [82] and (b) a porous structure for spinal fusion [26].

In order to design and manufacture a spinal cage, there are different aspects to consider. Firstly, it is important to prevent failure of the implant at all costs, because of the damage this can cause to vital parts of the body. One way failure can occur is when a large load is applied, breaking the implant at its weakest point. Another way is caused by a lower cyclic load. This will not lead to instant failure, but each loading cycle incrementally damages the implant. During these loading cycles cracks will form at high stress concentration in the implant, and will grow, leading eventually to the failure of the implant.

Apart from the strength of the implant, the apparent Young's modulus of the implant is important to consider. The apparent Young's modulus is defined as the measured Young's modulus which can be different compared to the true Young's modulus in for example porous structures [93]. A high apparent Young's modulus compared to natural bone causes stress shielding at the bone-implant interface, which leads to bone-resorption and eventually failure of the bone [41]. 3D printing gives the possibility to create complex porous structures, which lowers the apparent Young's modulus of the implant and allows bone to grow into the material. Unfortunately, many spinal cages still consist of big solid parts which are meant to strengthen the spinal cage, but often cause large stress concentrations and stress shielding [11]. Stress shielding occurs when most of the load is carried by the strong solid material and not by the porous material. New bone formation is stimulated by stress applied on the surrounding bone. When no stress is applied on the porous material the bone is not stimulated to grow into the porous structure. This reduces the success rate of spinal fusion. It is therefore important to find the optimal balance between strength and apparent Young's modulus in order to improve the fatigue life and the success rate of spinal fusion.

Secondly, currently during the production process of a spinal cage a heat treatment is applied which is called hot isostatic pressing (HIP). This is a very effective heat treatment for 3D printed materials, because it occurs in an inert environment and under pressure. This means limited oxidation will occur and internal pores created during 3D printing will reduce in size [71]. This heat treatment has been so effective that not much research is conducted for alternative heat treatments. However, HIP is an expensive heat treatment to perform, which is becoming clearer due to the growth of the number of 3D printed implants. It is now not clear what other heat treatments are available, which give similar results to HIP or how effective the heat treatment should be in the first place. It could be possible that a less effective heat treatment still gives the desired results. Furthermore, a less effective heat treatment could be supported by design changes in order to achieve the desired mechanical properties.

Finally, it is important to understand the design requirements of a spinal cage. Currently, a spinal implant is universally designed to meet the requirements for a wide range of patients. This means that the spinal cage is designed for the worst case scenario, meaning that it is not perfectly suitable for many patients. Therefore it is important to think about patient specific designs which lead to more successful spinal fusion.

In the next chapter, a review of the literature is presented, aimed at understanding the production process and the design process of a spinal cage. The review of the production process has an extra focus on the heat treatment in order to understand the possibilities for alternative heat treatments and its relation to the mechanical properties and the design requirements. In Chapter 3 the problem statement and research questions are presented, along with the research objectives. Chapter 4 describes the methodology, which includes the design methods of optimising the original spinal cage design as acquired by Amber Implants; the experimental methods involving mechanical and fatigue testing; and the computational methods describing the simulations. Subsequently, Chapter 5 gives an overview of the acquired results and corresponding discussion. Finally, in Chapter 6 the conclusions of this thesis project are presented, along with further recommendations.

2

Background

In this chapter the relevant literature regarding the production and design process of a spinal cage is discussed. This is summarised in three main topics: the *requirements of a spinal cage*, which includes understanding how a spinal cage works and what the general (material) requirements are for a spinal cage; the *3D printing* process of a spinal cage and the difficulties involved; and finally the *post processing methods* with a big focus on heat treatments and a smaller focus on surface treatments.

2.1. Requirements of a spinal cage

Spinal cages must meet certain biological and mechanical requirements before being found safe to be used as implant. These include requirements for the material choice of the implant and the durability of the implant. Furthermore, successful spinal fusion requires the bone to grow into the implant in allo or auto grafts or in the porous structures. This process requires a certain surface quality in order to induce osseointegration. In this section a general overview of the different requirements of a spinal cage is given including a discussion of the relevant literature.

The material choice for a spinal cage depends on three important qualities the material should possess. One important quality for a suitable implant material is to be biocompatible and not toxic for the human body [62]. Secondly, the material should have the ability to support osseointegration, which is supported by a fully interconnected porous structure with a precise topological design. Finally, the implant material should have similar mechanical properties as that of bone [41][107]. Ideally, the spinal cage mimics the mechanical properties of the bone as closely as possible, especially regarding the Young's modulus.

2.1.1. Properties of a vertebra

A vertebra is made of bone, which is a natural composite made from organic components like type I collagen and inorganic crystalline minerals like hydroxyapatite. The structure is comparable to concrete used in buildings. The hydroxyapatite and the collagen in the bone are like what the steel rods and cement are in concrete, respectively. They provide a combination of strength and flexibility. Bone has different hierarchical levels and each of these levels will have different mechanical, biological and chemical functions. The levels of bone include macroscale, microscale, sub-microscale, nanoscale and sub-nanoscale. The macroscale level includes the shape of the bone, which can be divided in compact or cortical bone and trabecula bone. Compact bone is almost solid and the space that is available is filled with osteocytes, canliculi, blood vessels and erosion cavities. Trabecular bone consists of large

cavities. The porosity of bone can vary between 50% and 90% and the cavities are filled with bone marrow [106].

At the micro and nano scales type I collagen and the hydroxyapatite form the collagenfibril. The reinforced collagenfibril is a universal building block for compact and trabecular bone. Age, bone quality and the anatomical site can greatly affect the mechanical properties of bone. The strength of bone is just like the Young's modulus an anisotropic property. For example, compact bone is stronger in the longitudinal direction and trabecular bone is even more complex because apart from being an anisotropic material the mechanical properties also depend on the degree of porosity and the architectural arrangement of the individual trabeculae. Figure 2.1 gives an overview of a median section of a vertebra and the location of cortical and trabecular bone, showing the complex structure of bone.

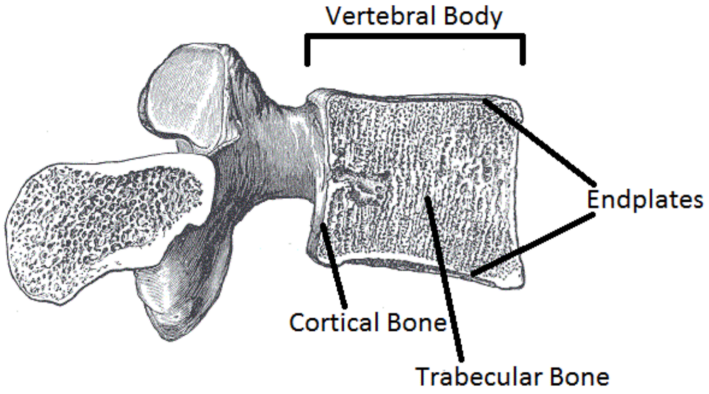

Figure 2.1: Median section of the vertebra showing the cortical bone and trabecular bone [40].

Furthermore, the mechanical properties of bone depend on the loading force and loading speed. The Young's modulus of bone is one of the most important properties in guiding artificial implant design. The Young's modulus of a vertebra is hard to determine due to its anisotropic nature. The measured Young's modulus of a vertebra depends on the applied load and loading speed. A wide range for the Young's modulus of a vertebra was found in the literature, with minimum and maximum values between between 10 and 1000 MPa [25][53]. as shown in Table 2.1.

Table 2.1: Overview of the different values for the Young's modulus of a vertebra as found by different studies. No. gives the number of experiments conducted.

Author and publication	**No.**	**Location**	**Young's modulus (MPa)**	**Standard deviation (MPa)**	**Minimum and Maximum (MPa)**
El Masri et al. [25]	22	T10-T12, L2	374	208	-
Nicholson et al. [80]	50	L1-L4	164.7	72.3	44.1 & 368.4
Cendre et al. [17]	32	L2	134	81	15 & 294
Chung et al. [22]	22	L3-L5	268	130	95 & 552
Banse et al. [8]	63	L1 and L4	352	145	-
Hou et al. [44]	28	T12	316	222	78 & 975
Gong et al. [38]	6	L4	259	121	-

It is clear that due to the anisotropic properties of bone, it is very difficult to produce an implant that will match the mechanical properties of bone. However, trying to match the mechanical properties as closely as possible is important for effective load transfer and alleviating the stress shielding effect [41][106]. Mechanical tests are a great way to get to know the different properties of bone, but when someone needs an implant it is also important to estimate the mechanical properties of that specific patients vertebrae. Since it is not possible to do these mechanical tests on patients, other methods have to be used. Bone mass is directly dependent on the size and the density of mineralised tissue contained within its periosteal envelope. Areal bone mineral density (aBMD), which is the amount of hydroxyapatite in grams per cm^2, can be measured by quantitative computer tomography (QCT) or dual energy X-ray absorptiometry (SXA and DXA). This can be used to estimate the mechanical properties of the bone, because BMD is directly proportional to the resistance of the skeleton to mechanical stress [108].

2.1.2. Material selection

The most commonly used material for spinal implants is Ti6Al4V. This material can be used in additive manufacturing, which gives it a big advantage over alternative materials, since creating complex shapes and porous structures is very expensive or impossible with conventional machining methods. Additive manufacturing allows a broad range of design possibilities at reasonable costs. Ti6Al4V is an α-β titanium alloy which has a high strength to weight ratio. It is biocompatible and is corrosion resistant. Apart from a wide range of biomedical applications it is also commonly used in the aerospace industry where a high strength to weight ratio and excellent corrosion resistance are necessary [39]. By using different combinations and methods of post processing it is possible create a wide range of mechanical properties for this material in order to get closer to the mechanical properties of a vertebra.

Looking at the first requirement of biocompatibility, Ti6Al4V has shown to be biocompatible because it has a low electrical conductivity, which contributes to electrochemical oxidation of titanium. This leads to the formation of a thin passive oxide layer [89], which in turn results in great corrosion resistance. A higher resistance to corrosion is favourable for biocompatibility, because of the stable and an inert oxide layer.

Some titanium, vanadium and aluminium can be released from the implant, which can have an effect on the body. Vanadium may cause sterile abscess and aluminium may cause scar tissue [106]. High concentrations of titanium can induce the release of osteolytic cytokines, which are usually involved in implant loosening [51]. Other elements can be used to produce a biocompatible titanium alloy, such as tantalum, niobium, zirconium and molybdenum. However, aluminium and vanadium are α and β phase stabilisers, respectively, and they will influence the mechanical properties of the material during heat treatment [106]. One study has shown that the concentration of titanium, aluminium and vanadium in the body will all reach a plateau after 8 years and do not show big signs of toxicity [110].

Finally, good osseointegration is necessary in order for spinal fusion to be able to occur. Studies have demonstrated that on nanophase materials (like Ti6Al4V) an increased activity of osteoblasts (bone forming cells) is observed compared to conventional alloys, polymers and ceramics [107]. Nanophase material are materials that have grain sizes less than 100 nm [107].

Looking at the Young's modulus of Ti6Al4V as shown in Table 2.2, it is much higher, about a factor 1000 higher, than that of a vertebra. In order to avoid stress shielding at the bone-implant interface the apparent Young's modulus of the implant has to be modified [41]. An

Table 2.2: Material properties of different solid materials [57][77][83].

	Young's modulus	3D pintable	Elongation at break	Yield strength	Biocompatibility	Chemical stability	Osseoinductivity
Ti6Al4V ELI (grade 23)	113.8 GPa	Yes	15%	790 MPa	Yes	Good	Good
Titanium	116 GPa	Yes	54%	120 MPa	Yes	Good	Good
Tantalum	186 GPa	Yes	30%	170 MPa	Yes	Good	Good
Magnesium	45 GPa	Yes	3 - 15%	90 - 105 MPa	Yes	Low	Coating required
Iron	200 GPa	Yes	1 - 15%	50 MPa	Yes**	Low	Good
Nitinol	38 GPa	Yes	15%*	814 MPa	Yes	Good	Good
CRF-PEEK	18 GPa	Yes	1 - 2%	120 MPa	Yes	Good	Coating required
PEEK	3.5 GPa	Yes	30%	80 MPa	Yes	Good	Coating required

* 8% max strain recovery
** More cytotoxic than Ti6Al4V

effective method to achieve this is by introducing porosity in the material [106].

Other alternative materials for implants, such as titanium, tantalum, magnesium, iron. nitinol, CRF-PEEK and PEEK are also shown in Table 2.2. These materials have their own advantages and disadvantages. However, due to the superior properties of Ti6Al4V and its already abundant use in different implants, this alloy is chosen for this thesis as the most suitable material for a PLIF spinal implant.

As mentioned before, additive manufacturing is the preferred method of producing the spinal implant. However, in order to produce an implant, not any type of Ti6Al4V powder is suitable. During 3D printing of a medical implant, a Ti6Al4V powder is used that is produced by gas atomisation or rotating electrodes. This powder is called an ELI powder, which means *extra low interstitials* with regards to the interstitial impurities, such as oxygen, carbon, hydrogen and nitrogen. Due to the low amount of oxygen, nitrogen and hydrogen, the amount of corrosion during 3D printing is reduced. Contamination due to oxygen, nitrogen and hydrogen in the environment during 3D printing will reduce the ductility of the material and reduce fatigue life. Titanium and its alloys have a high affinity to these contaminants and an increased temperature will fuel the reaction between these contaminants and titanium. The contamination will act as α stabiliser and during deformation will pin the dislocations, increasing the Young's modulus of the material [66]. However, one downside of the ELI powder is the high costs. This powder costs usually more than $400 per kg, while conventional Ti powders used for additive manufacturing, cost around $30 per kg [119].

2.1.3. Osseoinductivity

When an implant is placed in the body the first thing that occurs is the absorption of water molecules, proteins and lipids onto the surface of the implant from the blood. The specific concentration of the absorbed substance depends on the surface properties of the implant.

Many different proteins in the blood will interact with the implant, which can cause cell attachment and growth or an inflammatory response. Eventually, blood platelets attach to the implant releasing their inner content, which promote the formation of fibrin clots, which function as mesh-work to fill the voids and allow cell migration towards the implant. The strength of the attachment between these fibrin clots and the implant will depend on the surface properties of the implant. It is suggested that an increased surface roughness will increase the strength of the connection [65].

The first cells which arrive at the implant are neutrophils and macrophages, which will clean the wound, after which the mesenchymal stem cells (MSCs) arrive. MSCs are able to travel through the dense fibrin clots to the surface of the implant and are able to differentiate into osteoblasts, chondrocytes and fibroblasts, depending on what is needed at that specific location. The stem cells will mainly form bone tissue near the implant and some soft tissue at the interface between the implant and the bone. The osteoblasts formed will either proliferate for a few cycles or start making a non collagenous assortment of proteins which will initiate mineralisation called a cement line. This cement line will support the recruitment and maturation of the osteoblasts.

The next step for successful osseointegration is the bone remodelling phase, where osteoclasts resorb newly formed bone to remove cracks and prepare the surface for new bone formation. These osteoclasts will dissolve the calcium phosphate crystals, but will not produce collagenase which is required to break down collagen. This will leave micro and nano scale structures created by the remaining collagen giving the bone a high degree of complexity. This complex structure is the signal osteoblasts require, when they are looking for a new surface for bone formation. By mimicking these macro and nano scale structures on the surface, the formation of bone on the surface of the implant will improve. When the surface of the implant does not have these surface qualities a layer of fibrous tissue between the implant and the bone can be formed which will prevent good osseointegration and a good outcome of the procedure [33].

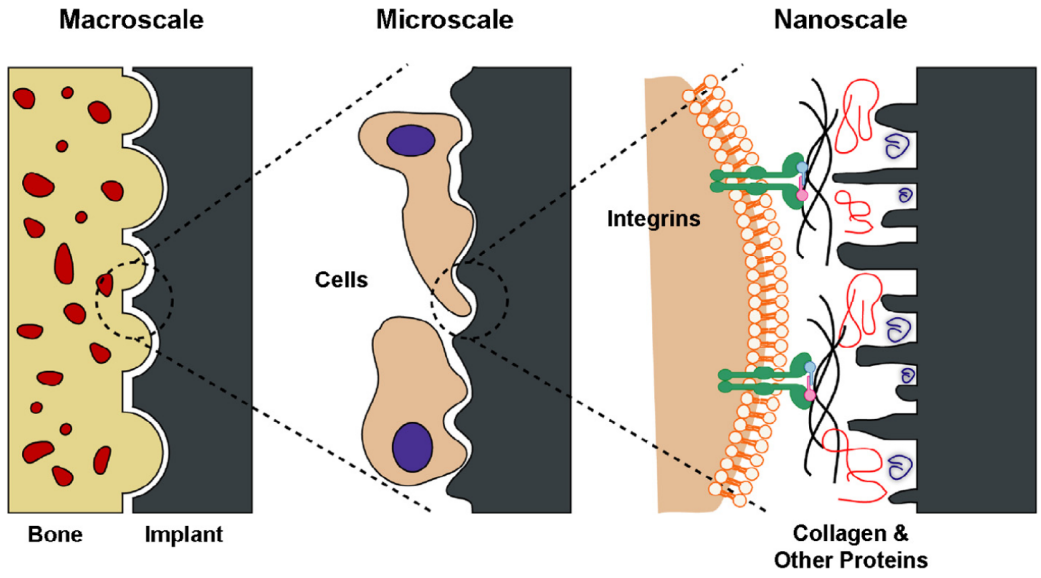

Figure 2.2: At the macroscale, the implant should provide a good mechanical fixation with bone. At the microscale the implant can directly interact with osteoblasts and mesenchymal stem cells. At the nanoscale, cell membranereceptors, such as integrins, can recognise proteins adsorbed on the surface [33].

A previous study has shown that on a nanoscale material increased function of osteoblasts was observed [107], which is explained by the increased osteoblast adhesion observed at grain boundaries [107]. The bone implant interface is shown in Figure 2.2 from macro to nano scale. Depending on the microstructure of Ti6AL4V may not have a nano scale structure. However, only the surface of the implant has to be nano scale for improved functionality of osteablasts, which can be achieved with surface post processing methods, such as etching or the application of a coating, as described in Section 2.3.2.

2.1.4. Durability of the implant

The durability of the implant is important to consider. It takes about 3 to 6 months for bone ingrowth to occur and the completion of the fusion of two vertebrae [100]. Taking some margin, this means a spinal cage should not fail for at least about a year in the operation conditions in the body. Failure can occur when a large load is applied, breaking the implant at its weakest point or by a lower cyclic load. This does not lead to instant failure, but each loading cycle incrementally damages the implant. The durability of the implant therefore depends on the strength of the implant, and the fatigue life of the implant.

Strength

For the strength of an implant the column load on the spinal cage is important to consider. Different researchers have investigated column load in different conditions. Wilke et al. [109] investigated the interdiscal pressure in the L4-L5 disc while an average person was holding a 20 kg object 600 mm away from the chest. They found an interdiscal pressure of 1.8 MPa, which is equivalent to a force of 3240 N in a disc area of 1800 mm^2. Iyer et al. [47] found a mean lumbar compressive force of 1693 N for an average person with a 10 kg load in the hands with the elbows bent to 90°. Finally, Schultz et al. [87] investigated the column load for different body positions and activities. He found values ranging from 0.27 MPa (486 N of load over 1800 mm^2) in a relaxed standing position to 1.62 MPa (2916 N of load over 1800 mm^2) in the most strenuous task examined.

For the purpose of this project and taking into account some safety margin, the spinal cage should be able to hold a compressive load of at least 4000 N, as was also used by Figueroa-Cavazos et al. [28] as the column load for their finite element analysis of compression testing of a spinal implant.

Fatigue resistance

When a material is subjected to a cyclic load fatigue failure can occur. Fatigue failure is one of the most common failure modes. Spinal implants are subjected to cyclic loads, which make them susceptible for fatigue failure. Fatigue resistance of the implant is therefore an important factor to consider. To estimate the fatigue life of a certain material a stress-life (S-N) or a strain-life (ϵ-N) graph can be made, where N is the number of cycles until failure. These graphs give an idea of the fatigue life on a macro level, but can also be used to estimate the fatigue life on a microscopic level. The fatigue life on a microscopic level can be found by determining the crack propagation threshold (ΔK_{th}), which is the intensity factor before the crack propagates, or by determining the stress threshold ($\Delta \sigma_w$), which is the fatigue limit before the crack propagates. For determining the fatigue life it is also important to know the stress ratio (R-ratio), which is the ratio between the minimum and maximum stress in one cycle, because this greatly affects the fatigue life. For a fatigue life of 5,000,000 cycles, a cyclic load of 600 N is advised along a R-ratio of 0.1 for testing on one spinal cage [28][47].

Four major factors that affect the fatigue life found in literature are surface quality, residual stress, microstructure and internal defects [66]. When using additive manufacturing the

material will be plagued by surface roughness and internal porosity. These internal pores and rough surface are both crack initiations sites. The quality of the surface is far more important compared to the internal defects. An untreated surface will act as multiple stress concentrators and will behave like short cracks. The fatigue life of a product without surface treatment can be about 40-50% compared to a product with surface treatment. Also noteworthy is that a crack will form not at the highest tensile stress, but at the highest shear stress nearby [81].

In addition to the stress acting on the internal pores, the size and shape play an important role. If all the internal pores would have the same shape fatigue failure will occur at the largest defect, but the cross sectional area of an internal pore normal to the applied stress is far more important than the volume. The aspect ratio is the ratio of the longer side with respect to the shorter side. Defects with a similar volume but a higher aspect ratio have a larger probability for crack initiation. This can be seen if you compare gas pores and lack-of-fusion pores. Gas pores will have a round shape and an aspect ratio close to 1 while lack-of-fusion pores have an aspect ratio larger than 1 due to its sharp tips. These sharp tips induce concentrated stresses on the material which will initiate cracks more easily [81].

Apart from surface roughness and internal porosity, additive manufacturing has an influence on the residual stress of the implant. During 3D printing of Ti6Al4V using, for example, selective laser melting (SLM), layers of ELI powder are melted on top of each other using a laser. The laser will increase the temperature of the Ti6Al4V and attaches a melted layer on top of the previous layer. However, when the temperature drops again, this will create a residual stress in the material. This residual stress in the material will increase with each layer that is added. High values of residual stress will occur near the free surface of the product and peak values are found at the final deposition layer [24]. When a new layer is formed on the previously deposited layer the tensile stress in the previous layer will convert to compressive stress due to subsequent thermal cycling. The amount of residual stress in the material can be changed by changing deposition strategy and track length. The residual stresses are higher in the scan direction due to a larger thermal gradient and also an increase in residual stress is observed with a longer track length. The residual stress in the material will reduce the fatigue life of the material, because it can cause crack initiation in the material. It is important to note that the residual stress in the material will consist of tensile and compressive stresses. The compressive stress is actually beneficial to the fatigue properties of the material, while tensile stresses add an additional driving force for crack initiation and propagation [104].

Finally, the microstructure is affected by additive manufacturing and could affect the fatigue life and other mechanical properties of the implant. This will be further discussed in Section 2.3.1.

Mechanical properties of porous structures

Due to the design freedom of additive manufacturing many different porous structures and sizes can be achieved. In Figure 2.3 multiple structures are shown, which are mechanically tested by Ahmadi et al. [2]. From these tests it became clear that the mechanical properties and failure mechanisms highly depend on the type and dimensions of the unit cell. The unit cells can be divided into low and high Young's modulus groups. The high Young's modulus group includes truncated cube, truncated cuboctahedon, rhombicuboctahedron and cube. The low Young's modulus group includes diamond and rhombic dodecahedron. Since the mechanical properties of the low Young's modulus group more closely resemble that of bone, this group is considered. Furthermore, since the diamond structure also has the lowest compressive strength, which resembles the bone more, the diamond structure is chosen as an ideal structure for spinal cages [2].

The second step is finding the ideal size of the pores that are created by the porous struc-

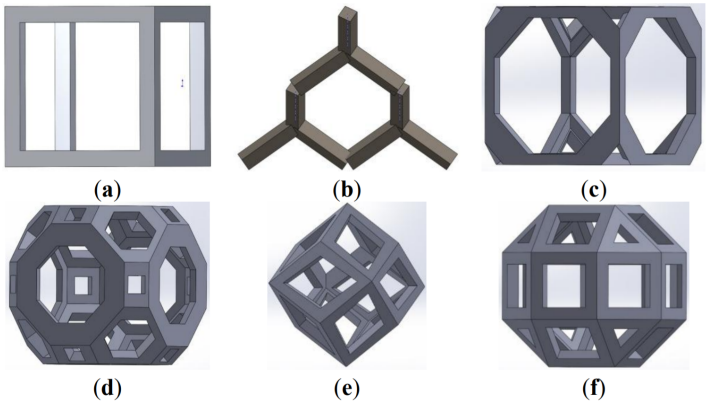

Figure 2.3: Schematic drawings of the unit cells used in the porous structure: (a) Cubic; (b) Diamond; (c) Truncated cube; (d) Truncated cuboctahedron; (e) Rhombic dodecahedron; and (f) Rhombicuboctahedron [2].

ture. Bone can already be formed at micropores with a size less than 10 µm, but a larger pore size will improve the vascularisation. A study shows that the upper limit for improving the vascularisation is at 400 µm [13], but another study show this can be as high as 700 µm [61]. Implants with a smaller pore size have a larger surface area for bone to grow into, but the permeability is higher at a bigger pore size. The permeability of the implant is important, because the transportation of cells, nutrients and growth factors require the blood to flow through the implant. Permeability is characterised by the gradient pressure it takes for the blood to flow through the implant [106]. The pores in the material are interconnected, which benefit the body fluid circulation, nutrient transport, vascularisation and bone ingrowth. The enhanced bone penetration facilitates a bigger tissue-material interaction, which enhances the load transfer along the interface to the surrounding tissue [84]. Current studies even suggest that spinal cages with a high titanium porosity can achieve solid interbody fusion without using bone grafts [118].

2.1.5. Regulations and standards

As discussed above the material requirements and durability requirements are important factors to consider. Fortunately, there are regulations and standards involved before a medical implant is approved for use in order to ensure that only safe implants will be used in surgery. Requirements can involve things like mechanical properties, biocompatability, microstructure and testing methods. The requirement for the microstructure of Ti6Al4V is an equilibrium α and β phase structure (ASTM F136, ASTM F620, ASTM F1108). To meet this requirement, often some sort of post fabrication heat treatment is necessary [114]. Most of the requirements involving test methods are described in ASTM F 2077-18, ASTM F 2193-02, ASTM F 1717-96, ASTM F 2077-01 and ASTM F 2267-04.

Fatigue testing of intervertebral body fusion devices should be carried out between two polyacetal test blocks to eliminate the effects of the variability of bone properties and morphology on the fatigue tests. The ultimate tensile strength (UTS) of the polyacetal blocks should not be less than 61 MPa. The static testing of an inter-vertebral body fusion device should be carried out between two stainless steel blocks with a UTS of at least 1310 MPa. The intradiscal height should be determined from the data of the intended level of application. The suggested height for the lumbar spine is 10 mm. The intradiscal height should not reach zero before failure. All the test samples should be unused parts only. Each pair of polyacetal blocks should be used for one test only. The metal blocks can be reused if not damaged. All static

tests should have at least five samples. For the static tests the metal blocks should have the appropriate matching geometry of the intervertebral body fusion device. The intradiscal height shall be constant for all test. The deformation rate should not exceed 25 mm/min until functional or mechanical failure of the intervertebral body fusion device.

For the dynamic tests the polyacetal blocks should have a matching geometry with the intervertebral body fusion device and the intradiscal height should be constant for all tests. Select necessary forces to develop a well defined force-cycle to failure trend comprised of a minimum of six data points. Suggested maximum forces are 25, 50, 75% of the yield stress of the intervertebral body fusion device, which should be obtained by performing compression tests. This data should be used to plot a graph of applied force versus the number of cycles. The end of test requirement is functional failure or 5,000,000 cycles without functional failure. Note that any not functional failure at the 5,000,000 cycle point (like crack initiation and propagation) should be noted. The maximum run-out force is to be determined. It is recommended that implants shall be examined for mechanical failure at intervals throughout the dynamic tests, however, it is also recommended that the implant should not be removed from the test. The frequency of the dynamic test should be determined and recorded. Frequencies above 10 Hz may result in heating of the polyacetal blocks and the user of this test method is left to find an appropriate cyclic frequency [34].

2.1.6. Conclusions regarding the requirements of spinal implants

From this section regarding the requirements of a spinal implant, it can be concluded that 3D printed Ti6Al4V is a suitable material for a spinal implant. Ti6Al4V is biocompatible and with a fully α + β structure it is in compliance with the regulations and standards regarding spinal implants. It was found that a diamond lattice structure for the porous part of the implant is most favourable because of the lower resulting apparent Young's modulus. Moreover, from literature a poresize between 10 and 700 microns was found to be optimal for osseointegration and therefore the chance of successful spinal fusion.

Regarding the durability of spinal cage a minimum fatigue life of 5,000,000 cycles at 1200 N is required, as well as no yielding at a minimum load of 4000 N. These results are all summarised in Table 2.3.

Table 2.3: Overview of the requirements of a spinal implant, regarding the material choice, the porous structure and the durability of the implant.

Requirement/advise	Value	Source
Biocompatible	Yes	[89]
Microstructure	fully α + β structure	ASTM F136, ASTM F620, ASTM F1108
Lattice structure	Diamond	[2]
Pore size	10 - 700 microns	[13][61]
Fatigue life	5,000,000 cycles at 1200 N	ASTM F2077
Strength	No yielding at 4000 N	[28][47]

2.2. 3D Printing

There are several ways to produce an open-cell porous metal structure. This includes liquid state processing (such as spray foaming), solid state processing (such as sintering), electro depositioning and vapour depositioning. The shape and size of the pores in this material can be adjusted by altering the parameters of the process, but only a randomly organised structure can be achieved with these methods. However, using additive manufacturing (AM) it is possible produce an open-cell porous metal structure with a predefined internal architecture [106].

AM processes are affected by a large group of process parameters, such as power, scan speed, scan strategy, hatch spacing, layer thickness and many more. There is also a large difference in energy input and thermal behaviour when choosing between powder bed and blown powders. The choice in powder is important, because the absorptivity, physical properties, particle size and particle shape determine the interactions between the laser/electron beam and the powder. The heat dissipation during the printing process will have an effect on the properties of the finished product.

2.2.1. Powder Bed Fusion

Powder Bed Fusion is a commonly used 3D printing method, which is suitable for printing complex porous structures for medical implants. During powder bed fusion (PBF) focused energy, using either an electron beam or a laser beam, is used to selectively melt or sinter a layer of a powder bed. Melting is more commonly used for metals, therefore selective laser melting (SLM) and electron beam melting (EBM) will be discussed in this section.

Selective laser melting (SLM) is the most widely used method in the AM industry [42]. SLM normally consists of a system of lenses and a scanning mirror or galvanometer to move the position of the laser beam. A schematic overview of an SLM process is shown in Figure 2.4. The entire process takes place inside a closed chamber, which is usually filled with an inert gas, such as N_2 or Ar, in order to minimise oxygen contamination during the printing process.

Electron beam melting (EBM) is very similar to SLM, but uses an electron beam for the melting and fusion of the powder particles. The set-up is comparable to a giant scanning electron microscope, which requires a filament and magnetic coils to collimate and deflect the position of the electron beam [35]. EBM occurs in a vacuum atmosphere, which also averts oxidation of the parts. A schematic overview of an EBM process is shown in Figure 2.5.

When comparing SLM and EBM, there are some important differences. The powder distribution is different between EBM and SLM. SLM systems use a dispersing piston and roller, while EBM systems use powder hoppers and a rake. When starting the PBF process a build substrate must be positioned. A build substrate or a start plate is used to give mechanical and thermal support to the build material. For fixation the SLM process mostly clamps down the substrate and the EBM process sinters the powder surrounding the plate to provide stability.

During the build when new layers are applied the existing layers should not move. The thermal properties of the substrate are important, because the building is prone to swelling and other process defects. The powder containers must be filled and the sensors checked. The operation is guided by a scan strategy and process parameters. After the build the excess powder can be recovered from the build chamber. For EBM the powder is put through a powder recovery system to recover sintered powder around the parts. For SLM sintering around the parts is less pronounced, so the powder can be sifted directly for re-use [86].

Looking at the cost and speed, SLM out performs EBM. The EBM process takes more time to process each layer compared to SLM, because the electron beam may be used mul-

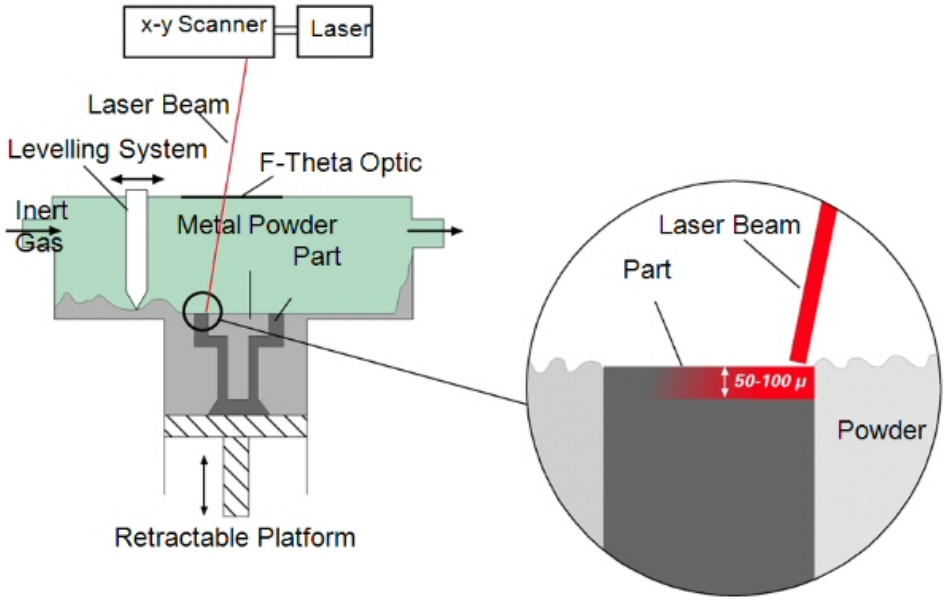

Figure 2.4: Schematic overview of the SLM process [119].

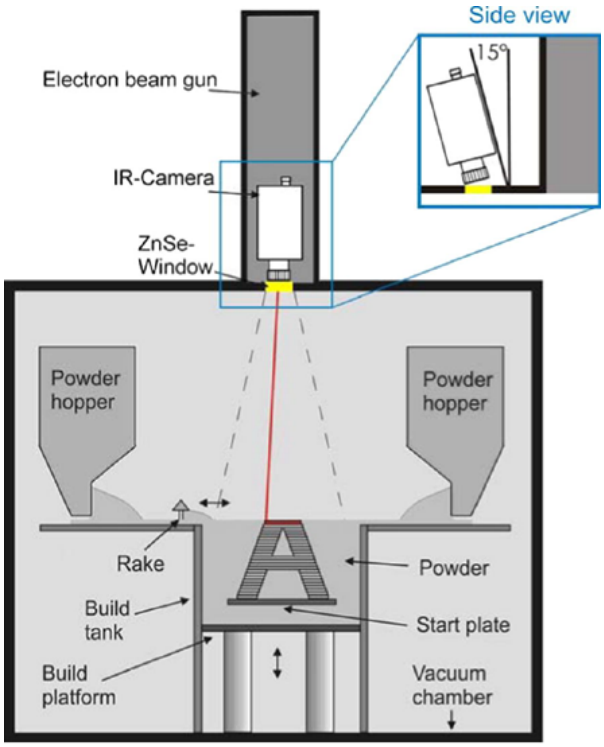

Note: Inset is showing a side view of the IR-camera setup mounted with a 15° angle relative to the beam column

Figure 2.5: Schematic overview of the EBM process [88].

tiple times to heat the powder bed and then to melt the parts selectively and is therefore used multiple times each layer [35]. Furthermore, the entire chamber becomes very hot in the process, meaning overnight cooling is necessary before the powder bed reaches room temperature and the parts can be removed from the chamber and substrate plate [35]. This makes parts produced by EBM much more expensive than SLM. Therefore, for the purpose of the experimental part of the thesis, the cheaper SLM printed samples will be used. In the next subsections the effect of the SLM process on the material properties of a produced Ti6Al4V part will be discussed.

The major sources of 3D printing defects are unmelted or partially melted powder; gas entrapment; lack of fusion; and delamination between adjacent passes or previously deposited layers [39]. This leads to two main types of printing defects, which are the presence of internal pores and the presence of surface defects. As described in Section 2.1.4 both the surface roughness and internal pores have an effect on the fatigue life of the part, because they act as stress concentrations.

Defects in 3D printed samples can be detected using micro-CT. Defects will show dissimilar size characteristics for different printing processes and printing parameters. The CT detectability plays a critical role in the defect visualisation. When the defects are small it is hard to visualise the contour of the defect. For example, when using an ACTIS 200/225 Ffi-HR CT/DR system, defects smaller than 21 µm are hard to visualise [37]. When the defects are bigger it is possible to visualise the defects better to determine the aspect ratio of the defect and visualise sharp edges as shown in Figure 2.6. Samples usually show a homogeneous grey scale in CT scans, but defects will cause variations of brightness in localised areas of single slices. Using image processing the porosity of the material can be estimated [37].

From the images it is also possible to determine the shape and size of the pores. Pores with a higher aspect ratio but similar volume will more likely lead to crack initiation.

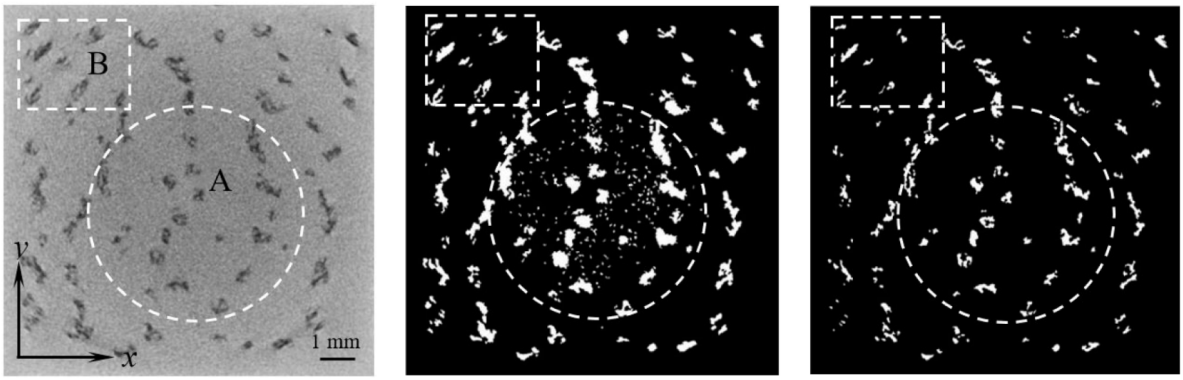

(**a**) Original slice (**b**) Binary image 1 (**c**) Binary image 2

Figure 2.6: Image processing of a single slice of CT scanned EBM specimen [37].

For a 3D printed product made from Ti6Al4V post surface treatment is necessary, because the surface defects will deteriorate the fatigue performance. SLM samples have a relatively high stress threshold ($\Delta\sigma_w$) and a lower propagation threshold (ΔK_{th}) compared to EBM. A higher $\Delta\sigma_w$ indicates a higher fatigue strength and a higher ΔK_{th} indicates a higher fatigue toughness. In order to improve the fatigue toughness a heat treatment can be used, which removes the residual stress from the sample caused by the printing process. This increases the materials crack propagation threshold [66].

Hot isostatic pressing (HIP) is a post processing method which will improve both the fatigue

strength and the fatigue toughness. It can effectively reduce the pore size in the material, which are undesired crack initiation points in the material. After conducting fatigue tests on 3D printed Ti6Al4V in horizontal and vertical directions, a difference was found in the $\Delta\sigma_w$ and ΔK_{th} values [66]. This difference shows that the material has an anisotropic structure which also affects the fatigue properties.

Printing direction and angle

An AM build part from Ti6Al4V shows significant anisotropy in mechanical properties in different orientations. In the longitudinal direction samples generally have a lower UTS and yield strength compared to horizontal samples, but the elongation until failure increases. These macro mechanical properties in different directions are associated with an anisotropic microstructure. This microstructure will consist of columnar β grains and α grains at the boundaries. The β grains will grow in the longitudinal direction along the deposition direction. During 3D printing of Ti6Al4V the size of β grains varies from 1 to 20 mm in length and a few hundred microns in width [105][113]. This can be seen in Figure 2.7.

Along the β grains a thin layer of α will be formed, delineating the β grains. This α phase along the β grains acts as a weak band connector and reduces the integrity of the microstructure. The α phase serves as a path along which defects accumulate. When Ti6Al4V samples are subjected to tensile loads in the horizontal direction, *i.e.* subjected on the short axis of the β grains, the α phase acts to separate adjacent β grains. When these samples are subjected to tensile loads in the vertical direction, *i.e.* subjected on the long axis of the β grains, the samples are less likely to fail. However, if due to lack of fusion pores prevail between the layers, the situation will be the opposite [66].

By re-positioning the sample it is possible to achieve increased or decreased mechanical properties in the direction where it is most needed. Furthermore, the printing angle has an effect on the surface roughness, which affects the biocompatibility. By increasing the printing angle with respect to the surface, more unmelted metallic particles will remain on the surface, which will create a higher surface roughness, but also sharp contact angles. Adhesion and proliferation of bone forming cells were found similar on the surface of various angles, although improved cell spreading was observed at higher additive angels because the cells were initially less adhered [19].

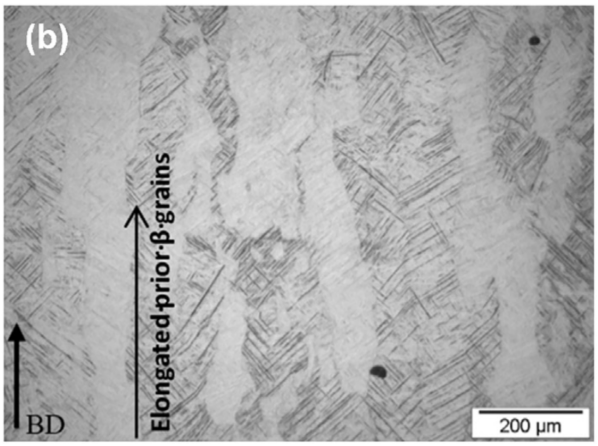

Figure 2.7: The morphology of prior β grains formed in selective laser melted Ti6Al4V [66]. BD represents the deposition direction.

Printing temperature

Ti6Al4V will be completely liquid at 1650 °C and it will be completely solid again at 1605 °C [83]. The temperature of the melt pool will depend on the laser power and process conditions. For example, for SLM with a laser power of 350 W, a deposition rate of 0.13 g/s and a layer thickness of 508 µm, the temperature of the meltpool will be between 2000 °C and 2500 °C [70]. During cooling the material solidifies again and the cooling rate will have a large influence on the microstructure of the material. The cooling rate during 3D printing will be between 12,000 °C/s and 40,000 °C/s [70].

As discussed earlier columnar β grains will form in Ti6Al4V, but when the cooling rate exceeds 410 °C/s this β phase will transform in α'- martensite. The orientation relationship between α'- martensite and β will determine the growth orientation of the martensitic needles. Martensitic needles will generally form about 40° inclined with respect to the building direction [39]. More research is needed about the local melt pool physics and the liquid-solid interface. This will lead to new strategies for improving the build on a macro and micro level. Moreover, the influence of powder characteristics remains not sufficiently explored [106].

It is already possible to produce an α + β dual phase Ti6Al4V without any α'-martensite using a low laser power and low scan speed. This method enables a long interaction between the laser and the material and a high energy input over a larger volume of material, resulting in slower heat diffusion and therefore a reduced cooling rate. As a result, an α + β dual phase is obtained [66].

Because of the high thermal gradients used the SLM process, a large amount of residual stress is observed The residual stress in the material can be lowered by stress relieving the material at an elevated temperature [66]. Ideally the residual stresses from the 3D printing process are removed which will be discussed in the next section.

2.3. Post processing

After 3D printing the spinal cage will not have the desired mechanical properties yet. Several steps of post processing can be used to change this. Heat treatment can be used to remove residual stress and to change the microstructure. Surface post processing, including sand-blasting, etching and coatings, can be used to modify the surface.

2.3.1. Heat treatment

During heat treatment the microstructure of the material changes. How the microstructure changes depends on the heating time, temperature and cooling rate. To get a uniform α + β microstructure a lot of knowledge is needed about how these variables will influence the material.

Microstructure

After 3D printing Ti6Al4V will often have an α'-martensite microstructure. According to Wang et al. [106] using XRD measurements no indication of the presence of a β phase is found. To change the microstructure a post heat treatment can be applied. Temperature, time and cooling rate will all have a significant effect on the creation of a certain microstructure. When heating the material an α phase will precipitate at the α'-martensite boundaries, where the α phase is present in fine needles. A β phase will form at the grain boundary of the α grains and the material will transform to an α + β mixture, but the α'-martensite grain size will prevent unlimited grain growth.

During 3D printing a melt pool is created and on solidification of this melt pool the material is

transformed to a β phase and prior β grains are formed. When the material temperature drops below the β transus temperature (995 °C) α'-martensite phases are formed within the prior β phase [106], as shown in Figure 2.8b. The β transus temperature is where the materials stable phase will change from a BCC β phase (above) to a HCP α phase (below) [103]. The effect of a HIP heat treatment at different temperatures (below and above the β transus temperature at 800 and 1050 °C, respectively) on the microstructure of a 3D printed Ti6Al4V alloy can be seen in Figure 2.8.

When post heat treatment is applied, these prior β grains are clearly visible due to the α phase formation at the grain boundaries. The eventual width of the α grains mainly depend on the maximum temperature for sub β transus heat treatments and on the cooling rate applied in super β transus heat treatments. The closer the temperature to the β transus temperature, the more the cooling rate and residence time will influence the result. When treated above the β transus temperature, prior β grains will form and grow extensively and the residence time will determine the final dimensions and the β grains will no longer be long columnar grains, as shown in Figures 2.8c. Eventually a 100% β phase microstructure will form. During cooling, a lamellar α + β mixture will be formed.

When the maximum temperature of the heat treatment rises, the yield strength and the UTS will decline, while the fracture strain rises because of the transformation of the fine α'-martensite needles to a coarser α + β mixture. Overall the best results are achieved when heat treated at 850°C for 2 hours according to Vrancken et al. [103]. Also heat treatment above the β transus temperature is interesting to look at, because the grain growth is not limited by the α'-martensite boundaries formed during 3D printing [106].

As discussed earlier the fatigue properties of 3D printed Ti6Al4V can be expressed in fatigue strength and fatigue toughness. As-built samples will usually have a higher fatigue strength, but a lower fatigue toughness. This high fatigue strength of as-built parts is due to the presence of α'-martensite, which contains a high concentration of dislocations. α'-Martensite has a very fine structure which impedes the motion of dislocations, increasing the fatigue strength even more. This increase of fatigue strength will come at the cost of the plastic strain of the material.

After heat treatment an increase in the fatigue toughness is observed due to the decomposition of the fine α'-martensite phase and the removal of any residual stress in the material. After sufficient post heat treatment a uniform α + β mixture will arise. With a decreasing amount of α phase in the material the fatigue strength increases. A study revealed that when the thickness of the α-laths decreased from 10 to 1 µm the fatigue strength increases by 20% [69]. Moreover, as discussed earlier defects act as crack initiation points, but when the material is defect free the plastic slip localisation will become the main source for crack initiation. A finer microstructure will have a higher fatigue strength because a greater amount of grain

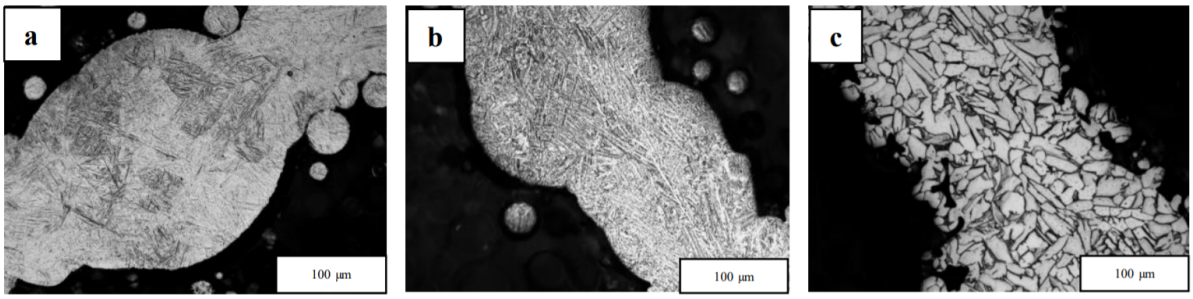

Figure 2.8: Microstructure of 3D printed Ti6Al4V using SLM a) as-processed, and HIP heat treated at b) 800 °C (below the β transus temperature) and c) 1050 °C (above the β transus temperature) [4].

boundary will impede the localisation of plastic slip. In Ti6Al4V plastic slip will occur at the HCP α phase and cause crack initiation. When the crack driving force increases the crack will propagate and starts to interact with the β grains. When the thickness of the α phase reduces, long plastic slip bands are not able to form, resulting in a bigger resistance to fatigue crack initiation [9] [66].

Heating time

Larger grains are created at high temperatures with a longer residence time. The microstructure created during heating will depend on the temperature, residence time and heating rate. For heat treatments below the β transus temperature the residence time and heating rate are of minor importance. The influence of residence time will increase for higher temperatures in the α + β range. In Figure 2.9 the microstructure of Ti6Al4V is compared after heat treatments of 2 hours and 20 hours. The α phase started to globularize, which is indicated by the arrows. The majority of the structure remains similar to that after 2 hours. The α grain thickness in Figure 2.9 have coarsened slightly to a bigger width from 2.23 $\pm$ 0.12 µm to 2.80 $\pm$ 0.16 µm.

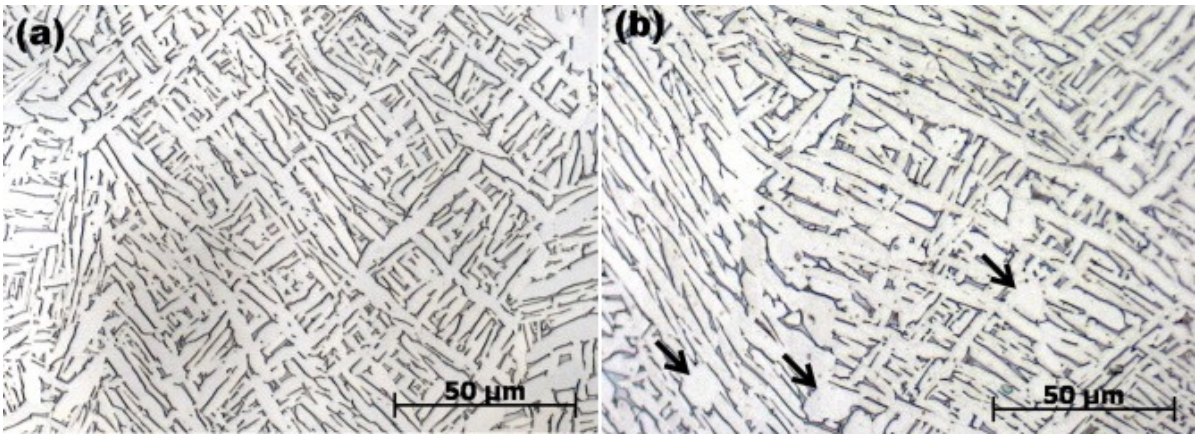

Figure 2.9: Comparison of the similarity in α grain thickness after (a) 2 h at 940 °C and (b) 20 h at 940 °C, followed by furnace cooling. The α phase is light, β is dark. The arrows in (b) indicate globularized α grains [103].

Vrancken et al. [103] found that a 50% globularization is found when heat treated at 995 °C for approximately 8 hours.

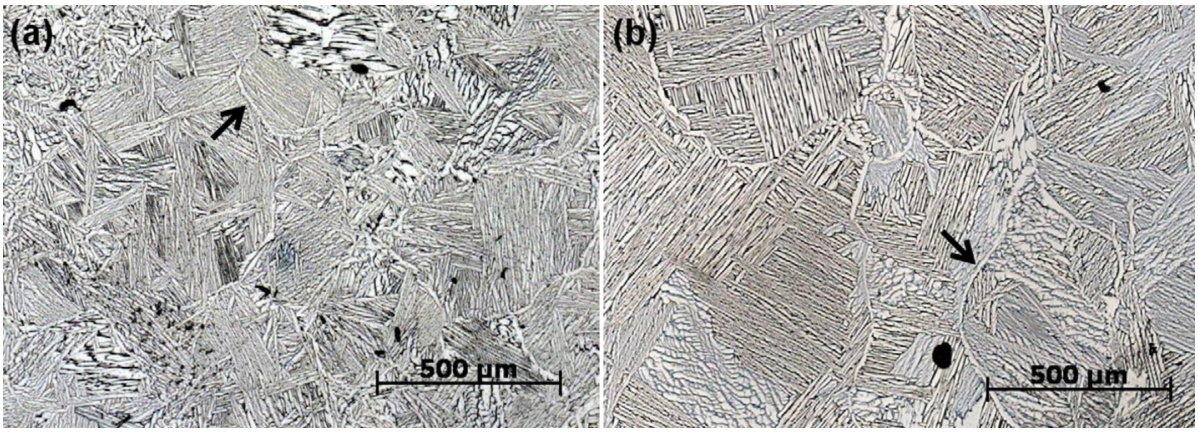

Figure 2.10: Illustration of the smaller α colony size after (a) 2 h at 1020°C compared to after (b) 20 h at 1040°C, followed by furnace cooling. The α phase is light, β is dark. The arrows indicate grain boundaries [103].

The samples used for this research have a microstructure which resemble elongated grains rather than a lamellar structure. For a lamellar structure the time for globularization is expected to increase significantly. When heating the material above the β transus temperature, the residence time becomes a lot more important. The material consists of a single phase and grain growth can occur fast and unhindered, because of the high temperatures. The final size of the α colonies is limited to the the prior β grain size. Larger sizes are possible for longer residence times. Looking at Figure 2.10 it is clear that the colonies become larger for longer residence times. The size of these colonies is a determining factor for the mechanical properties of the material. This means that the residence time during β annealing is an important parameter to consider [103].

Cooling rate

When a material is cooled at a rate faster than 5 °C/s it is called quenching. Cooling rates above 410 °C/s will result in a fully martensitic structure for Ti6Al4V. The cooling rate when using SLM will be between 10^4 and 10^5 °C/s [32], meaning the material is quenched during the printing process.

Between a cooling rate of 410 °C/s and 20 °C/s a big transformation will occur. The fully martensitic structure will gradually be replaced by diffusion controlled α Widmanstätten formation with a decreasing cooling rate [6]. In Ti6Al4V aluminium is an α stabiliser and vanadium is a β stabiliser, creating an α + β dual phase material at room temperature.

This dual phase material is highly dependent on the temperature history and the cooling rate. α + β Dual phase will only exist after a cooling process with a cooling rate below 20 °C/s. When a faster cooling process is used, more than 410 °C/s, from a temperature above the β transus temperature, instead of an α + β dual phase transformation, β will be decomposed by a non-equilibrium martensitic reaction. At 850 °C the α fraction in the material will be fairly high and the cooling rate will have little influence. When the temperature rises the amount of primary α phase will decrease and the influence of cooling rate will increase. At 950 °C the amount of primary α in the material will decrease even more and the cooling rate has an even bigger influence on the final composition of the microstructure.

The difference in needle size, when the material is quenched in water or slowly cooled using furnace cooling, is around 35%. During quenching in water the cooling rate is too high for grain growth to occur. Furnace cooling allows the grains to grow during cooling. Cooling rate becomes very important above the β transus temperature, because this will determine the final dimensions and morphology of the α phase. When the cooling rate is high many small nuclei will form, which will result in a small α colony size and smaller spaces between grains. Lamellar α + β will form during slow furnace cooling, while during air cooling an α Widmanstätten microstructure or basket weave-structure will form. Moreover during water quenching the cooling rate will be higher than 410 °C/s creating an α martensite structure. The β grains at high temperatures will be transformed into lamellar α + β during cooling. The lamellar spacing will decrease with increasing cooling rate and the thickness of the α grain boundary will also decrease with increasing cooling rate. As mentioned before when cooling from above the β transus temperature the cooling rate determines the size of the α colony, but the size of the α colony is limited by the size of the β grain it originates in [103].

Hot isostatic pressing

Hot isostatic pressing (HIP) is a heat treatment method, which can be used to heat treat Ti6Al4V. A schematic overview of a HIP process is shown in Figure 2.11. The heat treatment will change the mechanical properties and drastically increase the fatigue life of the material. This heat treatment will reduce the internal pore sizes in the material [66]. These pores are

reduced due to the heat and pressure by a combination of plastic deformation, creep and diffusion bonding. As-built samples with complex geometries will lose some shape accuracy when subjected to HIP and a consistent uniform microstructure is hard to obtain for complex shapes. In addition, using HIP increases the cost of production significantly [66]. The HIP process uses both an elevated temperature and an isostatic gas pressure in a pressure vessel to post heat treat different samples. The atmosphere in the pressure vessel will most of the times consists of argon which is an inert gas. Heating will already increase the pressure, but additional gas pumping can be used to further increase the pressure in the pressure vessel. For Ti6Al4V the pressure will mostly be kept at 100 MPa or 1000 bar and a temperature slightly below or above the β transus temperature [55].

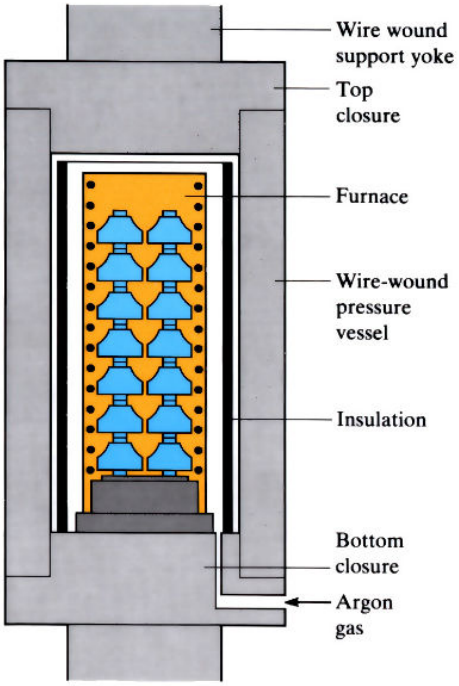

Figure 2.11: Schematic overview of a hot isostatic pressing process [59].

Vacuum oven

When using other heat treatments than HIP it is important to create an inert atmosphere, which will not react with Ti6Al4V at high temperatures. One way to do this is to put the material in a vacuum case and then heat the case. A quartz tube can be used to create a vacuum atmosphere and this tube can then be heated to high temperatures. Heating rates of about 10 °C/min are used to heat the quartz tube, after which it will be kept at a temperature around the β transus temperature for an extended period of time. To get different cooling rates there are three possibilities: using furnace cooling you can create a very low cooling rate; air cooling in a room temperature environment will lead to a cooling rate of about 7 °C/s; and for water quenching the tube will be broken and the samples will fall in the water, cooling to room temperature in a matter of seconds. It is also possible to do the heat treatment in an argon atmosphere like HIP, but without the high pressure. This reduces the time it takes to create a vacuum. When using air, the water in the air will coat the wall and it takes a while to pump this off [98][103].

Discussion heat treatment

As discussed, during heat treatment the heating time, cooling rate and temperature will have a big influence on the resulting mechanical properties. Several papers are consulted to understand the effect of heating time, cooling rate and temperature on the Young's modulus, yield strength, α grain thickness and the amount of β phase which is shown in Table 2.4. All the papers work with 3D printed Ti6Al4V made from either grade 5 or grade 23 ELI powder. The difference between the powders is a smaller percentage of contaminations in the grade 5 powder. Most samples tested are solid but some are printed with a lattice structure which resembles a BCC structure or a diamond structure. The effects of heating time, cooling rate and temperature are investigated for HIP, vacuum heat treatment and heat treatment using an argon atmosphere. Finally, the cooling rate is grouped under furnace cooling (FC), air cooling (AC) or water quenching (WQ).

Table 2.4: Comparison of selected studies and the effect of heat treatment on the mechanical properties of 3D printed Ti6Al4V.

Ref	Grade	Structure	Method	Temperature	Time	Cooling rate	α grain thickness	E(GPa)	yield (MPa)	β fraction
[103]	23	solid	Vacuum	850	2h	10 °C/min	1.27 ± 0.13	114.7 ± 3.6	955 ± 6	$10.7 \pm 0.9\%$
					2h	AC	1.22 ± 0.09			
					2h	WQ	1.16 ± 0.13			
				950	2h	10 °C/min	2.23 ± 0.12			
					2h	AC	1.57 ± 0.21			
					2h	WQ	1.48 ± 0.14			
				1020	2h	10 °C/min		114.7 ± 0.9	760 ± 19	
[27]	5	solid	vacuum	950	1h	FC			1248	
[63]	5	solid	Argon	AP	-	-		130	1156	0
				800	4h	AC		118	986	35.2
				850	4h	AC		115	973	33.9
				900	4h	AC		107	895	31.6
[123]	5	porous BCC	Argon	AP	-	-		1.52 ± 0.10	50 ± 11	0
				800	2h	AC		1.42 ± 0.06	44 ± 1	5.9
				800	2h	FC		1.86 ± 0.23	60 ± 13	4.7
				900	2h	AC		1.71 ± 0.39	57 ± 14	6.4
				900	2h	FC		1.70 ± 0.23	53 ± 6	5.4
[120]	23	solid	Vacuum	AP	-	-	0.89	120.1	1062	
				800	2h	FC	-	117.5	996	
				900	2h	FC	3.09	116.2	869	
				920	2h	FC	-	115.8	850	
				950	2h	FC	-	116.7	837	
				1080	2h	FC	-	117.1	840	
			HIP	900	2h	FC	2.61	115.3	839	
[5]	5	Diamond	AP	-	-	-	2.2 ± 1.4			
			HIP	920	2h	FC	8.7 ± 5.1			
[60]	23	Solid	AP	-	-	-			1008	
			Argon	800	2h	FC			962	
			Vacuum	1050	2h	FC			798	
			HIP	920	2h	FC			912	
[90]	23	Solid	AP	-	-	-		109.9	736	
			Vacuum	700	1h	FC		117.4	1051	
				900	2h	FC		118.8	988	
			HIP	900	2h	FC		115.4	973	

When looking at the Young's modulus in Table 2.4, it is observed that the Young's modulus of the material decreases when the temperature of the heat treatment is increased. This could be linked to the observed increase in α grain thickness with increasing temperature. When the cooling rate is increased the Young's modulus will also increase. Again this can be linked to the α grain thickness, which reduces with an increasing cooling rate. The percentage of β phase could also affect the Young's modulus, because the β phase has a lower Young's modulus compared to the α phase. The temperature and cooling rate does not seem to significantly influence the β phase fraction, however, the heating time does seem to influence the β phase fraction. Now comparing the different heat treatment methods it appears that no significant change in Young's modulus is found between the three methods. Looking at the yield strength it can be clearly seen this is linked to the measured Young's modulus. An increase in Young's modulus will also result in an increase in yield strength, which will result in the same conclusions for the yield strength compared to the Young's modulus.

From Table 2.4 the heat treatment method does not seem to affect the measured mechanical properties, but there is one big difference between HIP and vacuum or argon heat treatment. After 3D printing the material will have a large amount of internal pores. HIP is performed under a pressure of 1000 bar, which is expected to influence the size of the internal pores. In Table 2.5 a comparison in made between the internal porosity and different heat treatments.

Table 2.5: Comparison of selected studies and the effect of heat treatment on the internal porosity of 3D printed Ti6Al4V.

Ref	Grade	Printing method	Heat treatment	Temperature (°C)	Time (h)	Internal porosity (%)
[5]	5	SLM	AP	-	-	1.2 ± 0.6
			Argon	800	2.5	1.3 ± 0.7
			HIP	920	2	0.1 ± 0.1
			Argon	1050	2	1.4 ± 0.6
[36]	23	SLM	AP	-	-	0 - 5
		EBM	AP	-	-	0 - 5
[120]	23	SLM	AP	-	-	0.025
			Argon	900	2	0.021
			HIP	920	2	0
[45]	23	EBM	AP	-	-	0.2
			HIP	900	2	0
[90]	23	SLM	AP	-	-	0.6 ± 0.2

The effect of HIP on the internal porosity is clearly seen in Table 2.5. In one paper the internal porosity after HIP is less than 10% of the original internal porosity and in other papers the internal porosity after HIP is not even measurable anymore. When comparing the as-processed samples with the argon heat treated samples no significant changes of the internal porosity can be seen. From this data it can be concluded that the internal porosity is affected by HIP, but not by heat treatment with argon. Vacuum heat treatment is also not expected to reduce the internal pore size.

This difference in internal porosity does not seem to have a large influence on the Young's

modulus and the yield strength, but can have a large influence on the fatigue life of the material. In Figure 2.12 three fatigue graphs are shown. The as-built graph did not receive any post heat treatment, the HT 900 graph received an argon heat treatment for 2 hours at 900 °C and the HIP graph received HIP for 2 hours at 900 °C. It can be seen that argon heat treatment will increase the fatigue life significantly, but this improvement will be even better when HIP is used.

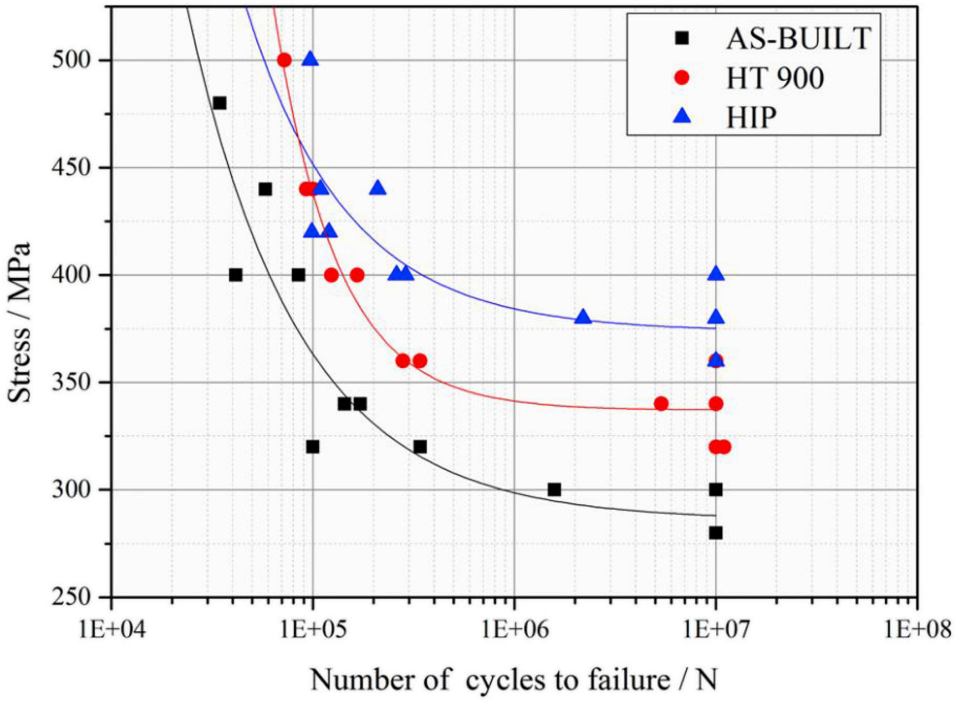

Figure 2.12: S-N curves of SLM Ti6Al4V heat treated in several conditions [120].

This additional improvement of the fatigue life can be attributed to the reduction of the size of the internal pores. However, crack initiation was not found at the internal pores, but at the subsurface of the samples. The internal pores are expected to stimulate the crack propagation rate, because no internal pores can be detected on the fracture surface of the HIP samples [120].

The fatigue graphs created in Figure 2.12 are created by testing solid 3D printed Ti6Al4V. Nowadays, many medical applications use 3D printing to create a lattice structure from Ti6Al4V, which can result in lowering the stiffness and allowing bone to grow into the material. By creating a lattice structure the surface area will drastically increase and in a lattice structure made of many struts, cracks are only able to cause failure in one strut instead of the entire sample. In Figure 2.13 several fatigue graphs are shown from samples printed with a diamond lattice structure. The AP samples did not receive any post heat treatment, the T800 and T1050 samples were heat treated using an argon atmosphere at 800 °C and 1050 °C, respectively and the HIP samples are heat treated using HIP. In addition some samples did receive chemical etching (CE) or sandblasting (SB) as surface treatment.

When comparing AP, T800, T1050 and HIP it is interesting to see that applying a heat treatment will improve the fatigue life significantly, but between the heat treatments no difference in fatigue life can be concluded as the graphs almost perfectly overlap. It could be possible this is due to the increased surface area, which dominates the fatigue life compared to the effect of the internal pores. When comparing the sandblasted graphs (AP+SB, T800+SB, T1050+SB and HIP+SB) at 1,000,000 cycles it can be seen that the heat treated samples still perform

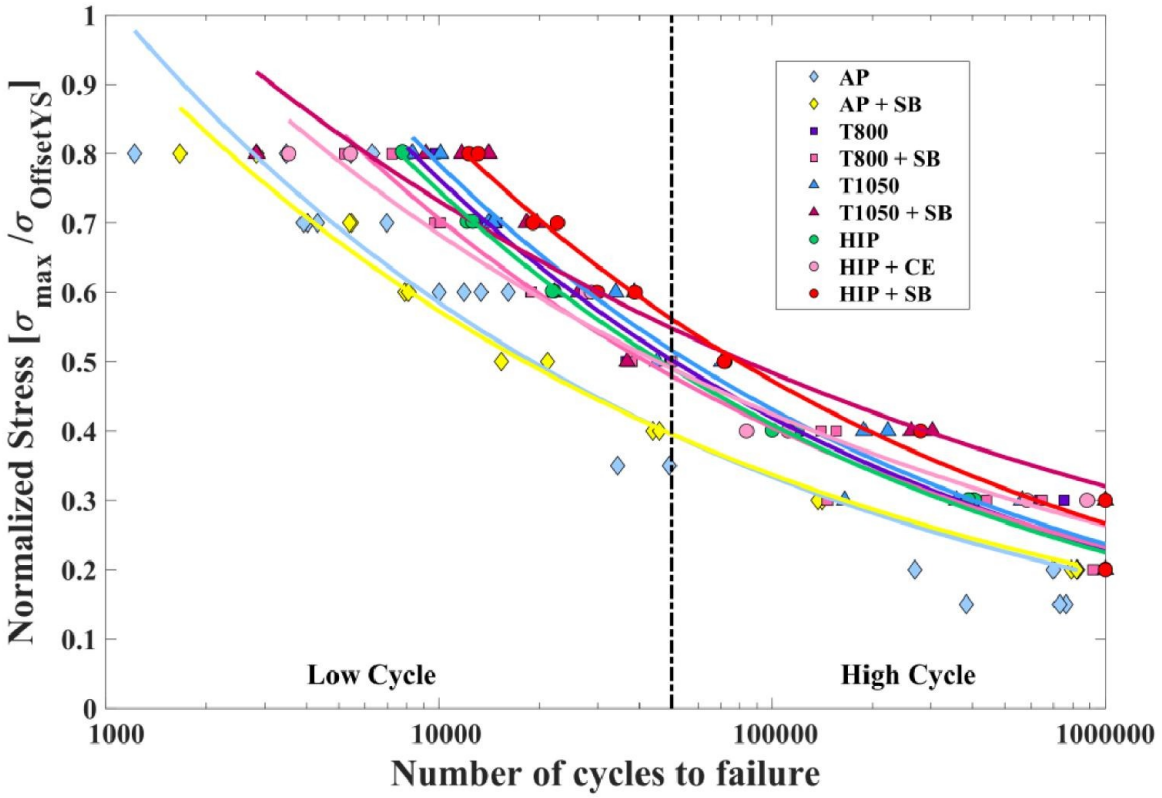

Figure 2.13: S-N curves of SLM Ti6Al4V heat treated in several conditions [5].

better compared to the as-processed samples, the T800+SB and HIP+SB samples overlap at 1,000,000 cycles and the T1050+SB samples have the best fatigue life. However, at a lower amount of cycles HIP+SB does seem to have the best fatigue life. The samples which are chemically etched show a decreased fatigue life. However, Karimi et al. [49] showed that the best fatigue life is achieved using a combination of sandblasting and chemical etching. It now looks like the benefit of reducing the pores using HIP is not notable any more at a high number of cycles. This makes it interesting to investigate the effect of different heat treatments on the fatigue life of lattice structures further. It would also be interesting to see the effect of vacuum heat treatment as all the fatigue graphs shown previously are heat treated with either argon or HIP.

2.3.2. Surface modification

To enhance the performance of 3D printed biomaterials, surface modification plays an important role in particular for biocompatibility and fatigue life. Titanium alloys are covered by a thin layer of oxide which provides excellent chemical inertness, oxidation resistance and biocompatibility. As explained before, the surface morphology is important to create an effective bond between the bone and the implant. This surface morphology depends on the history of material processing. During AM processing powder particles tend to become small liquid spheres when heated. These spheres can attach to the surface of the AM sample called the *balling* effect. This will lead to a rough surface with residual powder on it, which will reduce the fatigue life. Furthermore, the spheres can easily detach in the body [106]. Therefore, it is necessary to subject the SLM printed samples to surface post processing. Different methods of surface modification are sandblasting, etching and the use of coatings.

Sandblasting

Cells grown on a sandblasted surface show a round form which predicts good adhesion. A good test to show the relationship between cell growth and the substrate roughness is a proliferation test. A smoother surface will increase the rate at which cells proliferate. A smooth surface is needed for optimised cell adhesion, but also hard tissue must grow, which is activated more rapidly on a rough surface. A rough surface will increase synthesis of the extra cellular-matrix and improve mineralisation [65]. Sandblasted surfaces will induce good cell adhesion and rapid cell differentiation. This rapid cell differentiation in combination with low proliferation rate will generate bone with a low cell density which results in reduced implant stability. It is important to find a compromise between a smooth and a rough surface to get the best result. When sandblasting a complex lattice it can be difficult to reach the surfaces inside the lattice and sand particles can get stuck in the lattice affecting the biocompatibility.

Etching

Using etching it is possible to create a microtexture and nanotexture at the surface which is beneficial for bone formation on the implant. The properties of the textures can be controlled by changing the exposure time and chemical mixture. For etching of Ti6Al4V a combination of H_2SO_4 and H_2O_2 is usually used. During etching β grains surrounded by larger α grains etch more rapidly resulting in a surface with microscale cavities. Etching also creates nanopits at the surface of both the α and the β grains. These nanopits can be visualised by using high-resolution SEM. The roughness of the surface will also increase due to etching. Moreover, a thin oxide layer will form on the surface during etching. The resulting new surface after etching promotes the growth of osteoblasts and inhibits the growth of fibroblast. This makes etching capable of controlling the cell activity in a biological environment [102].

Coatings

Another way to increase the bioactivity on the surface of the implant is to apply a coating. There are several ways to apply coatings. For complex structures dip coating normally gives the best results, but also electrolytic deposition (ED) and plasma spraying are commonly used. Dip coating is often used with the sol-gel method where a metal alkoxide is transformed to a metal hydroxide during hydrolysis. After hydrolysis the hydroxide will condensate on the material creating a complex polymer structure in all directions. This method gives a homogeneous result at low costs.

Using ED a CaP coating is applied, which improves the bioactivity and forms osteoinductive bio-units for the repair of bone defects. Coating using ED will produce a uniform and fully covered surface, making it suitable for the coating of porous surfaces [106]. Radio frequency magnetron sputtering, which is a physical vapour deposition technique, is another method to apply a CaP coating on complex structures [21].

3

Problem statement

This thesis is in collaboration with Amber Implants, a TU Delft start-up which is developing 3D printed implants for medical use. Amber Implants acquired a design of a spinal cage which can be used to perform spinal fusion. During the production of this spinal cage the heat treatment hot isostatic pressing (HIP) is performed, which improves the fatigue life of the spinal cage. However, this heat treatment is expensive to perform, and limited experimental knowledge is available about more affordable heat treatments which can also create the desired mechanical properties and fatigue life. Therefore, it is important to investigate alternative heat treatments.

Mechanical testing was performed on the spinal cage design acquired by Amber Implants, which showed some undesirable qualities [11]. The apparent Young's modulus of the implant is significantly higher compared to the Young's modulus of the vertebrae. During compression stress shielding occurred, resulting in most of the applied force being transferred through the back of the implant, causing failure at that location as seen in Figure 3.1a. Furthermore, during fatigue testing crack initiation occurred at the interface between porous and solid Ti6Al4V and crack growth continued through the porous material which is sandwiched between solid material as seen in Figure 3.1b.

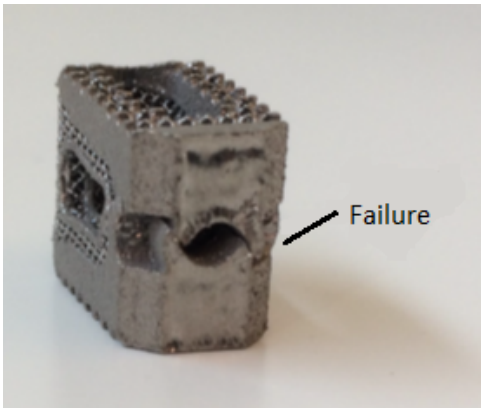

(a) Mechanical failure of a spinal cage

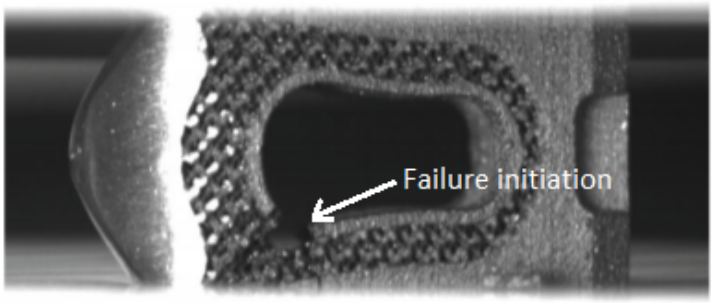

(b) Fatigue failure of a spinal cage

Figure 3.1: Mechanical tests performed by Adriaan Blok in cooperation with Amber Implants [11].

This spinal cage used by Amber Implants is designed for a very wide range of patients, so it can be used universally. Because of the universal application the design process was limited by constraints, like yield stress, fatigue life, apparent Young's modulus and size, which do not

apply for all patients. By designing spinal cages for different patient specific groups, a patient can obtain a more suitable spinal cage for his/her physique and lifestyle, which improves the success rate of spinal fusion.

3.1. Research questions

The problems regarding heat treatment and the current design of the spinal cage led to the following research questions:

- How does an alternative heat treatment without high pressure affect the fatigue life and strength, whilst still meeting the material requirements for spinal cages?
- How will design changes of the spinal cage affect stress shielding, the apparent Young's modulus, yield stress and the fatigue life?
- How much does creating patient specific groups change the mechanical properties of the spinal cage to improve the spinal fusion process?

3.2. Objectives

In order to be able to answer these research questions, the following objectives are formulated:

- Find how a vacuum heat treatment will affect the Young's modulus, yield strength, fatigue life and microstructure at two different temperatures.
- Find how the current spinal cage design can be optimised and use FEM software to investigate the change in mechanical properties.
- Make sure the spinal cage meets the three main requirements, which are having an α + β microstructure; no yielding when a force of 2000 N is applied; and no fatigue failure after 5 million cycles at 600 N with an R-ratio of 0.1.
- Find the difference in mechanical properties of the original and newly designed spinal cage.
- Divide the patients with a spinal cage in 5 different patient specific groups and find the requirements for each group.
- Investigate how the group specific requirements affect the mechanical properties of a group specific spinal cage using FEM software.
- Apply several mechanical test on spinal cages to validate the simulations of the FEM software.

4

Methods

In this chapter the methods are discussed, which consists of three main parts. Firstly, the design methods are discussed, which includes the method of creating different patient specific groups. Then the modelling methods are discussed, which is based on a finite element method (FEM). Finally, the experimental methods are discussed.

4.1. Design

4.1.1. Original design

The original design is shown in Figure 4.1, where the brown colour represents solid Ti6Al4V and the grey colour porous Ti6Al4V. The presence of the porous material lowers the apparent Young's modulus of the implant for it to more closely resemble the Young's modulus of bone and to allow the bone to grow into the implant. The implant design has a solid tip for easy insertion and a solid back so the implant can be gripped during insertion. Teeth are present at the contact points between the implant and the vertebrae to prevent slippage. There are two main holes in the implant which intersect in the middle of the spinal cage, one vertical and one horizontal. These holes allow allo or auto grafts to be added to the implant in order to improve the fusion process.

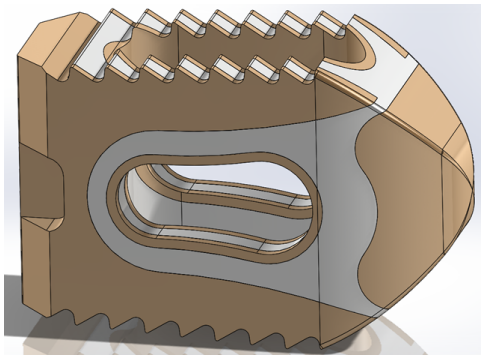

Figure 4.1: SolidWorks model of the current PLIF design (Amber Implants).

The objectives of this section is to find methods in order to optimise the current design as acquired by Amber Implants and to develop an approach on how the spinal cage can be made patient specific. This is done by taking into account the general requirements of a spinal cage, as explained in Section 2.1 and by looking at design specific requirements and

constraints, which will be explained in the next subsection. This will be followed by a review on the optimisation of the current design and finally the patient specific groups will be looked into, as well as methods to change the design in order to make it patient specific.

4.1.2. Constraints

A spinal cage is a medical device with the main function of being able to fuse two vertebrae together, which will be implanted into a human body. The design of such implant therefore comes with certain constraints. As discussed in Section 2.1 the spinal cage should be biocompatible and meet certain criteria, which are summarised in Table 2.3.

When looking at the design constraints of the spinal cage, it is important that the design should be producible using available technology of which the SLM process is preferred. Furthermore, it is important to consider how the spinal cage will be implanted. A spinal cage can be implanted between the vertebrae from the anterior or the posterior. Implanting from the anterior, the spinal cage will move through the abdomen making it a very invasive surgery. However, this gives the whole surface area between the two vertebrae as the size constraint, instead of the smaller area available with posterior implantation. Implanting from the posterior is less invasive, but most of the time two spinal cages inserted from both sides of the spinal cord are needed to achieve the same result. This puts a bigger restriction on the size of the spinal cage.

Another important factor to consider are the regulations regarding medical implants. In the USA it is easier to get your product on the marked by getting a 510(k) approval, because to get this approval your implant has to be similar to a product which has already been proven successful and no expensive clinical studies are necessary. This means it can be useful to change a design to make it more similar to an already existing spinal cage, which can save a lot of time and money for getting the spinal cage approved.

Finally, other design requirements which have to be considered are regarding the function of the spinal cage. There should be porous material, or room for allo and/or auto grafts in order for bone ingrowth to occur. Furthermore, for easy insertion of the implant, there should be a smooth solid tip and for easy gripping there should be a solid back, which can be easily gripped by equipment of a surgeon.

4.1.3. Optimisation of the current design

As shown previously in Figure 4.1 Amber Implants acquired a design for a spinal implant. However, this design is still open for improvement as the results of the mechanical testing performed by A. Blok [11] show. To improve the current spinal cage we will look into the results of the fatigue testing and the compression tests.

During fatigue testing the spinal cage starts failing at the same spot every time at the solid-porous interface [11]. This fracture moves from the centre of the implant to the outer edge through the porous material, neighbouring the solid parts, which is shown in Figure 4.2 and 4.3. Because there is a small strip of porous material between two stiffer solid parts, high stress concentrations are expected at this location. Using design optimisation, stress concentrations between the solid and the porous material can be reduced for an improved spinal cage.

During compression tests a different way of failure was found. As shown in Figure 4.4 the implant fractures at the back where normally the implant is gripped during insertion. When looking at the current design it is seen that the back of the implant is completely made of solid material, which is much stiffer than the porous material, resulting in most of the load being carried by the back of the implant. Furthermore, the current design shows teeth at the top and bottom surfaces to improve fixation when implanted. During testing the teeth will either sink

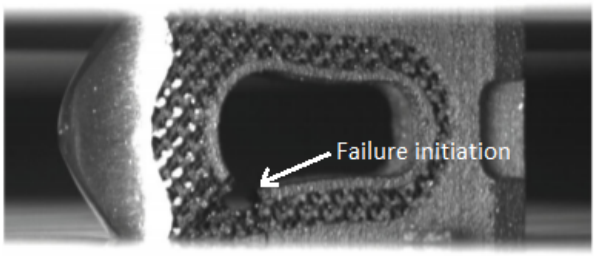

Figure 4.2: Fatigue failure of a spinal cage [11].

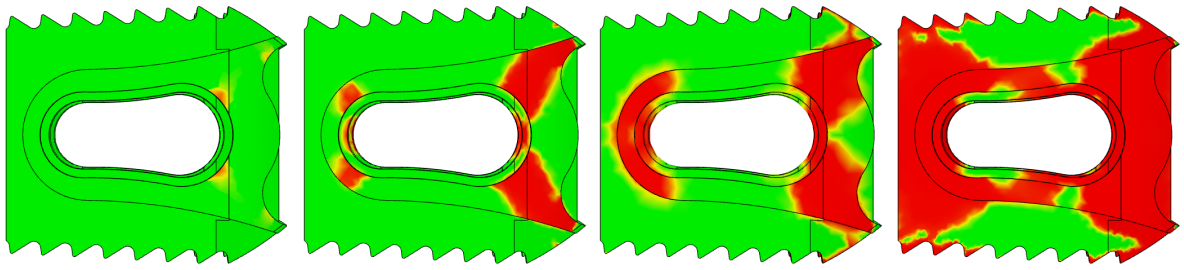

Figure 4.3: Visualisation of the growth of fatigue failure with increasing load cycles applied. The red and orange colour represent fatigue failure.

in the test set-up or will fail quickly due to the applied force. Because there are no teeth at the back end of the implant, this will not be compressed or sink in the test set-up, causing more force to be transferred through the back, leading to premature failure.

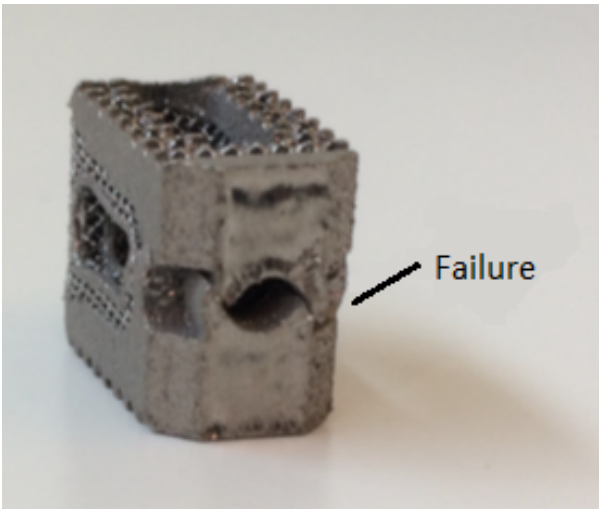

Figure 4.4: Mechanical failure of a spinal cage [11].

Apparent Young's modulus

When improving these weak spots, the fatigue life and yield strength will increase, generating the possibility of removing some support features. This will lead to another big improvement that can be made, which is reducing the apparent Young's modulus of the implant. The apparent Young's modulus is defined as the measured Young's modulus which can be different compared to the true Young's modulus in for example porous structures [93]. The Young's modulus of the bone is currently much lower than the apparent Young's modulus of the im-

plant, around 20 times lower, therefore approaching this value as close as possible is important for effective load transfer and alleviating the stress shielding effect [106]. One way to do this is by reducing the solid-porous ratio and by redistributing the solid material.

When an implant possesses a very high apparent Young's modulus compared to the surrounding bone this may lead to the implant penetrating into the interior vertebra in a process called subsidence. This is also a risk when implanting a metallic spinal cage between the vertebrae. Many metal based implants like titanium, stainless steel and cobalt-chrome have a significantly higher modulus compared to PEEK implants and allo graft bone, making metallic implants more susceptible to subsidence [41].

Another problem which can occur is stress shielding. When a spinal cage is implanted between the vertebrae, bone will grow into the porous structure of the implant. In some spinal cages it can occur that the solid frame of the implant will support most of the load bypassing the porous structure. Wolff's law stipulates that too little loading in the porous region can cause bone resorption. On the other hand higher loading will stimulate bone formation. The stress shielding caused by the solid parts results in bone resorption and therefore implant loosening [41].

To reduce the apparent Young's modulus and prevent stress shielding it would be ideal to create an implant completely made of a porous material. It has already been proven that by implanting a porous implant between sheep vertebrae the fusion succeeds without failure of the implant. However, of course, this is not the same as human implantation, because of the upright posture of the humans causing more load to be applied to the spinal implant [112]. The completely porous implant must still reach the desired fatigue life and yield strength. The tip and edges of the current design of the implant are solid to reduce difficulty during insertion. For future designs a solid tip and edges should also be incorporated to prevent unnecessary damages to the vertebrae during insertion.

The creation of patient specific designs will also generate the possibility of reducing the apparent Young's modulus even more. For a patient specific group where the cyclic load and the peak load are lower compared to other groups, the strength of the implant can be lower, which gives the opportunity to reduce the apparent Young's modulus of the implant to more closely resemble the Young's modulus of the bone.

Integration of allo and auto grafts

Most procedures involving spinal cages still use allo and/or auto grafts, which are added to the spinal cage to improve the spinal fusion. The use of allo and/or auto grafts makes the procedure more invasive and more difficult, so eliminating this will be desired. Recent studies suggest that inter-vertebral cages made of titanium with a high porosity could achieve inter-vertebral fusion without using bone grafts [95][112] [118]. This would have significant clinical benefits for patients by eliminating invasive bone harvesting procedures, which have a high complication rate.

Further research and experience is still needed to proof the effectiveness of spinal cage implantation without bone graft in humans. For this research the choice is made to proceed with designing an implant which does not contain any holes for allo and auto grafts, which creates a wider range of design possibilities. One disadvantage of not using allo or auto grafts could be an increased time to achieve complete spinal fusion, but because the operation itself is less invasive a choice can be made by the patient for the preferred method. The actual difference in time until complete fusion is not very well known yet.

Fixation

Many implants are completely made of solid material, which can create a smooth outer surface. Most vertebrae are not parallel to each other, resulting in an angle between the vertebrae.

When a load is applied under an angle to a spinal cage with a smooth surface slip can occur. To reduce the chance of slip, teeth are added to the surface of the implant. However, lots of new implants consist partly of a porous material and looking at the surface of this porous material in Figure 4.5 it is shown that it has a rough surface structure.

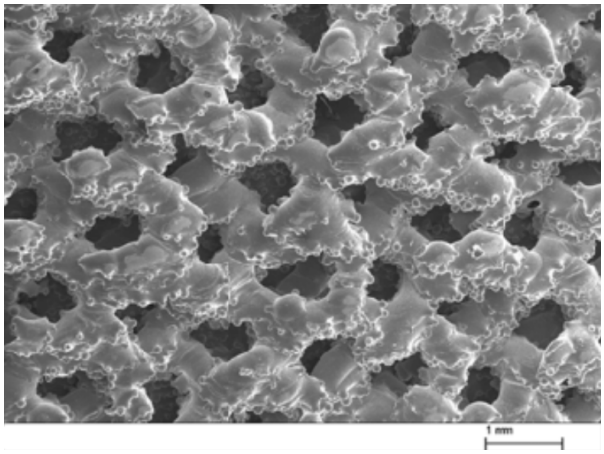

Figure 4.5: SEM image of ALM surface structures of Ti6Al4V [12]

During studies with porous implants without any teeth, none show any signs of slip. Also by reviewing failure of existing implants under instability at the FDA the main causes found of instability are wrong implant size or wrong insertion. No cases of slip were recorded. Therefore, the addition of teeth on porous implants seems redundant and seems to be only there to give the implant a safer impression. Other implant companies have also moved towards implants without teeth and without the addition of allo or auto grafts, as shown in Figure 4.6.

Figure 4.6: An FDA approved TLIF implant made by GmbH (EIT) [72].

Solid-porous interface

At the interface of the solid and porous material notches can be created causing stress intensification. This stress intensification makes the material susceptible to crack initiation. Similar to a solid-porous interface, a sintered interface also experiences stress intensification at notches between the sintered material and the substrate.

SEM images taken from a sintered material show that cracks often occur a small distance away from the stress initiating notch. This means that crack initiation not only depends on the stress intensification, but also on the microstructure in this highly stressed region. The

crack initiation sites will lower the fatigue life of the implant. The solid part and the porous part of the implant are made from the same material, but the porous part will behave differently. The elastics modulus of the porous part will be different to the solid part creating an elastic modulus mismatch. The following formula can be used to calculate the elastic modulus for the porous material where ρ is the relative density. The relative density is defined as the ratio of the density of the porous material to the density of the corresponding solid material [3].

$$E_{porous} = \frac{(0.46 + 0.17\rho)\rho^2}{(0.46 + 1.17\rho)(3.85 + 1.14\rho)} E_{solid} \tag{4.1}$$

The elastic modulus mismatch causes a shear stress in the material when loaded, which in turn causes the initiation of cracks and crack propagation at the interface, eventually resulting in interface debonding [3][46][76].

Implant dimensions

For the 510(k) approval as discussed in Section 4.1.2, it is useful to change a design in order to make it more similar to an already existing spinal cage. This can save a lot of money when getting the spinal cage approved. Therefore, for the PLIF design the same outer dimensions are taken as the original design shown in Figure 4.7. To see all the dimension please look in the Appendix.

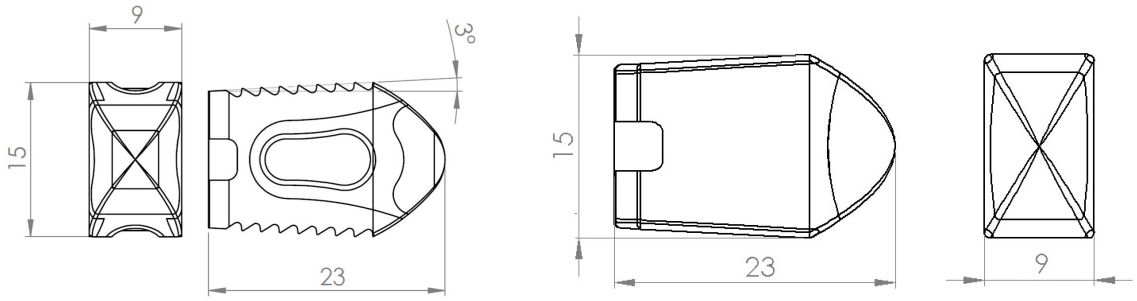

(a) Old PLIF design.

(b) New PLIF design.

Figure 4.7: Dimensions of the original and new PLIF design given in mm.

Production process

Another way to achieve the desired mechanical properties which were not the focus of the research presented in this thesis is by looking at the production process. During the production process the mechanical properties of the implant will be influenced. By altering the production processes, such as 3D printing, heat treatment, sandblasting and etching, it is possible to achieve different printing qualities, surface finishes and microstructures. All these material properties have a large effect on the fatigue life, yield strength and the osseointegration of the implant. Different printing qualities, like hardness, internal porosity and surface quality, can be obtained by changing the parameters of the printing process, such as laser power, scan speed, hatch space and scan angle or by choosing different printing processes such as SLM or EBM. The surface finish depends on the printing process, but also on post processing like sandblasting and etching. The microstructure can be changed by applying a post heat treatment.

4.1.4. Patient specific design

AM technologies make it possible to produce porous metallic implants with complex and customised structures. This means it is possible for every patient to get their own customised

spinal cage. However, designing and 3D printing for each and every patient independently is not cost competitive. Even though this could change when technology improves it has been decided for this research to focus on creating five different spinal cages which will meet the demands of five different patient groups. This will not have the same result as creating a spinal cage for every individual patient, but it will improve the result for patients, because there will be a more suitable choice.

In order to create five different patient specific groups it is important to find all the variables that make the different patients unique. These variables can vary between mechanical properties of the bone, dimensions, age, sex, damage and many more. A list of these variables is presented in Table 4.1.

As shown an optimal spinal cage design is influenced by many different variables. It is important, in order to simplify the design process, to reduce this number of variables. In this review it was found that all these variables can be grouped together in 5 main variables, which will be called parameters. These are the parameters: *load, T-score, time, pore size* and *dimensions*. Note that it will be possible for a variable to influence multiple parameters.

Load When designing a spinal cage it is important to know all the loads applied on the spinal cage. Peak forces should not exceed the yield stress of the spinal cage. During most daily activities the spinal cage will be subjected to a cyclic load, for which a certain fatigue life should be achieved. Apart from the properties of the spinal cage, the fatigue life will depend on the age, body weight and activity of the patient. The size of the vertebra determines the maximum possible dimensions of the spinal cage, which will influence the load distribution. Finally, the angle between the vertebrae will determine the amount of shear stress in the implant and the needed amount of friction between the implant and the vertebra. This results in the following variables grouped together under the parameter *load*: age, peak forces, cyclic forces, product life cycle, body weight, angle and vertebra size, of which an overview is given in Table 4.2.

T-score The T-score shows how much the patient's bone density is higher or lower than the bone density of a healthy 30-year old male adult. Scores above -1 (-1 times the standard deviation (SD)) are considered healthy. Scores between -1 and -2.5 are considered osteopanea and scores below -2.5 (-2.5 times the SD) are considered osteoporotic. One time the SD can be compared to a decrease of about 10 to 12% of the bone mineral density (BMD). Thus T-score describes the relative bone density. Using the bone mineral density it is possible to estimate the bone strength and the Young's modulus of the bone. The gender of the patient also has an influence on the estimated mechanical properties of the bone. Women usually have a lower bone density compared to men and this makes them more susceptible to osteopanea and osteoporosis. Moreover, menopause has a big influence on the decrease in bone density. There are several diseases which can affect the bone density and also a fracture will reduce the bone density. The maximum decrease in bone density due to a fracture can be 13%. This results in the following variables grouped together under the parameter *T-score*: age, gender, bone strength, bone density, bone Young's modulus, disease, fracture and menopause, of which an overview is given in Table 4.2.

Time The mechanical properties and structure needed for a spinal cage will also depend on time. Normally complete fusion of the vertebrae will be completed after 3 to 6 months after which the bone can support itself. The spinal cage should be able to withstand any mechanical loads until its support is not needed anymore. After fusion the implant will remain in the body,

Table 4.1: Variables which affect the optimal spinal cage design. Note: x is the age in years, and UTS is the ultimate tensile strength.

Variables	**Values**	**Source**
Age (**x**)	**x** taken in years between 20 and 90	[74]
Gender	See other parameters	[74]
Peak forces	Average force on vertebrae during comfortable lifting Female: 1671 N Male: 2080 N	[15]
Cyclic forces	50 - 150 % of body weight	[7]
Lumbar vertebrae UTS	Male: -99.78x + 11006 N Female: -76.94x + 8864 N	[73][74][85]
Bone density	Female: -1.3x + 214 kg/m^3 (Ash density) Male: -1.1x + 200 kg/m^3 Osteoporotic: Density: $60 - 90$ kg/m^3 Describing the bone density of males with a linear graph is relatively accurate, but for females this is not the case. Females have a close to linear reduction of bone density until the menopause, where a high decrease of bone density is observed. After this large decrease, the bone density stays almost stable during ageing.	[10][15][73] [74]
Bone Young's modulus	Increases due to mineralisation Decreases due to density decrease Increase with increasing force Male 25% higher than female	[10][14][18] [58][91][121]
Speed bone ingrowth	3 to 6 months until fusion of two vertebrae	[100]
Life cycle	After a certain time the bone can support itself, so no mechanical strength from the implant is needed. Corrosion is still a problem which stimulates osteolytic cytokines. Vanadium, titanium and aluminium ions which are released by the implant all reach plateau concentrations in the body after 8 years	[50][110]
Disease	Osteoporosis (see bone density) Fracture (see fracture)	
Fracture	Maximum recorded density decrease is 13% Fracture will be fully recovered after 1 year	[29][56][99]
Pore size	No age or bone quality related optimal pore size is found	
Menopause	See density and bone strength	
Body weight	Female: 0.027x + 56.1 kg Male: -0.257x + 87.1 kg	[73]
Angle	Angle between L2 and L3 is between 0 and 15° Average: 6.89°	[23]
Vertebrae size	L3 upper vertebrae width Female: 40.9 $\pm$ 3.6 mm Male: 46.1 $\pm$ 3.2 mm	[23]

so biocompatibility should remain over time. Age and gender will both affect the speed of bone formation resulting in different completion times for complete fusion. This results in the following variables grouped together under the parameter *time*: age, gender, speed bone ingrowth and product life cycle, of which an overview is given in Table 4.2.

Pore size As discussed before the pore size is important for optimal performance. Small pores create a bigger surface area for bone growth, but larger pores increase vascularisation. A larger pore size will also increase permeability which is necessary, because transportation of cells, nutrients and growth factors requires the blood to flow through the implant. The quality of the blood and the quality of the bone will both affect the ideal pore size. This results in the following variables grouped together under the parameter *pore size*: age, bone density and and bone Young's modulus, of which an overview is given in Table 4.2.

Dimensions For the final parameter *dimensions* is chosen. The limitations in spinal cage design is greatly affected by the size of the vertebra. When the vertebra has a bigger surface area it is possible to create a spinal cage with a bigger surface area, which is able to carry a higher load without compromising the apparent Young's modulus of the implant. The height between two vertebrae also affects the implant design. The angle between L2 and L3 can be between 0 and 15°. This variation in angle will determine the amount of shear stress in the implant and also the amount of friction which is needed to keep the implant in place. This results in the following variables grouped together under the parameter *dimensions*: angle and vertebra size, of which an overview is given in Table 4.2.

Table 4.2: An overview of the 5 parameters load, T-score, time, pore size and dimensions and their corresponding variables.

	Load	**T-score**	**Time**	**Pore Size**	**Dimensions**
Age	x	x	x	x	
Gender		x	x		
Peak forces	x				
Cyclic forces	x				
Lumbar vertebrae UTS		x			
Bone density		x		x	
Bone Young's modulus		x		x	
Speed bone ingrowth			x		
Product life cycle	x		x		
Disease		x			
Fracture		x			
Menopause		x			
Body weight	x				
Angle	x				x
Vertebra size	x				x

Groups

There are now five different parameters: *load, T-score, time, pore size* and *dimension*. This is still too much if all these parameters are variable and only five patient specific groups can be formed. A solution to this problem is by seeing if some parameters can be taken constant. The first parameter, *time*, can be taken constant, because it normally takes 3 to 6 months before the bone can support itself, therefore for every patient specific design it is important for the spinal cage to not fail within the upper limit of 6 months. Furthermore, the *pore size* can be taken constant, because current research is still in disagreement about what the perfect pore size is and only small differences in successful osseointegration is noticed for different pore sizes. This difference in successful osseointegreation will often level off after some time.

The parameter *dimensions* is harder to take as a constant. The dimensions can be compensated slightly by increasing or decreasing the space between the vertebrae and by scraping away some of the bone. By scraping away some of the bone there can also be a correction for the angle of the implant. In current spinal cage procedures scraping of the bone is used to create a perfect fit. The vertebrae size and angle will be used as an input for the division of the patients in different groups, but will not influence the creation of these groups. For example, someone with a bigger vertebra needs a bigger implant which will reduce the stress on this implant if the load remains the same, resulting in the ability to handle higher loads. With a larger angle between the vertebrae the shear stress increases and the implant has to be stronger to handle the extra shear stresses, which can be comparable to someone with a smaller angle but higher cyclic loads. To make this work a relation has to be found between fatigue life versus increased load and fatigue life versus increased shear stress.

Now only two parameters remain, which will be used to divide the patients in five different groups: *load* and *T-score*. The cut off values for these parameters will be categorised in such a way that roughly 20% of the patients will be assigned to each group. For the parameter T-score three value ranges are picked. Above -1, which means you will be classified as healthy, between -1 and -2.5, which is classified as osteopanea and below -2.5, which is classified as osteoporotic. Now there are three different groups created. To create the final two groups the parameter load is used, cyclic load to be more specific. For osteoporotic patients the same cyclic load is used. Patients classified as healthy and as having osteopanea will both be divided into two different load groups. The cyclic load is calculated using body weight and by using the T-score of these patients an expected age group can be formed. From this age group the average body weight for western people is used to calculate the cyclic load and make the division. In Table 4.3 the five different groups depending on the T-score and cyclic load are shown. Also added in this table is the expected BMD, ultimate tensile strength (UTS) and age, which can be found using the T-score [7][10][15][73][74]. The peak load, cyclic load and percentage of patients can be found using the age of the patients.

In literature a 4000 N axial force is advised as reference load, which will be in this case 2000 N per spinal cage, because two spinal cages are used per patient. For the cyclic load 600 N is advised for testing on one spinal cage [28][47]. This finally resulted in the following values, which can be seen in Table 4.4 used as maximum loads for the patient specific groups.

Several techniques can be used to achieve patient specific designs for the five groups which were developed above. For a patient specific group where the cyclic load and the peak load are lower compared to other groups, the strength of the implant can be lower, which gives the opportunity to reduce the apparent Young's modulus of the implant to more closely resemble the Young's modulus of the bone.

Table 4.3: Division in patient specific groups and the resulting values.

	T-score	BMD (g/cm3)	UTS (N)	Age (years)	Peak load	**Cyclic load**	Patients
Group 1	**>-1**	>0.98	>4600	F: >20, <55 M: >20, <80	>2000N	**>750N**	26.35%
Group 2	**>-1**	>0.98	>4600	F: >20, <55 M: >20, <80	>2000N	**<750N**	26.35%
Group 3	**>-2.5** & **<-1**	>0.85 & <0.98	<4600	F: >55, <65 M: >80, <90	<2000N	**>750N**	16.4%
Group 4	**>-2.5** & **<-1**	>0.85 & <0.98	<4600	F: >55, <65 M: >80, <90	<2000N	**<750N**	16.4%
Group 5	**<-2.5**	<0.85	<3800	F: >65, <90	<1800N	**<700N**	14.5%

Table 4.4: The compressive and cyclic loads used for the different patient specific groups.

	Compressive load	**Cyclic load**
Group 1	2000 N	600 N
Group 2	2000 N	375 N
Group 3	1000 N	600 N
Group 4	1000 N	375 N
Group 5	900 N	350 N

For all the groups there is also a difference between cyclic loads and peak loads, which will both result in different failure mechanisms, given these groups different design limitations. The first step is to look at the production process. During the production process the mechanical properties of the implant will be obtained. By altering the production processes, such as 3D printing, heat treatment, sandblasting and etching, it is possible to achieve different printing qualities, surface finishes and microstructures.

All these material properties have a large effect on the fatigue life, yield strength and the osseointegration of the implant. Different printing qualities, like hardness, internal porosity and surface quality, can be obtained by changing the parameters of the printing process, for example laser power, scan speed, hatch space and scan angle or by choosing different printing processes such as SLM or EBM. The surface finish will depend on the printing process, but also on post processing like sandblasting and etching. The microstructure can be changed by applying a post heat treatment. Not only the production process will determine the mechanical properties of the spinal cage, but also the design has a huge role in this. By changing the relative amount of porous or solid material the strength and apparent Young's modulus of the implant can be changed. Furthermore, the location and shape of the solid and porous material influence the mechanical properties.

4.1.5. Methods of altering implant design to become patient specific

To create patient specific designs four main alterations can be made to the design. These are altering the outer dimensions; the amount and placement of solid material; the production process; and the porosity.

Changing the outer dimensions could create problems with the insertion, the placement and the stability of the implant. To avoid these problems the same outer dimensions compared to the existing PLIF implant are taken.

Increasing the amount of solid material compared to the amount of porous material can strengthen the spinal cage when placed correctly. It is also important to understand that at the solid-porous interface stress concentrations are created which will weaken the implant material. Apart from the solid-porous interface sharp corners or complex shapes can create stress concentrations. In this report a great amount of work went into finding the optimal solid-porous ratio and figure out the placement of the solid material. This resulted in a spinal cage design which is further described in Chapter 5.

By altering the production process different material properties can be achieved. This could be a good method for creating the desired spinal cage for a specific patient without altering the design. The production process itself can be divided into two parts, heat treatment and post processing. Different temperatures (below and above the β transus temperature), heating times and cooling rates can be applied. Changing one of these parameters will change the microstructure which will result in different mechanical properties. To use this for creating patient specific designs, an extensive understanding is required about how these changes will influence the mechanical properties, which is currently not available. For surface treatment sandblasting and etching are used. These processes mainly have the function to increase the fatigue life by removing defects at the surface, but by using them for an extended period of time it is possible to remove quite some material. The removal of this material will also affect other mechanical properties apart from fatigue life.

For now the most effective way to produce patient specific implants is by changing the porosity of the material. The spinal cages are mostly made of porous material and some parts of solid material. Changing the porosity of the porous material will change the apparent Young's modulus, Poisson's ratio and the yield strength. The apparent Young's modulus will decrease with increasing porosity. By lowering the apparent Young's modulus it becomes more similar to the Young's modulus of bone, improving osseointegration. This decrease in apparent Young's modulus will also decrease the yield strength of the spinal cage and due to the larger modulus mismatch between the solid and the porous higher stress concentration are created reducing the fatigue life. Finally, an optimum has to be found between the strength of the implant and the apparent Young's modulus. This optimum will be different for every patient group.

The method of designing and optimising different designs is done using simulations. This will be described in the next section.

4.2. Modelling using FEM

Several programs, such as Magics, SolidWorks and COMSOL, were used to design and test the samples. In order to create the design of the porous Ti6Al4V cylindrical samples with a diamond structure the program Magics was used. The diamond structure itself was already available in Magics, so only the outer dimensions were changed. This design was 3D printed to create the cylindrical samples. For the spinal cages SolidWorks was used to create a design and COMSOL was used to simulate mechanical tests on this design. Magics is again used to create the porous structure in the implants which can be 3D printed to create the samples.

4.2.1. Sample design

SolidWorks was used to create the new PLIF spinal cage. First, a sketch was made and using the extrude function and a solid block was created. Fillets were used to round the edges. When the base design was finished, the implant has to be split up in a solid and porous part. Using different sketches, extrude cuts and fillets the base design is altered to create the solid part. The solid part is cut out of the original base design using the cavity function, which leaves the porous part of the implant. Finally, when combining the solid and porous parts a spinal implant was created.

For the simulated tests in COMSOL two vertebrae were created in SolidWorks. Using the cavity function a small hole is made in both vertebrae in order to ensure a good fit during the simulations, as shown in Figure 4.8.

4.2.2. Set-up

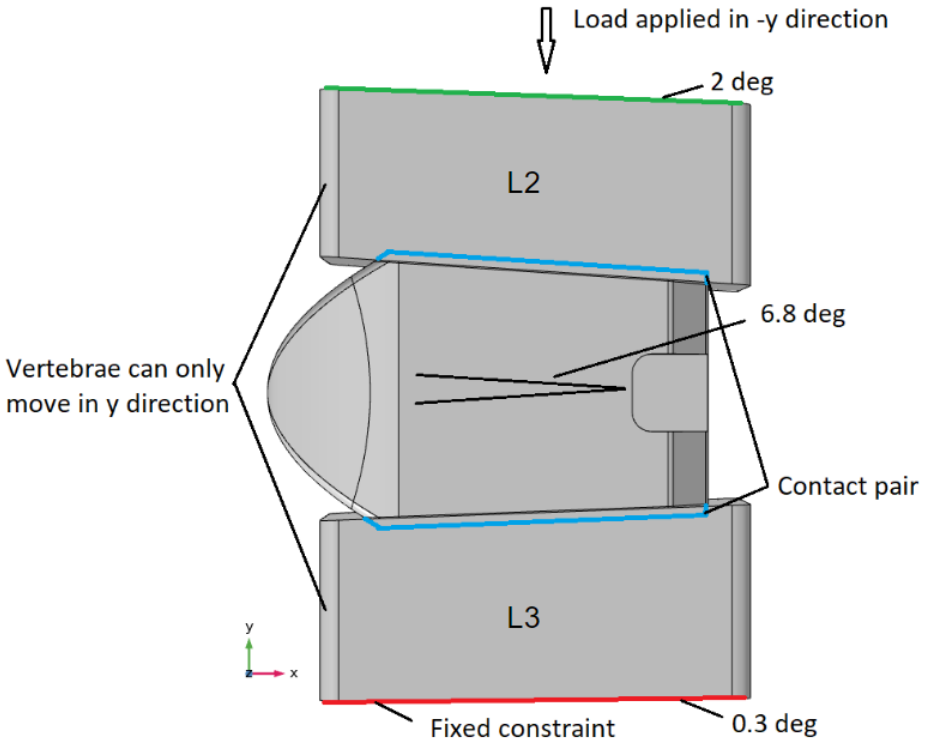

Figure 4.8: Set-up used for COMSOL simulations.

The simulation set-up is based on the same angles as found in real vertebrae, as shown in Figure 4.8 and 4.9. The spinal cage for these simulations is placed between the L2 and L3 vertebrae, which results in the following angels, L2: -2°, L3: 0.3° and between L2-L3: 6,8 °.

The setup consists of 7 different parts: 4 parts simulating solid Ti6Al4V; 1 part simulating porous Ti6Al4V; and 2 parts simulating the vertebrae.

The solid and the porous parts are fused together using the fusion method provided by COMSOL. This means that at the interface of the solid and porous material the material is fixed together and is not able to move relative to each other. The spinal cage is placed between two blocks, which simulate the vertebrae. The interface is defined as contact pair, which will insure that the materials will not move through each other when pressed together, whilst allowing the

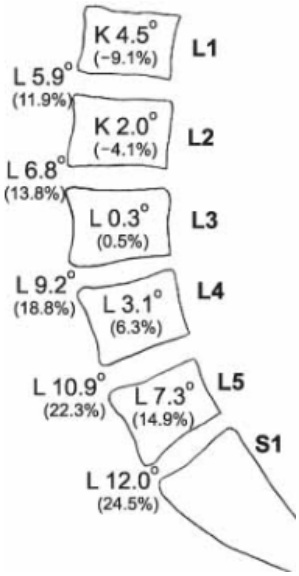

Figure 4.9: The standard of segmental shape in lumbar vertebrae [52].

material to move relative to each other at the interface.

An alternative option is to create a fusion between the surface of the spinal cage and the blocks simulating the vertebrae. In literature it is found that a connection is formed between the spinal cage and the vertebrae in the body in 1 or 2 weeks. The whole fusion process will take between 3 and 6 months after which the bone created between the vertebrae can support itself. It could be that a simulation using fusion between the spinal cage and the vertebrae gives results more closely resembling the spinal fusion process in the body. Unfortunately, it is not possible to perform mechanical tests with fused implants for my thesis and also for approval of this medical device only tests with a contact pair have to be performed. Therefore this technique of fused spinal cage and vertebrae is not further investigated.

A fixed constraint is applied at the bottom surface of the block simulating the L3 vertebra to ensure the set-up stays in place. Furthermore, a force is applied at the top surface of the top block simulating the L2 vertebra. The load is applied in the negative y-direction. Note that this is not perpendicular to the top surface of the top block. A parameter is created to run the simulation at the desired load and at 10% of the desired load. This will be useful later for fatigue simulations.

4.2.3. Mechanical properties

For the simulations three different materials are used: 3D printed solid Ti6Al4V, 3D printed porous Ti6Al4V and lumbar vertebra. For the lumbar vertebra Polyoxymethylene (POM) is used during the fatigue tests and will therefore also be used for the simulations. The three material properties which are important for the simulations are Poisson's ratio, Young's modulus and density. The values of these properties for solid 3D printed Ti6Al4V and POM are given in Table 4.5.

The mechanical properties of the porous 3D printed Ti6Al4V depend on the porosity of the material. The pores arise because of the 3D printed diamond structure. This means every node is connected to four other nodes and the angle between each strut is 109.51°. It is possible to predict the yield stress, apparent Young's modulus and Poisson's ratio of this structure using analytical methods. The following equation gives the relationship between the strut length (L), the size of a unit cell (a) and the angle between struts and the horizontal plane

Table 4.5: Mechanical properties of solid 3D printed Ti6Al4V and POM.

	solid 3D printed Ti6Al4V	**POM**
Young's modulus (GPa)	113.8	3
Poisson's ratio	0.342	0.44
Density (kg/m^3)	4430	1410

(θ):

$$a = 2\sqrt{2}Lcos(\theta). \tag{4.2}$$

Since θ = 35.26° for a diamond structure, as explained further in [3], the equation becomes:

$$a = \frac{4\sqrt{3}}{3}L. \tag{4.3}$$

Subsequently, the volume of the unit cell is given by:

$$V_1 = \frac{64\sqrt{3}}{9}L^3. \tag{4.4}$$

If the strut diameter is defined as (d), the total volume of struts in this unit cell is given by:

$$V_{struts} = 4\pi d^2 L. \tag{4.5}$$

The relative density is defined as the ratio of the density of the porous material compared to the density of the solid material, or as the ratio of the volume of the porous material to the volume of the solid material:

$$\rho = \frac{V_{struts}}{V_1} = \frac{3\pi\sqrt{3}d^2}{16L^2} \cong 1.02\frac{d^2}{L^2}. \tag{4.6}$$

The porous material has an isotropic structure which results in isotropic mechanical properties.

In order to create an equation for calculating the apparent Young's modulus two different theories are used: the Euler–Bernoulli and Timoshenko theories [97]. The aim is to relate the mechanical properties of the solid material to the mechanical properties of the the porous material and the relative density. Take F_{tot} as the force in the y-direction of a unit cell. Because the structure is isotropic the force on every strut is the same. There are four struts in every unit cell resulting in the force on one strut to be: $F_{strut} = F_{tot}/4$; and the bending moment to be: $M = \frac{1}{2}F_{strut}Lcos(\theta)$. The struts are deformed due to a combination of bending moment ($\delta_{22,b}$) and axial force ($\delta_{22,a}$), as shown in Figure 4.10.

The total deformation in the y-direction is given as the combination of bending moment and axial force:

$$\delta_{22} = \delta_{22,a} + \delta_{22,b} = \frac{FL^3cos^2\theta}{12E_sI} + \frac{FLsin^2\theta}{E_sA}, \tag{4.7}$$

where E_s is the Young's modulus of the matrix material, I is the moment of inertia and A is the cross-sectional area of the strut. This gives the deformation of one strut. In order to get the deformation in the y-direction of the whole unit cell the following equation is used:

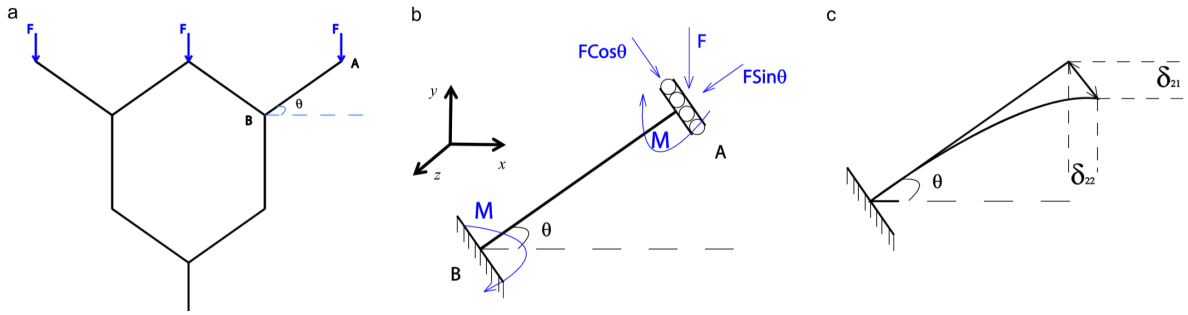

Figure 4.10: a) An arbitrary unit cell under uni-axial compression. The free body diagram and deformations of an arbitrary strut in the b) y- and c) x-directions [3].

$$\delta_{22,UC} = 4 * \delta_{22}. \tag{4.8}$$

Using the stress-strain relationship ($\sigma = E\epsilon$) the deformation of the unit cell is given by the following relationship:

$$\delta_{22,UC} = \frac{\sqrt{2}P}{4LE_u cos\theta}. \tag{4.9}$$

By combining equation 4.7 and 4.9 and by assuming the apparent Young's modulus of an infinitely large cellular structure is equal to the apparent Young's modulus of a single unit cell ($E_{US} = E_p$) the following relationship between the apparent Young's modulus of the cellular structure (E_p) and the Young's modulus of the matrix material is obtained (E_s):

$$E_p = \frac{\rho^2}{3.85 + 1.41\rho} E_s. \tag{4.10}$$

The Timoshenko beam theory also considers rotational inertia next to shear deformation. This results in an additional term added to equation 4.10 making the equation closer to experimental results:

$$E_{p-Timoshenko} = \frac{(0.46 + 0.17\rho)\rho^2}{(0.46 + 1.17\rho)(3.85 + 1.41\rho)} E_{solid}. \tag{4.11}$$

In order to find the relationship between the relative density and the Poisson's ratio, the Euler–Bernoulli beam theory is used again. However, this time the deformation relationship has to be expressed in the x-direction:

$$\delta_{21} = \delta_{21,a} + \delta_{21,b} = \frac{\sqrt{2}FL^3 sin2\theta}{48E_s I} + \frac{\sqrt{2}FLsin2\theta}{4E_s A}. \tag{4.12}$$

Subsequently, the Poisson's ratio can be calculated as follows:

$$v_{12} = -\frac{\delta_{21}}{\delta_{22}} = -\frac{\delta_{21}}{\delta_{22}} = \frac{4L^2 - 3d^2}{8L^2 + 3d^2}. \tag{4.13}$$

And using $\rho \cong 1.02d^2/L^2$ the Poisson's ratio can be expressed in terms of relative density:

$$v_{porous} = 0.5\frac{(1 - 0.735\rho)}{(1 + 0.368\rho)}. \tag{4.14}$$

For the COMSOL simulations of the porous structure, three material properties are needed, the apparent Young's modulus, the Poisson's ratio and the density, which are obtained by the

above equations. However, in order to understand when the material yields, the yield strength of the material has to be related to the relative density. Material failure can happen due to buckling or yielding. It was found by Ahmadi et al. (2014) that buckling is only more likely to occur in materials with a porosity above 99.96%, therefore only yielding is further considered.

To find a relationship between the yield strength and the relative density a few assumptions are made. First of all, the maximum stress is a combination between the bending moment and the axial force; the bending moment can be neglected when the material reaches the plastic zone; and the plateau stress is equal to the yield stress of the material. This results in the following relationship between the plateau stress of the porous material and the yield stress of the matrix material:

$$\frac{\sigma_{pl,porous}}{\sigma_{y,solid}} = \frac{9\pi d^3}{32\sqrt{6}L^3} \cong 0.35\rho^{1.5}. \tag{4.15}$$

Finally, using equations 4.11, 4.14 and 4.15 the apparent Young's modulus, the Poisson's ratio and the yield stress can be plotted with respect to the relative density. Normally, the mechanical properties of the porous material are not only dependent on the relative density, but also on the production process, heat treatment and post treatment. Fortunately, the samples used in this research have undergone very similar production processes compared to the samples used to validate the equations produced by Ahmadi et al. (2014). In order for the simulations to be more realistic, equation 4.15 and 4.11 are scaled to match the values found during mechanical testing of the porous samples. The values for yield strength and apparent Young's modulus found during the mechanical testing and using the equations are shown in Table 4.6.

Table 4.6: The apparent Young's modulus and yield strength obtained with mechanical testing versus equation 4.15 and 4.11.

	Test sample	**Equation**
Young's modulus (GPa)	2.48	2.49
yield strength (MPa)	84.0	80.8

Using this data, equation 4.15 is scaled with (84.0/80.8) and equation 4.11 with (2.48/2.49). This results in the following plots, where the yield stress, Poisson's ratio and the apparent Young's modulus are plotted against the relative density.

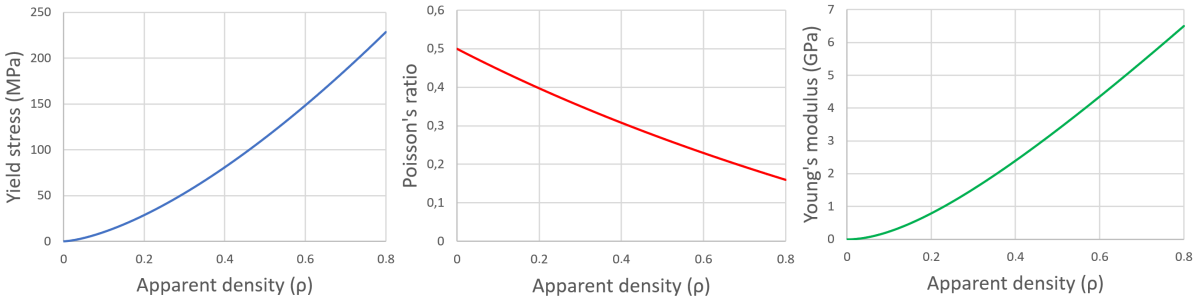

Figure 4.11: Yield stress, Poisson's ratio and apparent Young's modulus plotted with respect to the relative density of a porous material with a diamond shaped structure.

4.2.4. Sensitivity study

During simulations a mesh is created of the implant.The smaller the mesh size the preciser the measurement, however, this also increases the simulation time. During the mesh study the minimal mesh size and the maximum mesh size are decreased until the standard deviation of the measurements is not improving anymore and a visual inspection is performed for any abnormalities. For every measurement a new mesh is simulated to ensure every measurement is unique. For each mesh size 5 measurements are performed and the highest von Mises stress found is recorded as shown in Tables 4.7 and 4.8.

Table 4.7: Highest stress in MPa measured for a maximum mesh size of 3.12 mm and different minimum mesh sizes.

Maximum mesh size (mm)	Minimum mesh size (mm)	Highest stress (MPa)
3.12	0.561	3211
3.12	0.1	122.9 ± 4.5
3.12	0.01	122.7 ± 2.5
3.12	0.001	120.9 ± 6.2

Table 4.8: Highest stress in MPa measured for a minimum mesh size of 0.01 mm and different maximum mesh sizes.

Maximum mesh size (mm)	Minimum mesh size (mm)	Highest stress (MPa)
10	0.01	122.2 ± 2.1
3.12	0.01	122.7 ± 2.5
1	0.01	126.5 ± 3.7

For the simulations a maximum mesh size of 3.12 mm and a minimum mesh size of 0.01 mm are used. Using a maximum mesh size of 10 mm did not perform worse compared to a maximum mesh size of 3.12 mm, however, because no difference in computation time was noticed between the two meshes the smaller mesh size was chosen.

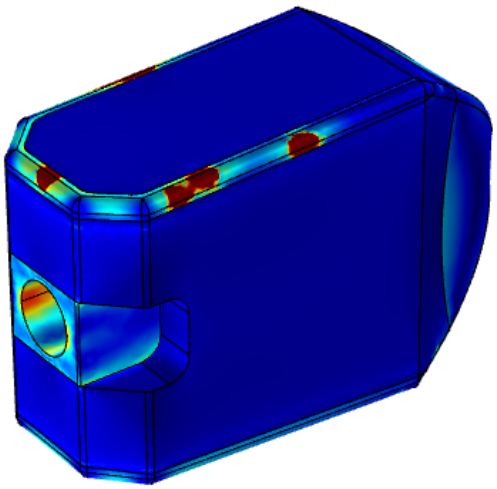

Figure 4.12: PLIF Spinal cage after a compression test using COMSOL.

During visual inspections a few abnormalities were found, which are shown in Figure 4.12. With a very robust mesh size the spinal cage is covered with red dots creating high stress concentrations in the material, which appear due to errors in the mesh. On a finer mesh size a dot can also randomly appear during a simulation. When this happens the simulation is repeated, because it makes it harder to find the actual location of the highest stress in the material.

4.2.5. Compression tests

In Section 4.2.2 the set-up used to perform the compression tests has already been explained. For every simulation two inputs have to be given: the applied load and the porosity of the porous material. Using equations 4.11, 4.14 and 4.15, the apparent Young's modulus, the Poisson's ratio and the yield stress, respectively, are calculated for the desired porosity. The goal of the simulated compression tests is to find the maximum porosity the material can have when a certain load is applied. Table 4.9 gives the compressive and cyclic loads which are used for the five patient specific groups.

Table 4.9: The compressive and cyclic loads used for the different patient specific groups.

	Compressive load	**Cyclic load**
Group 1	2000 N	600 N
Group 2	2000 N	375 N
Group 3	1000 N	600 N
Group 4	1000 N	375 N
Group 5	900 N	350 N

As shown in Table 4.9, three different compressive loads are used for the simulations. After each simulation the maximum von Mises stress is measured in the solid and porous part of the material. This is measured in both parts, because the solid and porous parts have a different apparent Young's modulus and yield stress. The yield stress of the solid part is 790 MPa and the yield strength of the porous part is dependent on the porosity. Figure 4.13 shows how the maximum von Mises stress is found after the simulation.

The three loads are plotted for different relative densities to obtain at what relative density the maximum von Mises stress exceeds the yield strength of the solid or the porous material in order to find the maximum porosity.

Figure 4.14 displays two example plots, which show the maximum stress for different relative densities when a load of 2000 N is applied. Similar graphs are made for 1000 N and 900 N. In this example the relative density of the porous material must at least be 0,16 for the maximum von Mises stress to be below the yield stress of the solid material and at least 0,45 for the maximum von Mises stress to be below the yield stress of the porous material. Since the porous material is the limiting factor, the relative density should therefore at least be 0.45. This means the porosity of the material should not exceed 55%.

When the maximum porosities for all the patient groups are found the compression tests can again be used to calculate the apparent Young's modulus for these maximum porosities. To calculate the apparent Young's modulus several compression simulations are performed using the maximum porosity and a load where the von Mises stress will not exceed the yield stress. A point is taken at the top surface of the implant and at the same location at the bottom surface. First of all the original distance between these points is measured and after the simulation the displacement of each point can be measured. Using this displacement the new

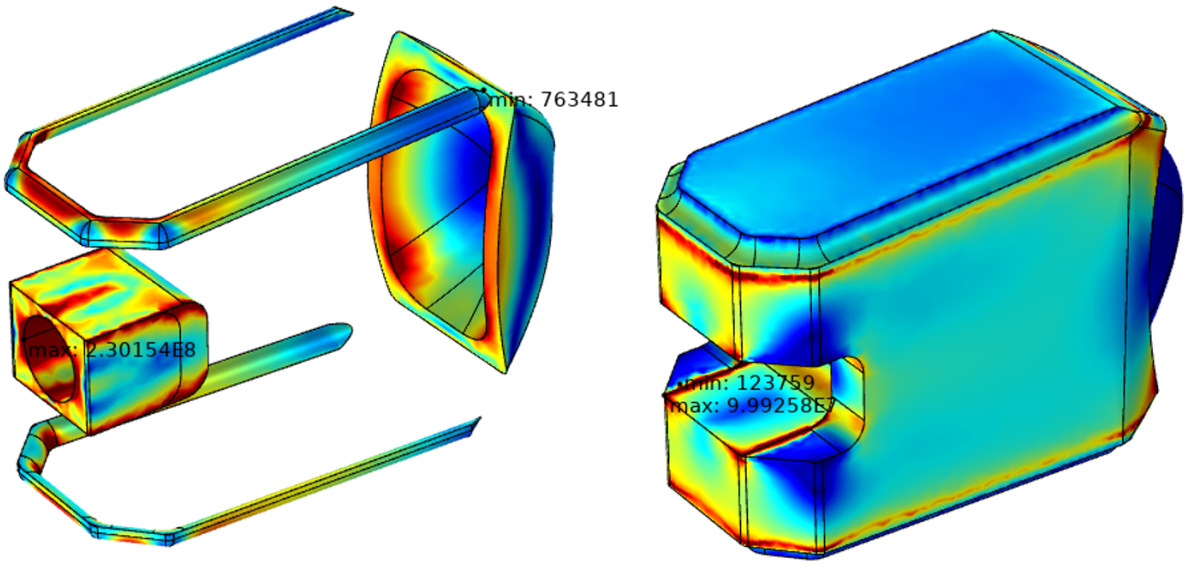

Figure 4.13: Spinal cage after a compression test using COMSOL. The minimum and maximum von Mises stress found are indicated at the solid parts (left) and the porous part (right).

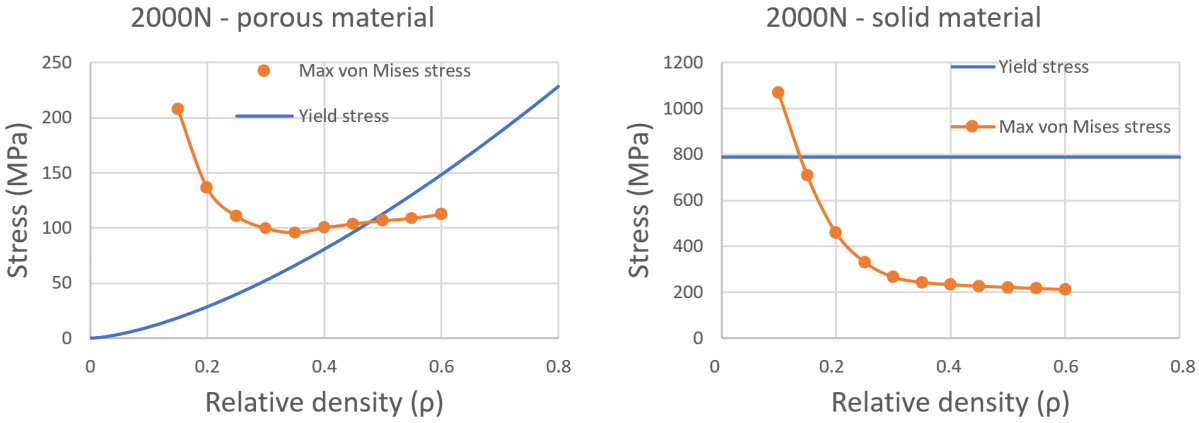

Figure 4.14: Maximum von Mises stress found in the spinal cage after a simulation for different relative densities.

distance between the points can be found and the amount of strain can be calculated. Using the strain, the load and the surface area of the implant finally the apparent Young's modulus can be calculated. This process is repeated nine more times at other points on the implant to get an accurate average.

4.2.6. Fatigue tests

For the fatigue test additional information is required by the program, which is an estimation of the fatigue graph. There are two different materials present in the spinal cage (the solid and the porous part) with both different fatigue graphs. The fatigue graph of the porous material is chosen for this purpose due to two reasons. First of all, the von Mises stress in the porous material is closer to its yield strength compared to the solid material. This will usually result in a lower fatigue life and looking at fatigue tests of the original implant the lower fatigue life of the porous material is confirmed. During this project a plot of the fatigue life of as-processed (AP) porous samples is produced. The fatigue graph seen in Figure 4.15 is used to fit the fatigue graph found for the as-processed porous samples.

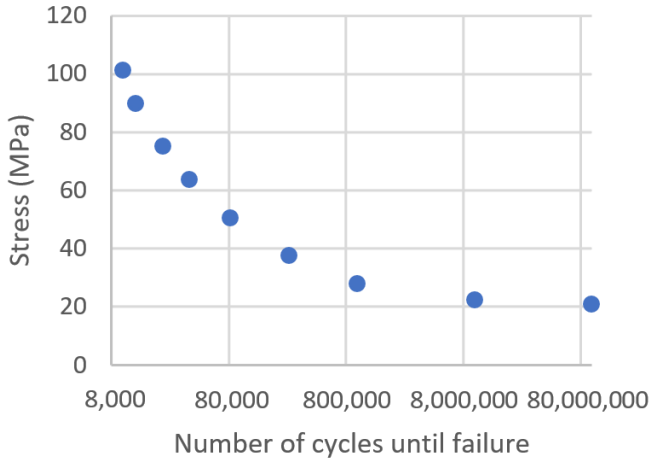

Stress (MPa)	Number of cycles
101.2	8586
89.6	13530
75.1	19866
63.6	44635
50.6	79689
37.6	263382
28.0	1.00E+06
22.4	1.00E+07
20.9	1.00E+08

Figure 4.15: Fatigue graph used to perform fatigue simulations in COMSOL.

The main reason to not use the fatigue graph of the whole implant are the presence of stress concentrations. For example, when a load of 2000 N is applied on the spinal cage, much higher stresses can arise in some parts of the implant due to stress concentrations created by the solid porous interface. When using the fatigue life of the implant it looks like the material failed due to a force of 2000 N when it actually failed due to the increased load created by the stress concentrations. To simulate this a fatigue graph is used of the porous material which is created by testing a uniformly porous sample to ensure the stress in this sample is the same everywhere. For the simulation first a compression test is performed to find the von Mises stress in every part of the implant caused by the applied load. Finally, these stresses can be used in combination with the fatigue graph to simulate the fatigue life of the implant.

As shown in Table 4.9 the fatigue life for three different loads should be tested. For these tests an R-ratio of 0.1 is used and a maximum number of cycles of 100 million. This is because the inserted fatigue graph only provides information about the fatigue life until 100 million cycles. The loads are tested in combination with different porosities to find the maximum porosity where the fatigue life is at least 5 million cycles for a certain load. In Figure 4.16 an example is given of how this maximum porosity can be found.

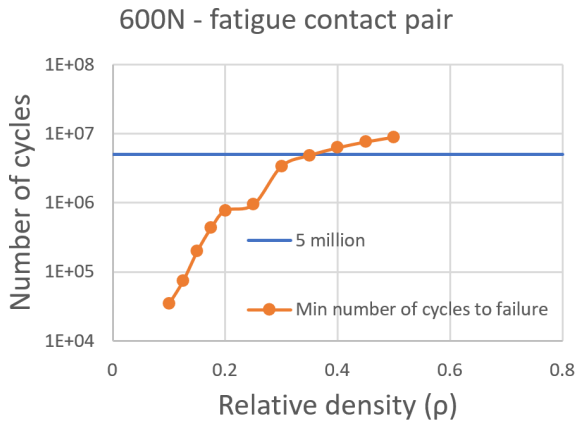

Figure 4.16: Example of minimal number of cycles to failure compared to the relative density.

Apart from finding the fatigue life using simulations, it is also interesting to gather informa-

tion about the location of fatigue initiation and how this progresses through the material.

Finally, compression tests and fatigue tests can be used to find the apparent Young's modulus for a patient specific group. When a group has a maximum compression load of 2000 N and a cyclic load of 600 N as the examples given in Figures 4.14 and 4.16, the maximum relative densities are 0.16 (solid material), 0.45 (porous material) and 0.38 (fatigue life). This results in porosity ranges of 0 - 84% (solid material), 0 - 55% (porous material) and 0 - 62% (fatigue life). This means that for this example the porous material is the limiting factor and the maximum porosity for this group is 55%. Using this porosity the apparent Young's modulus can be calculated.

4.3. Experimental methods

In this section the experimental methods are described, which consists of mechanical tests (compression and fatigue testing), X-ray diffraction and microstructural characterisation, but first the test samples and how they are manufactured and post processed are discussed.

4.3.1. The test samples

Two different samples are mechanically tested in this report: a porous 3D printed cylindrical sample made from Ti6Al4V with a diamond structure and a 3D printed PLIF spinal cage made from Ti6Al4V with a partly porous diamond structure and a partly solid structure. These two types of samples are shown in Figure 4.17.

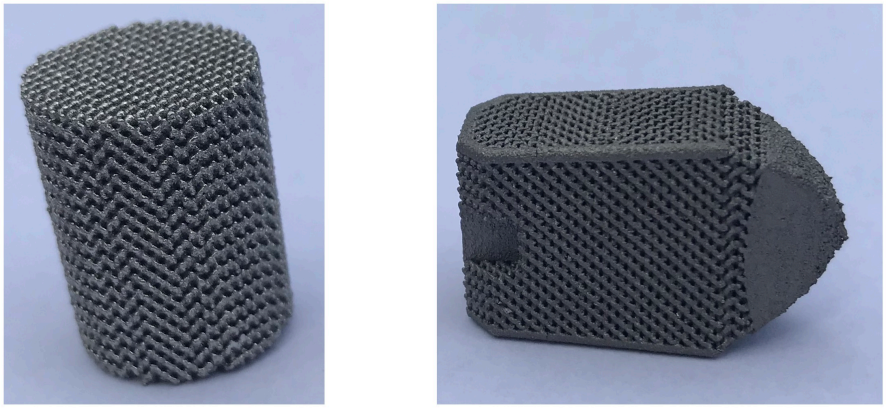

Figure 4.17: 3D printed samples used for mechanical testing. Cylindrical sample (left) and spinal cage (right).

Powder characteristics

For the 3D printing process an ELI (extra low interstitials) grade 5 Ti6Al4V powder with spherical particles was used. The particle size is 20 - 63 µm and is produced by AP&C (Advanced Powders and Coatings Inc). Grade 5 Ti6Al4V refers to a composition of almost 90% titanium, 5.5 - 6.5% aluminium, 3.5 - 4.5% vanadium, a maximum of 0.25% iron, a maximum of 0.13% oxygen, a maximum of 0.05% nitrogen, a maximum of 0.015% hydrogen and a maximum of 0.008% carbon.

Manufacturing

The continuous laser based samples were manufactured with Ti6Al4V ELI powder with a particle size of 20-63 µm (grade 5) from SLM Solution Group AG, Lubeck, Germany. The SLM machine is equipped with Twin (2x 400 W) IPG fiber lasers (IPG Photonics Corporation, Ox-

ford, USA) with a wavelength range of 1070±10 nm. The samples were manufactured using a layer thickness of 30 µm and scan speed of 10 m/s.

Cell type

The porous material has a diamond structure as shown in Figure 4.18.

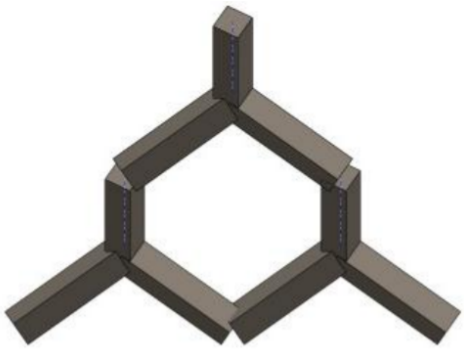

Figure 4.18: Schematic drawings of diamond unit cell [2].

Porosity

In order to determine the porosity of the samples dry weighting was used. The porosity can be calculating by obtaining the outer dimensions of the sample and measuring the weight to calculate the the density of the sample using the following equation:

$$\left(1 - \frac{\rho_{sample}}{\rho_{3D-Ti6Al4V}}\right) * 100 = porosity. \tag{4.16}$$

Since the material is 3D printed internal defects can be created due to the presence of contamination's in the solid material and this also creates a level of porosity in the solid material. This internal porosity has to be taken into account when finding $\rho_{3D-Ti6Al4V}$. How the internal porosity is measured is explained in Section 4.3.4. Using the internal porosity the density of the solid 3D printed material ($\rho_{3D-Ti6Al4V}$) can be calculated using the density of Ti6Al4V.

To determine the porosity of a 3D printed spinal cage, which includes porous and solid material, the ratio between the solid and the porous material has to be found. This can be found using the software which is used to design the implant. In this case the software used is SolidWorks and 90.88% of the implant is porous material and 9.12% solid material. The following equation is used to calculate the porosity of the 3D printed spinal cage in combination with Equation 4.16:

$$\rho_{sample} = \frac{m - 0.0912 * V * \rho_{3D-Ti6Al4V}}{0.9088 * V}. \tag{4.17}$$

In Equation 4.17 the mass (m) from the porous part is found by subtracting the mass of the solid part from the total mass. After this the mass is divided by the volume (V) of the porous part to find the density of the porous part.

When producing different samples the porosity will not always be the same. The strut length (L) and the angle between the struts are assumed to remain the same for all porosities, printing processes and post treatments. Now the only variable is the strut diameter (d) which determines the porosity of the samples.

To eliminate the effect of strut diameter and being able to compare different porosities the compression and fatigue tests are normalised. Firstly, a benchmark porosity must be chosen

to normalise against. In this case a porosity of 65% is chosen, which translates to a relative density of $\rho_{relative}$ of 35%. Equation 4.18 created by Gibson et al. [31] can be used to find the strut thickness related to this porosity. This equation takes into account the overlap of material at the connections between the struts. In this equation two constants are used which depend on the structure of the material. In this case a diamond structure is used and the constants are: $C1$ = 4.08 and $C2$ = 3.21 [101][122].

$$\rho_{relative} = C_1\left(\frac{r}{L}\right)^2 - C_2\left(\frac{r}{L}\right)^3 \tag{4.18}$$

In order to relate the strut diameter to the applied stress, the force at one strut needs to be found. This can be done by dividing the total force over the amount of nodes (n) in the cross section using the following equation:

$$F_{strut} = \frac{F_{tot}}{n * 2}. \tag{4.19}$$

With a diamond structure a node at the top of the sample connects 2 struts, as can be seen in Figure 4.19. Thus the number of nodes is multiplied by 2. The number of nodes (n) in the top cross section of the sample can be calculated using the following equation where D is the diameter of the sample and a is the cell size:

$$n \approx \left(\frac{\pi}{4}\right) * \left(\left(\frac{D}{a\sqrt{2}} - 1\right) * 2 + 1 * 3\right)^2. \tag{4.20}$$

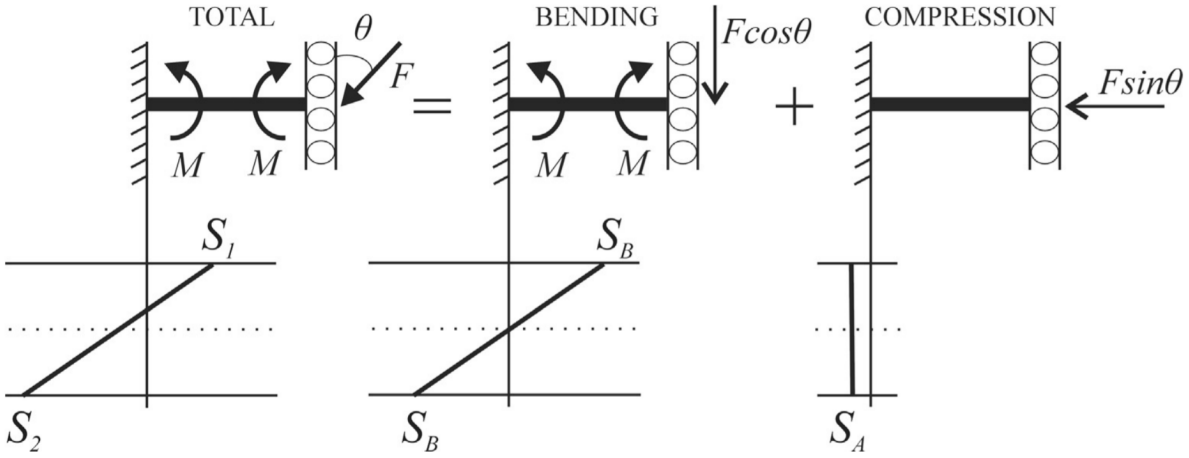

Figure 4.19: Approximation of normal stresses in a hyper-static strut of a diamond unit cell [101].

Figure 4.19 shows that the local stress σ_1 is created by combining the bending moment applied by the vertical element $F_{strut} * cos(\theta)$ and compression of the horizontal element $F_strut * sin(\theta)$. This σ_1 is the main reason for failure during compression and compression fatigue. σ_1 can be calculated using the following equations:

$$\sigma_A = \frac{F_{strut} * sin(\theta)}{A}, where A = \frac{\pi d^2}{4}, \tag{4.21}$$

$$\sigma_B = \frac{F_{strut} * L * d * cos(\theta)}{4 * I}, where I = \frac{\pi d^4}{64}, \tag{4.22}$$

$$\sigma_1 = \sigma_B - \sigma_A = F_{strut} * C_{sample}. \tag{4.23}$$

The parameter C_{sample} in equation 4.23 is used to account for the difference in structure and porosity of the sample. C_{sample} can now be calculated for the actual sample and using equation 4.16 and 4.23, $C_{65\%}$ can be calculated for the theoretical reference sample with 65% porosity. Moreover, C_{sample} is used to calculate σ_1 and using σ_1 and $C_{65\%}$ the hypothetical F_{strut} can be calculated for a porosity of 65%. Finally this hypothetical F_{strut} can now be used to find the normalised stress for the tested samples. This model assumes there are no differences in geometry, printing process and post treatment between the samples.

Post treatment

All spinal cages and some cylindrical samples did not have any post treatment and are referred to as as-processed (AP). In total 45 cylindrical samples are produced and 30 of these samples are post processed using a heat treatment. For the heat treatment a vacuum oven is used. The samples are heated in a quartz tube and immersed in titanium powder as *getter*. The heating rate is 10 °C/s and when the desired temperature is reached, the temperature is kept at this level for two hours after which the material is cooled to room temperature with a cooling rate of 10 °C/s. The temperatures the samples are heated to are 850 °C/s and 1050 °C/s, which are below and above the β transus temperature. From the 30 heat treated samples, 15 samples are heated to 850 °C/s and 15 samples are heated to 1050 °C/s.

4.3.2. Mechanical tests

For the mechanical test 45 3D printed cylindrical samples made from Ti6Al4V and 20 3D printed spinal cages made from Ti6Al4V were used. These samples have been subjected to quasi-static compression tests, fatigue tests, XRD and microscopy, as summarised in Table 4.10 and 4.11. All tests were destructive to the sample except for XRD.

Table 4.10: Number of cylindrical samples tested.

	Total	Compression	Fatigue	XRD	Digital Microscope
AP	15	3	9	1	1
V850	15	3	9	1	1
V1050	15	3	9	1	1

Table 4.11: Number of PLIF spinal cages tested.

	Total	Compression	Fatigue	XRD	Digital Microscope
AP	20	6	12	1	1

The cylindrical samples are designed to have a height of 20 mm and a diameter of 15 mm. As shown in Figure 4.20 the spinal cages are designed to have a length of 23 mm, a maximum height of 15 mm and a width of 9 mm. The top and bottom surface both create a 3° angle with respect to the horizontal.

Compression tests *Cylindrical samples*

The compression tests are performed on a Zwick z100 tensile tester according to the test method suggested in ISO 13314:2011(E). The cross-head speed used is 1.8 mm/min and three different end-of-test criteria were used: 0.6 strain, 50kN or a sudden drop in load of 30%. Between the sample and the machine two slabs are placed to protect the machine from damage. Before the samples were tested the stiffness of the machine was tested. This

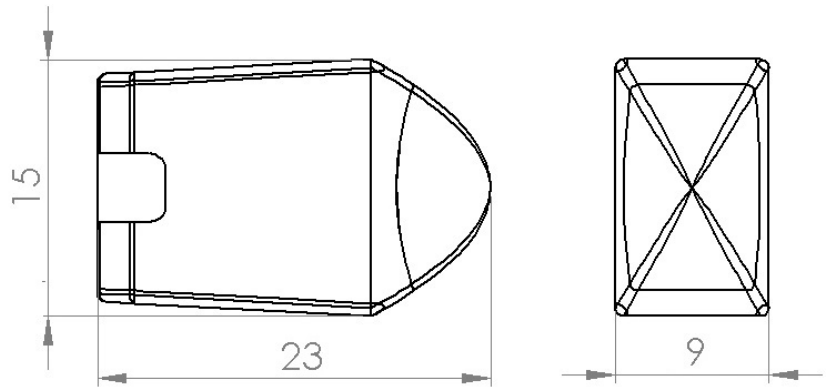

Figure 4.20: Dimensions of the spinal cage.

was done by doing a compression test without the sample, but with the two slabs. After this compression tests with the cylindrical samples were conducted.

The compression tests resulted in several stress-strain graphs. From these graphs the apparent Young's modulus is calculated by taking the stiffness (k_{setup}) of the set-up and the stiffness of the set-up including the sample ($k_{setup+sample}$). The following equation is used to find the stiffness of the cylindrical sample:

$$k_{sample} = \frac{1}{\frac{1}{k_{setup}} + \frac{1}{k_{setup+sample}}}. \tag{4.24}$$

Using the stiffness of the sample, the surface area and the strain, the apparent Young's modulus can be calculated. Another value which can be found using the stress-strain graph is the yield strength of the material. According to ISO 13314:2011(E) the yield strength of porous and cellular metals with a porosity above 50% can be found by plotting a 0.2% offset strain as shown in Figure 4.21.

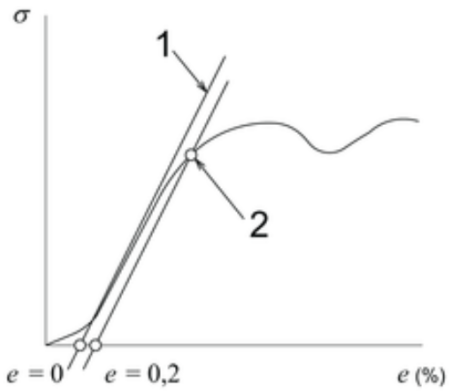

Figure 4.21: Yield stress measurement advised for compression tests of porous samples with a porosity above 50%.

This line is plotted by creating a line which overlaps the elastic part of the stress-strain curve and shifting this 0.2% on the x-axis where the strain is plotted. The intersection of the offset line with the stress-strain curve gives the yield strength of the sample.

Compression tests *Spinal cage*

For the compression tests of the spinal cage the Zwick/Roell BZ1-EXZW001 is used. The top and bottom surfaces of the spinal cage are not parallel to each other, but under an angle of 6°.

This means the set-up has to be altered in order to perform compression tests. ASTM F2077 - 18 advises to use the following set-up as shown in Figure 4.22.

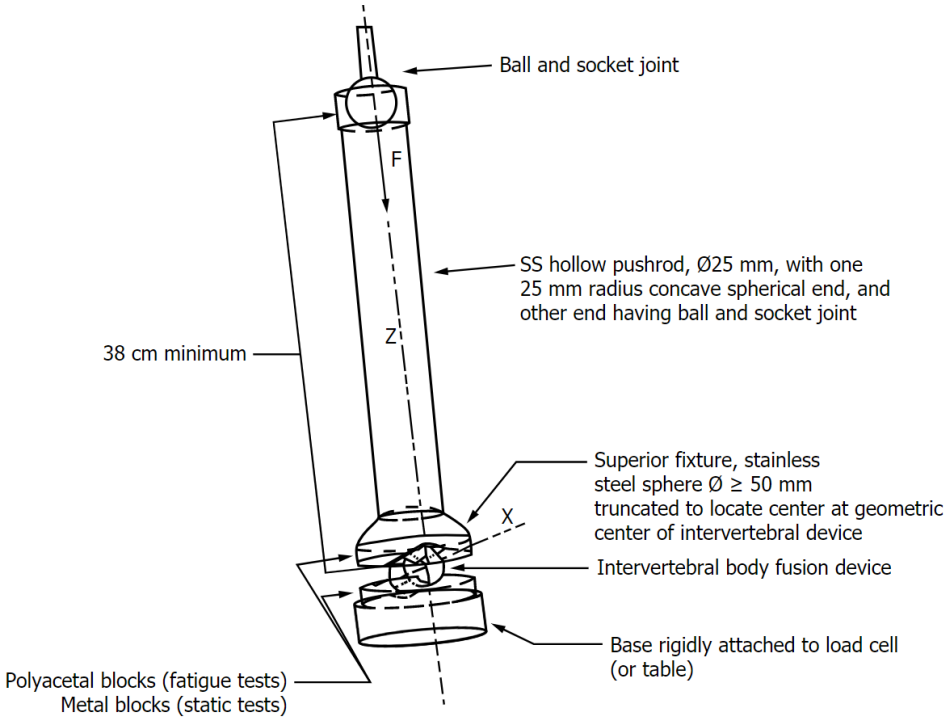

Figure 4.22: Recommended set-up by ASTM F2077 - 18.

The parts required to build this set-up are shown in Figure 4.23 and were already manufactured in a previous project performed at the TU Delft. The push-rod shown in Figure 4.23a and the minimal friction sphere shown in Figure 4.23b are manufactured using lathe. The ball and socket join in Figure 4.23c was a standard part and finally the steel plates in Figure 4.23d are produced using CNC milling. After production a post heat treatment was applied to the steel plates, the push-rod and the minimal friction sphere in order to achieve a UTS of at least 1310 MPa. The groves in the steel plates are made to match the outer dimensions of the spinal cage in order to aim the applied force at the geometrical center of the implant.

Using this system the top steel plate is able to rotate around two axes causing the push-rod to move out of centre. This can cause a momentum on the load cell of the machine, which can influence the results or even break the load cell. To counter this problem a long push-rod is used to reduce the momentum on the load cell. Assuming there will be a maximum sideways displacement of 5 mm and a maximum force of 20 kN, a horizontal force of 297 N will be applied on the load cell. This force results in a momentum of 29.7 Nm, which was found to be insignificant.

In Figure 4.24 the set-up is assembled and to get an accurate measurement and extensometer is added to the set-up.

During the compression test the end-of-test criteria are 20 kN, 4 mm displacement and a drop of 15% of the applied force. The test is displacement controlled with a speed of 1.8 mm/min. Five measurements were performed to determine the stiffness of the set-up without the samples after which six spinal cages were tested. Using Equation 4.24 the stiffness of the sample is calculated, which is used to find the apparent Young's modulus.

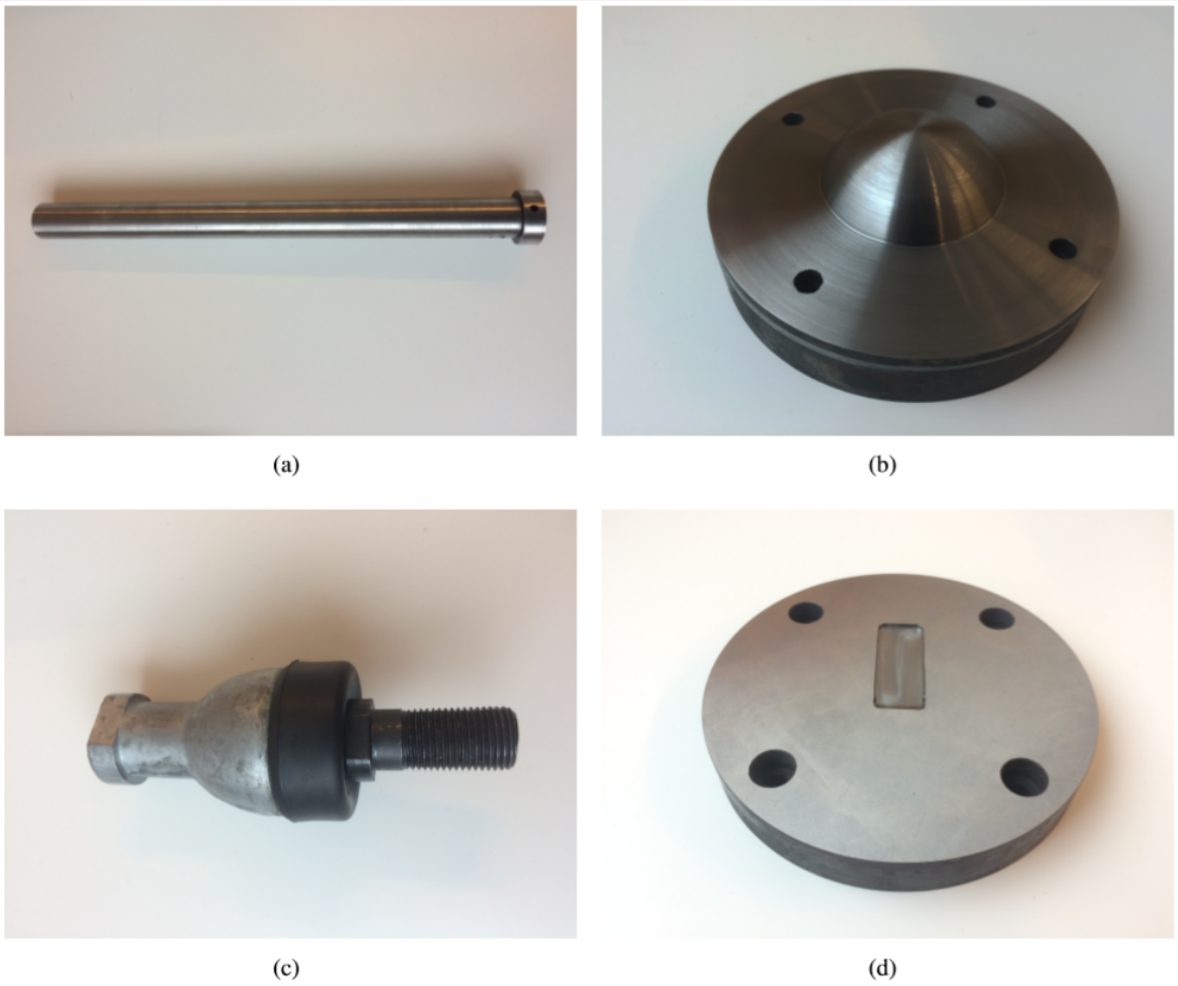

Figure 4.23: A set of four parts of the ASTM F2077 set-up: (a) Push-rod; (b) minimal friction sphere; (c) ball and socket joint; and (d) steel block [49].

Fatigue tests *Cylindrical samples*

For the fatigue tests on the cylindrical samples the MTS 858 was used with a 100 kN load cell. An R-ratio of 0.1 was used and a frequency of 15 Hz. The load applied during the fatigue tests is based on the yield strength of the samples. Three different sample groups were tested, which are as-processed, heat treated at 850 °C and heat treated at 1050 °C. For every group three samples were tested at 75%, 50% and 35% of the yield strength. The end-of-test criteria are 4 mm displacement, 5 million cycles and a drop of 30% of the applied stress. The P-gain was 3,286 and the I-gain was 4,000. In Figure 4.25 the set-up is shown.

Fatigue tests *Spinal cage*

For the fatigue tests of the spinal cages the 60 kN Home made (LF7M01) machine is used. An R-ratio of 0.1 is used and a frequency of 10 Hz. In ASTM-F2077 10 Hz is advised as the maximum frequency to prevent excessive heating of the POM blocks. Five different loads are used to create a fatigue graph. For three loads three samples were tested, for one load two samples were tested and for the last load only one sample is tested. The end-of-test criteria are 2.5 mm displacement, 5 million cycles and a drop of 30% of the applied stress. To find the fatigue life of the spinal cages the displacement is plotted against the number of cycles as shown in Figure 4.26. In this graph the point where the curve suddenly drops is taken as the fatigue life of that sample.

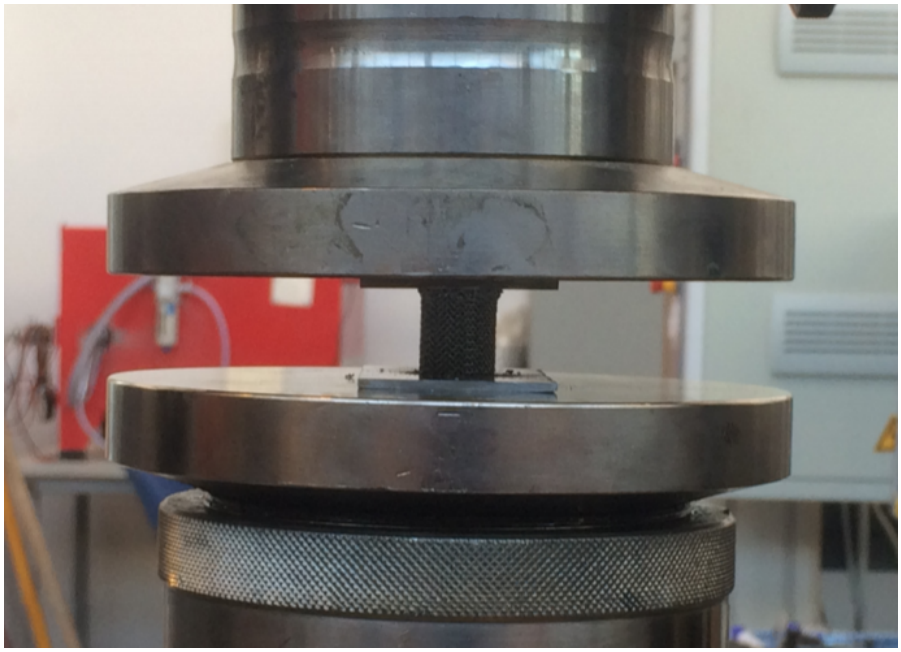

Figure 4.24: The set-up for compression tests.

Figure 4.25: The set-up for fatigue tests.

To visualise the fatigue failure of the spinal cage a time lapse is made where a picture is made every 300 seconds using a camera. The set-up which is used for the fatigue tests on the spinal cage is shown in Figure 4.27.

4.3.3. X-ray diffraction

X-ray diffraction (XRD) measurements are performed to find the different phases in the material. It could also be used to measure possible corrosion on the surface of the sample. The sample was put in a holder LH20 as can be seen in Figure 4.28.

The ‘lines’ at the top were aligned parallel with the incident beam to maximize the irra-

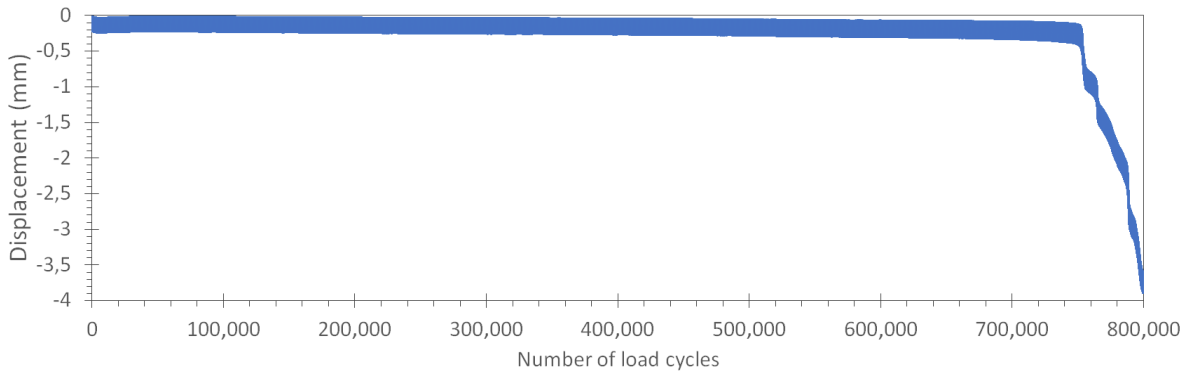

Figure 4.26: Cross-head displacement during a fatigue test on a spinal cage.

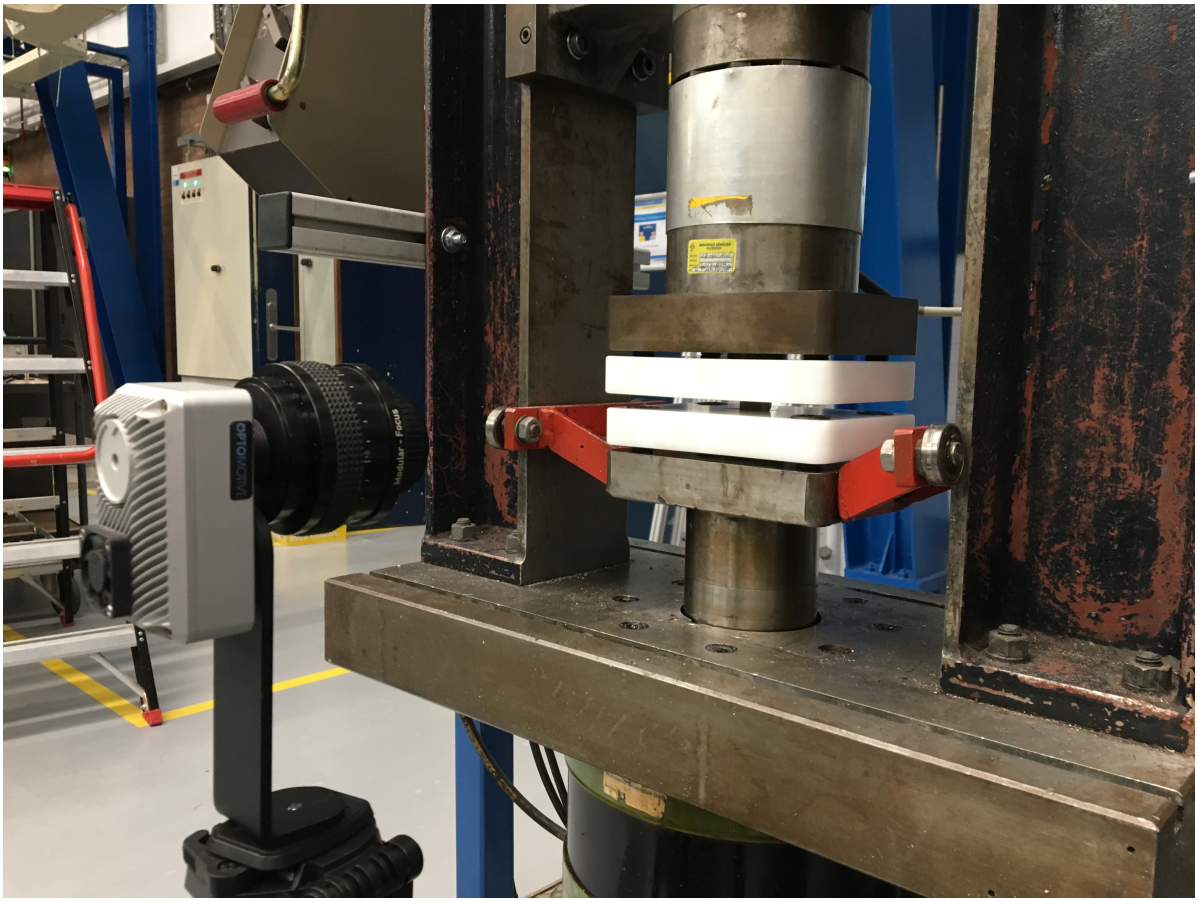

Figure 4.27: Set-up for the spinal cage fatigue tests.

diated area and no sample spinning is applied. The Bruker D8 Advance diffractometer with Bragg-Brentano geometry and Lynxeye position sensitive detector were used to do the experiment. The set-up was operated with Cu Kα radiation (45 kV, 40 mA) and diffracted beam with a Ni filter. Divergence slit V12 was used and a scatter screen height of 5 mm. The measurement method used is coupled TwoTheta/Theta scan, step size 0.03°, 2θ, counting time per step 2 seconds and detector settings LL 0,11 W 0.14. Finally, the software used for the data evaluation is Bruker software DiffracSuite.EVA vs 5.0.

Figure 4.28: Sample with holder used for XRD measurements.

4.3.4. Microstructural characterisation

Before being able to obtain microscopic images, the samples need to be prepared. The samples are cut perpendicular to the top surface using the Struers secotom 10. After cutting the samples are embedded in bakelite using a mounting press. The samples are sanded in steps where every step the grain-size of the sanding paper is reduced. To ensure a mirror like finish without visible scratches the samples are polished in two steps with grain sizes of 3 µm and 1 µm. Finally, to make the microstructure visible the samples are etched. The etchant consists of 50 ml H_20 25 ml NHO_3 and 5 ml HF. Now the samples are swabbed with the etchant until the microstructure is clearly visible. Finally, the Keyence VHX5000 microscope was used to create microscopic pictures.

Strut thickness

The same samples which were prepared for the microscopic pictures are used to measure the strut thickness. In Figure 4.29a the diamond structure of the porous material is shown. As explained the samples are cut perpendicular to the top surface and a cut will be made as shown in Figure 4.29b. The resulting surface area of the cut can now be seen in Figure 4.29c where the red line shows how the strut thickness is measured. This measurement is repeated for 30 different struts for every sample.

Internal porosity

To find the internal porosity, the samples which were used to gather microscopic pictures and measure the strut thickness are sanded and polished again to recreate a mirror like finish. Now using the Keyence VHX5000 microscope, the internal pores are clearly visible as seen in Figure 4.30. The background is made white and using the program paint.net the percentage of the material which consists of pores is estimated. For every sample where the internal porosity is measured this is done at 10 locations to get an accurate average.

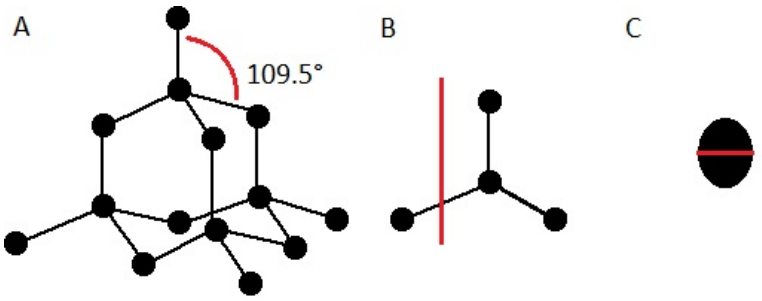

Figure 4.29: a) Shows the diamond structure used in the cylindrical samples where all angles between struts are 109.5 degrees. b) A side view of a single unit cell and the red line represents the cut that is made to determine the strut thickness. c) Shows the expected oval shape of the intersection of the strut and the red line shows how the diameter is estimated of a strut.

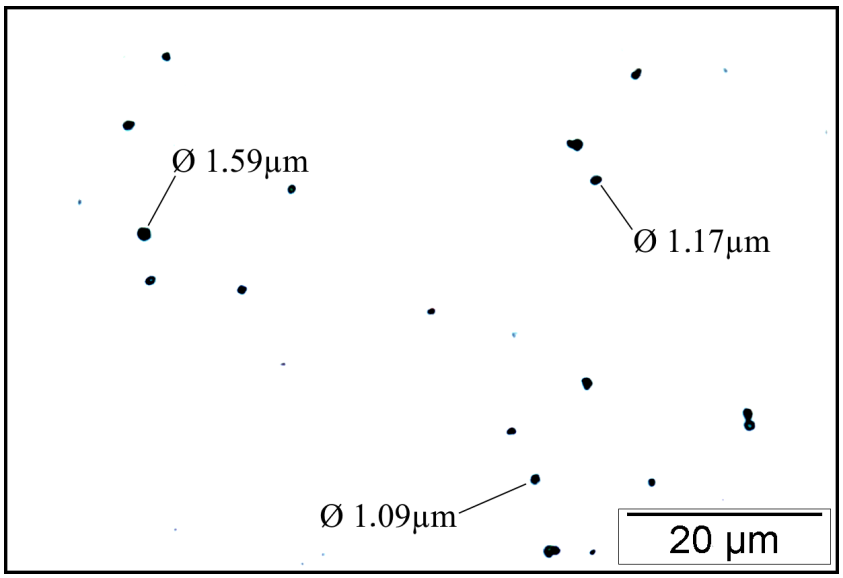

Figure 4.30: Microscopic picture of as-processed sample which is sanded and polished.

4.3.5. Statistical analysis

To investigate whether a significant difference is found between data points, statistical analysis is performed. This involves determining the probability a certain value is found, when assuming the value is expected to be the same as the average. If the probability is found to be too small, it can be concluded that the values are not the same and a significant difference is found. In this case the choice is made that a probability below 5% is considered a significant difference. For a single value a significant difference can be achieved when it is at least 1.96 times the standard deviation separated from the mean. However, it this report a lot of average values are compared to each other. To estimate the probability that a mean value will deviate a certain amount from the expected mean value a Z-score must be calculated. When the Z-score found is equal or above 1.96 the probability of finding this average is below 5%. This will result in concluding there is a significant difference between the averages. The following formula is used to calculate the Z-score. Where $\overline{X}$ is the measured average, μ is the expected average, SD is the standard deviation and n is the number of samples tested:

$$Z = \frac{\overline{X} - \mu}{SD/\sqrt{n}}. \tag{4.25}$$

The Z-score can be used to find the p-value. The p-value gives the probability a value will

deviate a certain amount from the average, where a certain amount is defined as the difference between the measured and expected value. For a Z-score of 1.96 the p-value is 0.05 which translates to a 5% probability a value will deviate a certain amount or more from the average. The p-value corresponding to a certain Z-value can be found in a standardised table.

5

Results and discussion

5.1. 3D printed porous cylindrical samples: experimental testing

In this section the results and discussion of the experiments on the 3D printed porous cylindrical samples are discussed. First the microstructural and morphological characteristics are examined, which include strut thickness measurements, analysing the microstructure. the internal porosity of the struts and the XRD measurements. This is followed by the results and discussion of the quasi-static compression tests and finally, the fatigue results are presented and discussed.

5.1.1. Microstructural and morphological characteristics

Strut thickness

Three different samples are used to calculate the strut thickness of as-processed, heat treated at 850 °C and heat treated at 1050 °C samples. No surface treatment like sandblasting or etching is applied on the samples. In Figure 5.1 the average strut thickness is shown. The average strut thickness for as-processed, 850 °C and 1050 °C is 303 $\pm$ 15 µm, 318 $\pm$ 21 µm and 304 $\pm$ 21 µm, respectively.

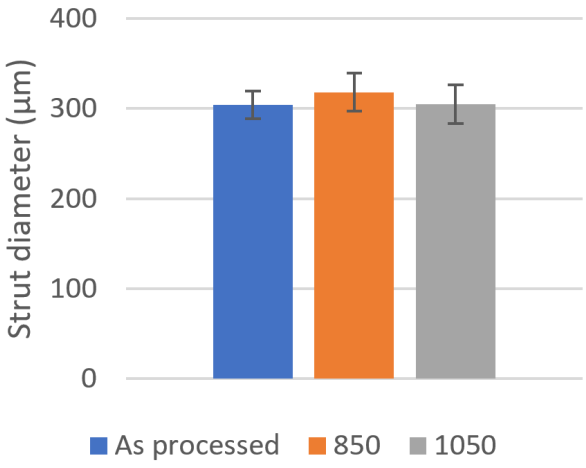

Figure 5.1: Average strut size for three different heat treatments including the standard deviation.

When looking at the standard deviation it can be seen the average strut thickness of each sample lies between the range provided by the standard deviation of the other samples. Using this information it seems there is no significant difference in strut thickness and the strut thick-

ness is not affected by the vacuum heat treatment. However, when calculating the Z-score the following values are found shown in Table 5.1.

Table 5.1: Z-score and p-value of the measured strut thickness for AP, V850 and V1050 samples.

	Z-score	p-value
AP	1.72	0.085
V850	2.29	0.022
V1050	1.55	0.121

No significant difference is expected since the applied temperature is not near the melting temperature. Thus without an externally applied force no deformation of the struts will take place. But to be determined not significant the Z-scores should be below 1.96 and as shown in Table 5.1 the Z-score for V850 is above this value. Looking at the p-value there is a 2.2% chance this would happen. No explanation can be given why there would be a significant difference, so it is expected this Z-score is found due to bad luck and/or bad measuring consistency.

Microstructure

Figure 5.2a shows the microstructure of the as-processed samples. The microstructure is mostly white which represents the α or $'\alpha$-martensite phase, but in this case it excepted to be mostly $'\alpha$-martensite. After the vacuum heat treatment at 850 °C for 2 hours it can be seen in Figure 5.2b that the $'\alpha$-martensite is transformed to an α (white) + β (black) structure. After the vacuum heat treatment at 1050 °C for 2 hours it can be seen that the α and β grains have increased in size significantly. In Figures 5.3 and 5.4 the division between the α phase (white) and the β phase (black) at the boundaries of the α grains is clearly seen. The arrows indicate some locations where the β phase is formed. The α grain thickness after heat treatment at 850 °C is measured to be 1.3 ± 0.3 µm and the α grain thickness after heat treatment at 1050 °C is measured to be 3.7 ± 1.1 µm.

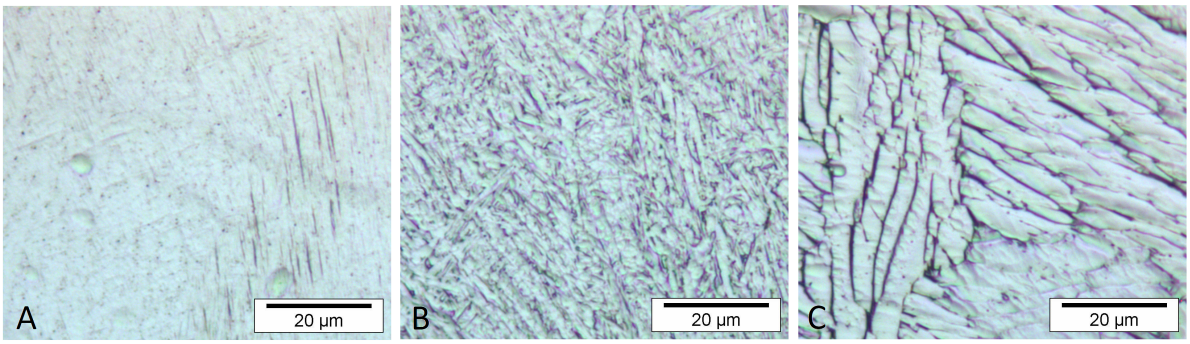

Figure 5.2: Microstructure of (a) an as-processed sample, (b) vacuum heat treated at 850 °C and (c) vacuum heat treated at 1050 °C at a magnification of 50x.

To investigate whether the change in α grain thickness is significant, a statistical analysis is conducted and the Z-scores and p-values are calculated which can be seen in Table 5.2.

It is clearly seen that the difference in α grain thickness is significant as the Z-score is above 1.96.

At high temperatures Ti6Al4V will consist of a BCC β phase and during cooling prior β grains will form in the material. When the temperature drops below the β transus temperature (995 °C) this beta phase is transformed into an HCP α + BCC β phase. The β phase will

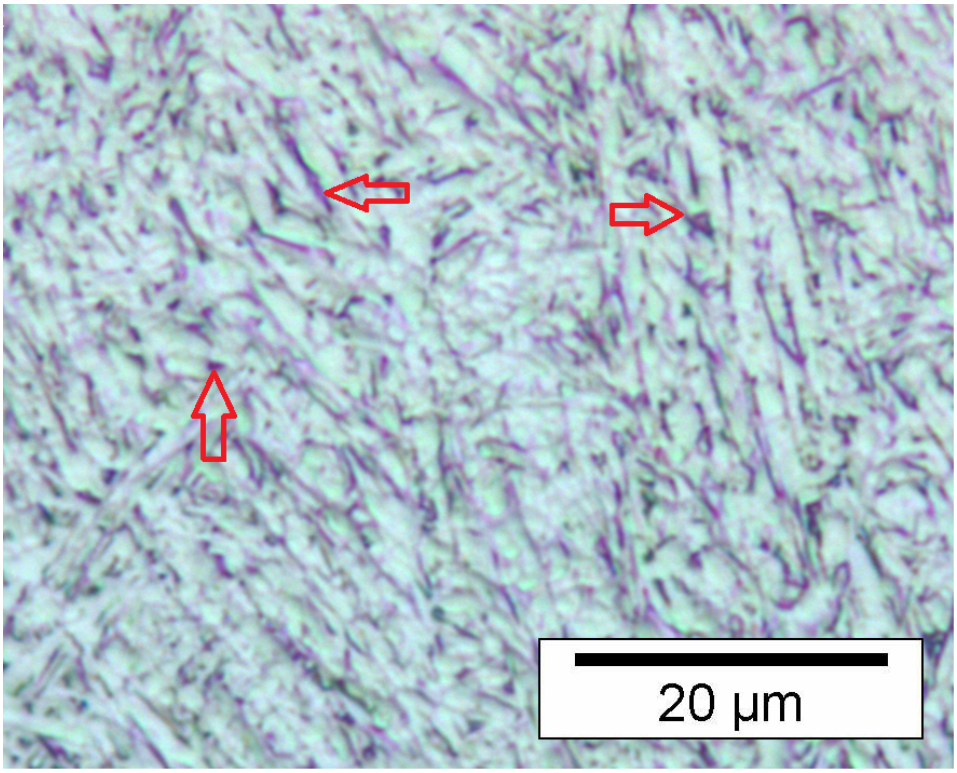

Figure 5.3: Microscopic picture of sample vacuum heat treated at 850 °C at an magnification of 50x and arrows indicating the present β phase.

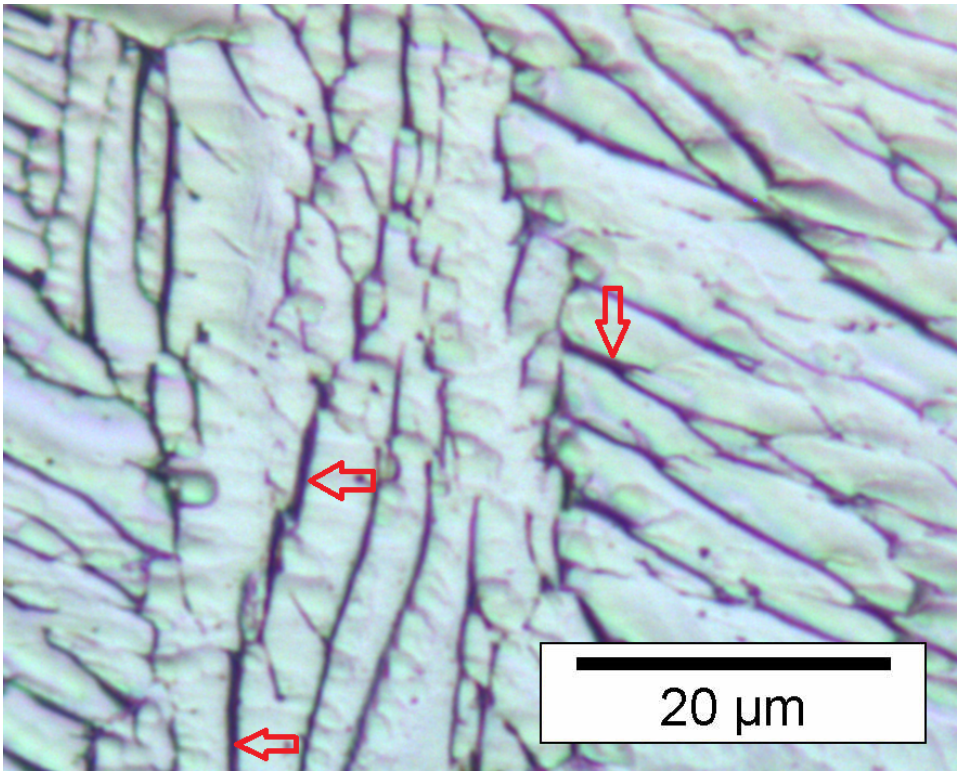

Figure 5.4: Microscopic picture of sample vacuum heat treated at 1050 °C at an magnification of 50x and arrows indicating the present β phase.

Table 5.2: Z-score and p-value of the measured α grain thickness for V850 and V1050 samples.

	Z-score	p-value
V850	13.3	<0.0001
V1050	13.3	<0.0001

remain present in the material because there is no room in the compact HCP structure of the α phase for vanadium. This results in the diffusion of vanadium from the α to the β phase. However, during rapid cooling using an SLM 3D printing process there is no time for diffusion and an diffusionless α'-martensite structure is formed with a distorted HCP structure. The α'-martensite is made from needle like laths. These laths are usually 0, 30, 60 or 90° inclined to each other [78]. The α'-martensite is supersaturated with β stabilisers (vanadium) and has a high dislocation density. An α'-martensite structure can be seen in Figure 5.2a

When heating samples with an α'-martensite structure, below the β transus temperature, nucleation of α and β phases are expected. This heat treatment should be performed above the α'-martensitic transformation temperature (575 °C) where the formation of α and β phases is favoured above keeping the α'-martensite phase [116]. The α phase will nucleate at the α'-martensite grain boundaries and due to the diffusion of vanadium a β phase will be formed at the α grain boundaries. This will continue until no α'-martensite is present in the material anymore. The size of α and β grains is limited by the size of the α'-martensite grains [49][103][106]. In Figure 5.2b it can be seen that as expected an α + β structure is formed from the 'α-martensite.

Metals like aluminium are α stabilisers and when they are dissolved in titanium only a few electrons will appear at the Fermi level, while most electrons will go to lower bands. The titanium electrons will avoid the aluminium atoms and will go to strengthen the Ti-Ti bonds which will preserve the HCP α structure. The final amount of α and β phase is determined by the amount of α stabilisers which will strengthen the α phase and the amount of β stabilisers which will form β phases. The exact amount of α and β phase is hard to measure from the microscopic pictures shown in Figure 5.2, but because the amount of α and β stabilisers will determine the amount of α and β phase and a common titanium alloy powder is used for printing, this can be estimated by looking at the literature.

Heating above the β transus temperature (995 °C) is a completely different story. Above this temperature a 100% β will exist and the limiting 'α-martensite grains will disappear. Now prior β grains will appear which will increase in size with an increasing residence time. The size of these prior β grains will eventually limit the maximum size of the α and β grains. However, when heating above the β transus temperature the cooling rate will determine the size of the α and β grains when this size limitation is not reached. High cooling rates will result in many α nuclei which will result in small α grains and even higher cooling rates will result into 'α-martensite grains. Reducing the cooling rate will result in a increase in grain size [78][79][103]. When comparing Figures 5.2b and 5.2c it can be seen that with the removal of the 'α-martensite size limitation and the reduction of the cooling rate (from quenching to 10°C/min) the α grain thickness size is almost 3 times larger. The α grain thickness after heat treatment at 850 °C is measured to be 1.3 $\pm$ 0.3 µm and the α grain thickness after heat treatment at 1050 °C is measured to be 3.7 $\pm$ 1.1 µm.

Internal porosity

In Table 4.3.4 the average internal porosity of the as-processed samples, heat treated at 850 °C and heat treated at 1050 °C including the standard deviation.

In Figure 5.5 an example is provided of the internal porosity of the SLM 3D printed material

Table 5.3: The average internal porosity of as-processed samples, samples heat treated at 850 °C and samples heat treated at 1050 °C.

	Internal porosity (%)
AP	0.60 ± 0.11
V850	0.64 ± 0.06
V1050	0.59 ± 0.10

including the diameter of some defects to give an idea of the size of the defects found in the material. The minimal size of pore which can be detected with this method is 70 nm.

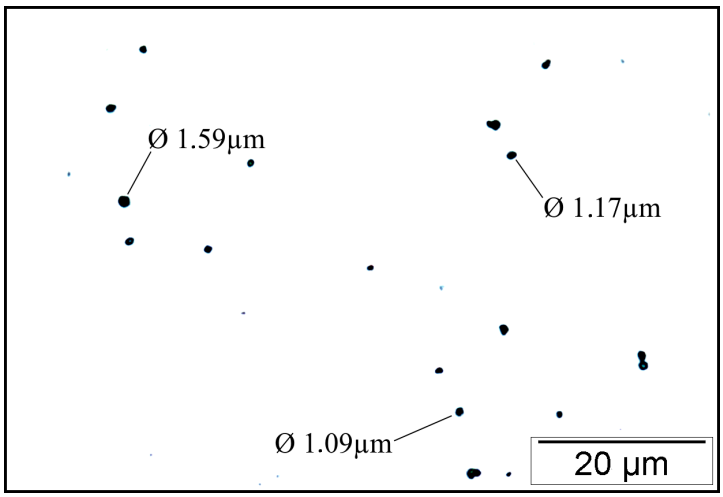

Figure 5.5: Internal porosity of as-processed sample at a magnification of 50x.

To check whether there is a significant difference between the three average internal porosities measured, a statistical analysis is performed where the Z-score and the p-value are calculated. These values are shown in Table 5.4.

Table 5.4: Z-score and p-value of the measured internal porosities for AP, V850 and V1050 samples.

	Z-score	p-value
AP	0.35	0.73
V850	1.05	0.29
V1050	0.70	0.48

It can be seen that no significant difference between the measured internal porosities is found as no Z-score exceeds 1.96.

HIP has shown to drastically decrease the size of the internal pores, but looking at Table 5.3 it can be seen that heat treating the material in a vacuum oven does not affect the internal porosity. Also no difference is detected between heating above and below the β transus temperature. This is expected because no high pressure is applied during the heat treatment, which could deform the material around the pores to reduce their size. This makes a heat treatment in a vacuum or with argon comparable in terms of the effect on the internal porosity. Looking at Table 2.5 in Chapter 2, different internal porosities are measured which showed that the printing process already has a big influence on the internal porosity. Gong et al. [36] even showed that a reduction of 5 times the original internal porosity can be achieved

when changing the 3D printing parameters. In Section 2.3.1 it was discussed that the internal porosity influences the fatigue life of the material. However, the effect of the internal porosity on the fatigue life was not this noticeable when working with a lattice structure. Now it will be interesting to see the effect of the internal porosity on the fatigue life of the material.

X-ray diffraction

Three different samples are tested using XRD: as-processed; heat treated for 2 hours at 850 °C; and heat treated for 2 hours at 1050 °C. The as-processed samples and the heat treated samples received different measurement methods, which makes the data hard to compare. For the as-processed sample Co radiation is used and for the heat treated samples Cu radiation. To solve this 2θ is changed to d-values using Bragg's law where n = 1, θ_{Cu} = 1.54060 Å and θ_{Co} = 1.78897 Å.

$$n\lambda = 2dsin\theta \tag{5.1}$$

The d-values are material properties, so the peaks will be at the same locations and can therefore be compared. The number of counts is also not the same, so all values are divided by the total count to be able to compare the relative height of the graphs. The resulting graphs can be seen in Figure 5.6 and the original graphs can be seen in the Appendix.

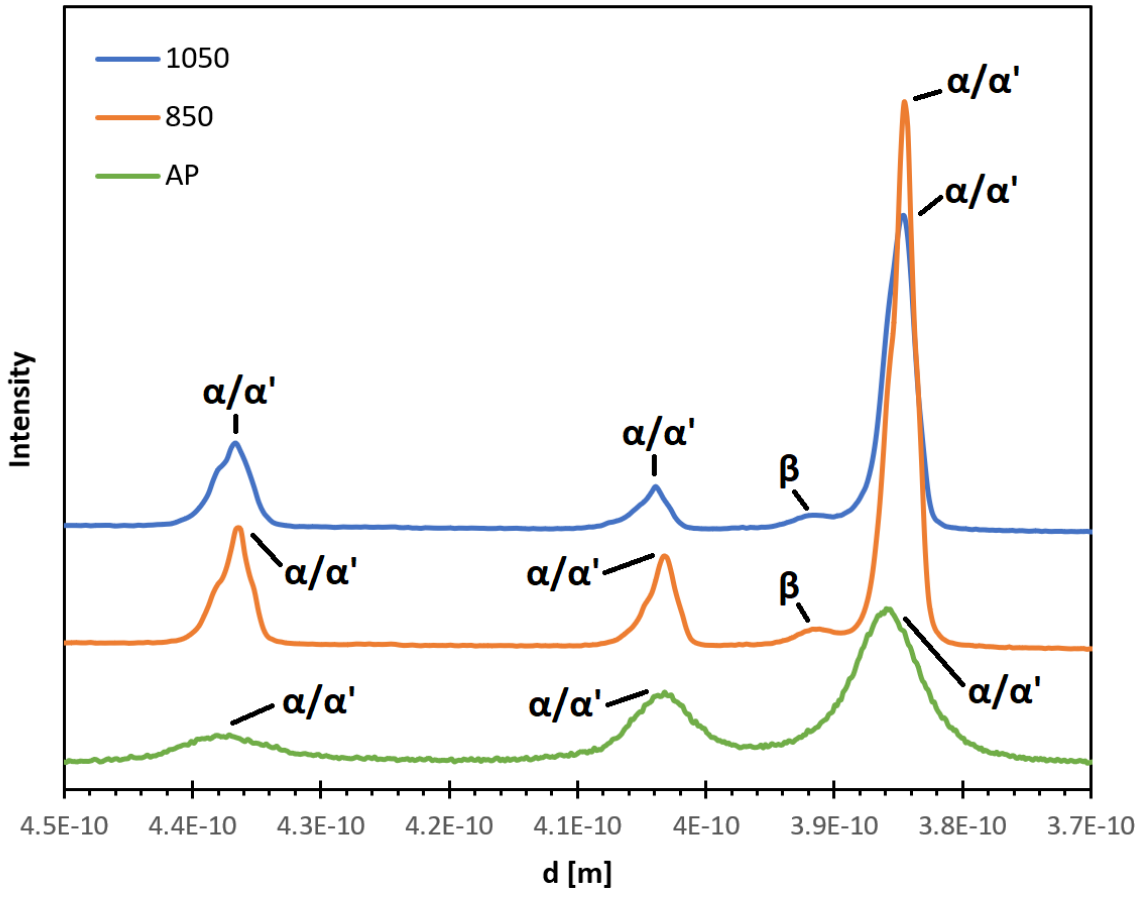

Figure 5.6: XRD measurements of as-processed, vacuum heat treated at 850 °C and vacuum heat treated at 1050 °C samples.

Looking at Figure 5.6 it can be seen that for the heat treated samples α/α'-martensite and β peak can be found. For the as-processed sample only α/α'-martensite are found. Because α

and α'-martensite phases will create a peak at the same location it is hard to distinguish these phases. However, there are some indications which makes it possible to make a prediction about which phase is present. Usually α'-martensite peaks are wider compared to α peaks due to the distorted α'-martensite structure. Another indication would be the presence of a β peak, because to create an α phase vanadium has to diffuse out of the α'-martensite phase and this will create a β phase. In the previous section it is discussed that for the as-processed samples an α'-martensite microstructure is expected and for the heat treated samples an α + β structure. The XRD graph for the as-processed sample shows wide peaks and no β phase which would suggest an α'-martensite microstructure and the XRD graphs from the heat treated samples show narrow α/α'-martensite peaks and β peaks which suggests a α + β microstructure. Peaks at other locations would indicate oxidation, but no unexpected peaks were found. In the XRD graphs shown in the Appendix a third type of peak is indicated which is caused due to the Co or Cu in the incident beam.

5.1.2. Quasi-static compression tests

Three samples with two different post processes are tested using a quasi-static compression test. The samples tested are as-processed, heat treated at 850 °C and heat treated at 1050 °C. The results of these tests are shown in Figure 5.7, 5.8 and 5.9

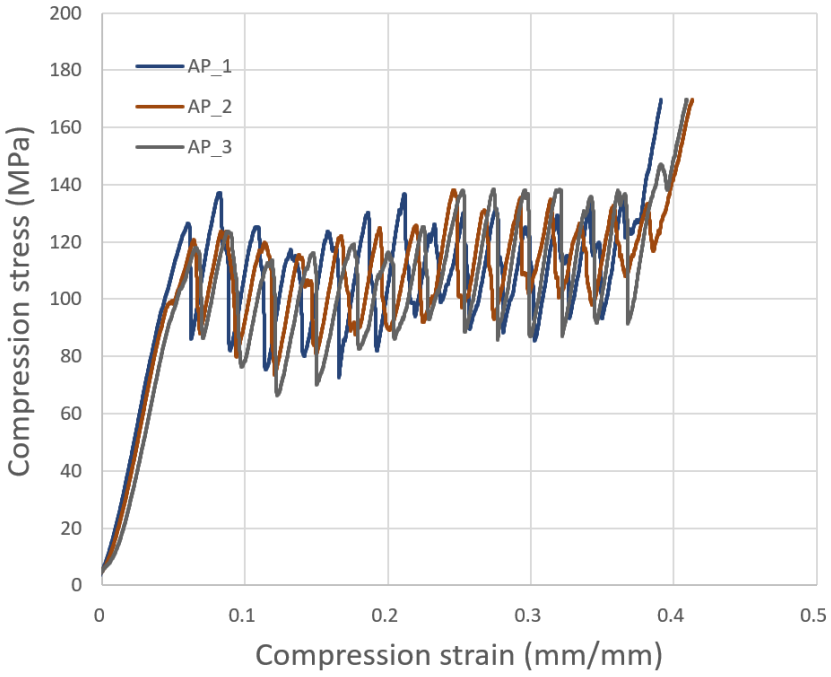

Figure 5.7: Stress-strain graph of as-processed samples from compression tests.

From these graphs the apparent Young's modulus and the yield strength are found and shown in Table 5.5.

To investigate whether a significant difference of the apparent Young's modulus and the yield stress between the different heat treatment is found, a statistical analysis is performed in order to find the Z-score and the p-value. In Table 5.6 it can be seen that for the Young's modulus there is no Z-score below 1.96, so a significant difference is found between these values. For the yield stress a Z-score below 1.96 is found for the vacuum heat treatment at 850 °C, because this value was probably close to the value estimated, assuming all the yield stresses are expected to have the same value. The other Z-values are above 1.96, so still a

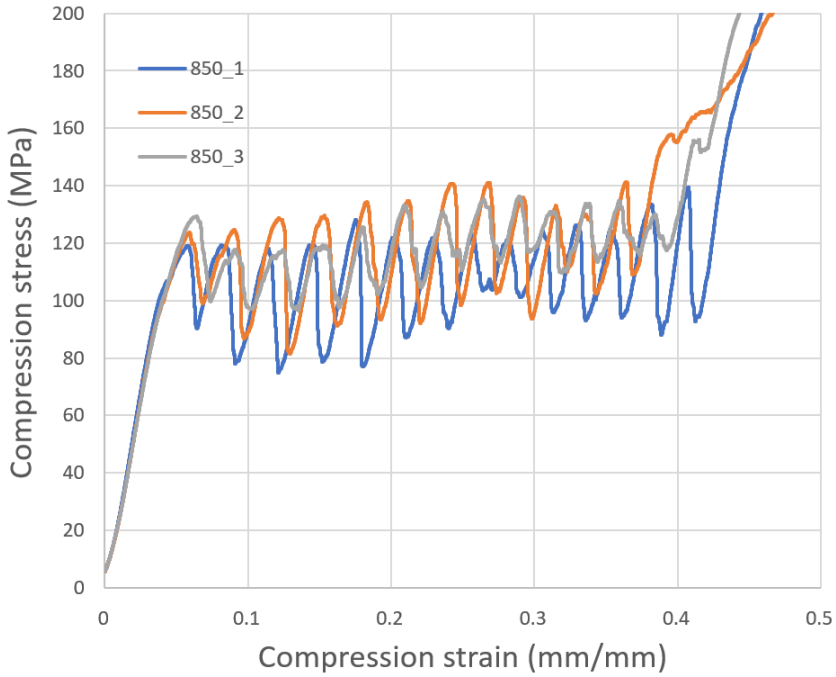

Figure 5.8: Stress-strain graph of 850 °C samples from compression tests.

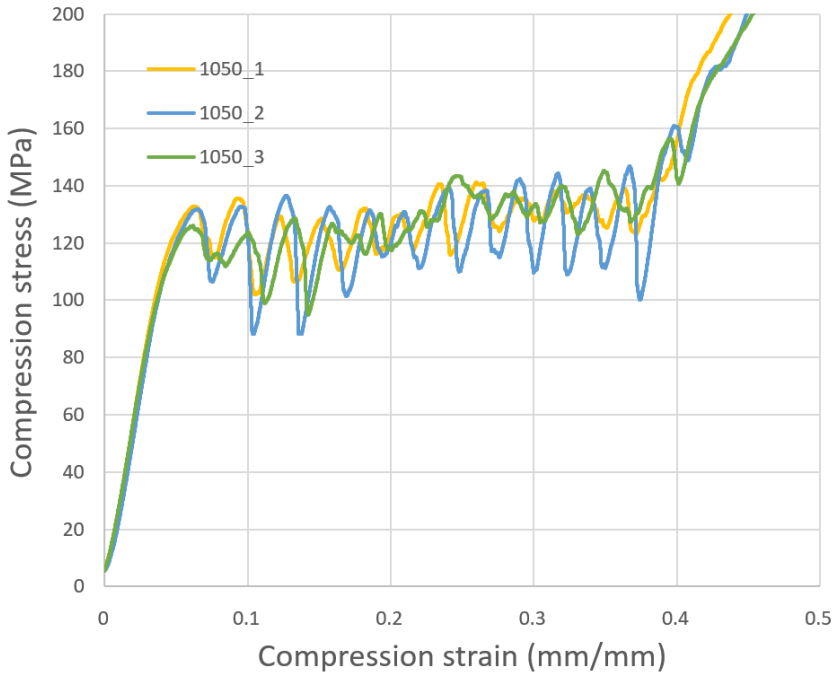

Figure 5.9: Stress-strain graph of 1050 °C samples from compression tests.

significant difference between the three values is found.

During heat treatment at 850 °C and 1050 °C the 'α-martensitic microstructure will transform into an α + β structure. This will affect the Young's modulus of the material because all three phases have a different Young's modulus. The transformation of 'α-martensite to β will reduce the Young's modulus and the transformation of 'α-martensite to α will increase the Young's modulus. This is because the α has a higher Young's modulus compared to 'α-martensite

Table 5.5: Apparent Young's modulus and yield stress of cylindrical sample with different heat treatments.

	As-processed	Heat treatment 850 °C	Heat treatment 1050 °C
Apparent Young's modulus (GPa)	2.48 $\pm$ 0.05	2.81 $\pm$ 0.07	2.96 $\pm$ 0.04
Yield stress (MPa)	84 $\pm$ 6	98 $\pm$ 2	105 $\pm$ 3

Table 5.6: Z-score and p-value of the measured Young's modulus and yield stress for AP, V850 and V1050 samples.

	Z-score apparent Young's modulus	p-value apparent Young's modulus	Z-score yield stress	p-value yield stress
AP	9.35	<0.0001	5.38	<0.0001
V850	2.08	0.038	1.06	0.29
V1050	7.27	<0.0001	4.43	<0.0001

and β has a lower Young's modulus compared to 'α-martensite. Looking at Table 5.5 it can be seen that with both heat treatments the apparent Young's modulus is increased. This increase indicates that the effect of the 'α-martensite to α transformation prevailed over the 'α-martensite to β transformation.

When comparing the heat treated samples it can be seen that the apparent Young's modulus of the samples heat treated at 1050 °C have a slightly higher apparent Young's modulus compared to the samples heat treated at 850 °C. However, when looking at the results of the XRD measurements it was found that the heat treated samples at 1050 °C have a similar concentration of β phase. The β phase count for both heat treatments was around 8800. Moreover, the apparent Young's modulus of the samples heat treated at 1050 °C was expected be similar compared to the samples heat treated at 850 °C if the apparent Young's modulus is purely determined by the concentrations of each phase.

This could possibly be explained by the α grain thickness of the samples. As seen in Figure 5.2 the α grain thickness of the samples heat treated at 1050 °C are a lot larger compared to the α grain thickness of the samples heat treated at 850 °C. This is because if the material is heated below the β transus temperature the material is limited by the size of the prior β grains and not able to grow any larger. Above the β transus temperature the grain size is not limited. The α grain thickness size measured for the samples heated below the β transus temperature at 850 °C was 1.3 $\pm$ 0.4 µm and above the β transus temperature at 1050 °C it was 3.7 $\pm$ 1.1 µm. This small grain size causes the material to consist of a lot of grain boundaries and triple junctions. The Young's modulus at these grain boundaries and triple junctions is lower compared to the Young's modulus of the material itself. In materials with a large intercrystal volume fraction (like 3D printed Ti6Al4V heat treated at 850 °C) this could lower the Young's modulus of the sample. In literature the material nickel-iron was tested and when the average grain size was below 20 µm a drop in the Young's modulus was observed [30]. Kim et al. (2012) also found a drop in the Young's modulus when the grain size was reduced. [54]. Finally, Zhou et al. (2003) found a decrease in Young's modulus for NiP for grain sizes below 18 µm. They also tested the Young's modulus of grain boundaries and triple junctions which was 76% and 73% of the original Young's modulus respectively [124].

It was observed that the yield stress will increase when the samples are heat treated at 1050 °C instead of 850 °C. This would mean that an increasing α grain thickness will result

in an increase in yield strength. However, this is against the Hall-Petch relationship, which is given by the following formula:

$$\sigma_y = \sigma_0 + \frac{k_y}{\sqrt{d}} \tag{5.2}$$

In this equation σ_0 and k_y are material constants, so the yield strength (σ_y) will decrease when the grain size (d) increases. Zhang et al. [123] found this to be true for heat treatments at different temperatures below the β transus temperature, so a decrease in yield strength is expected and not an increase. Yan et al. [120] did find an increase in yield strength when heat treating above the β transus temperature. According to them this is due to the formation of an α colony microstructure. Another explanation could be the presence of $'\alpha$ - martensite in the material heat treated above the β transus temperature. During heat treatment below the β transus temperature $'\alpha$ - martensite will transform into an α + β structure due to vanadium diffusion. When heat treating the material above the β transus temperature the $'\alpha$ - martensite will transform into β and when cooling the β phase will transform to an α phase with β phase at its grain boundaries due to the vanadium diffusion. When a high cooling rate is applied after heat treatment above the β transus temperature an $'\alpha$ - martensite structure will be formed since vanadium has no time to diffuse. This is not the case for heat treatments below the β transus temperature because the vanadium is already diffused. Jovanovic et al. [48] heat treated Ti6Al4V at 850 °C and 1050 °C for 1 hour and cooled the samples using water quenching. The sample heat treated at 850 °C had 10% $'\alpha$ - martensite and the sample heat treated at 1050 °C had 95% $'\alpha$ - martensite. When the cooling rate decreases, the amount of $'\alpha$ - martensite also decreases until no $'\alpha$ - martensite is present anymore in the material. To reduce this amount of $'\alpha$ - martensite the samples were heat treated at 10 °C/min, but due to the higher yield strength found it could be there is some $'\alpha$ - martensite in the samples heat treated at 1050 °, which would also explain the higher yield stress.

5.1.3. Fatigue properties

For the fatigue tests three different samples are tested: as processed, vacuum heat treated at 850°C and 1050°C. Each sample is tested three times at 75%, 50% and 35% of its yield strength. In Figure 5.10 the results from the fatigue tests are shown. The local stress is calculated for all measurement to remove the effect of sample dimensions and to get a better approximation of the true stress. This local stress is normalised to a porosity of 65% to remove the effect of different strut thicknesses. How the local stress is calculated and how the data is normalised is explained in Section 4.3.1. The data is normalised to a porosity of 65%, because this is close to all the different porosities measured. From these results it can be seen that the shape of the fatigue graphs are similar. The vacuum heat treatment improves the fatigue life of the material by 20% and, finally, there does not seem to be a significant difference in fatigue life between the two different heat treatments.

In Figure 5.11 three fatigue graphs are added from a different study [11]. The samples tested to produce these graphs were produced using exactly the same 3D printing process and an identical design. The graphs added are from as-processed samples, samples heat treated with HIP at 920 °C for 2 hours and HIP heat treated samples including sandblasting and chemical etching. It can be seen when comparing these three graphs that applying HIP on the as-processed samples will improve the fatigue life and adding sandblasting and chemical etching will improve the fatigue life even further.

All the different samples tested to create the fatigue graphs in Figure 5.11 are produced in two different batches. Two different fatigue graphs are produces from both batches which can be seen in Figure 5.12. There is no difference observed between the fatigue graphs of

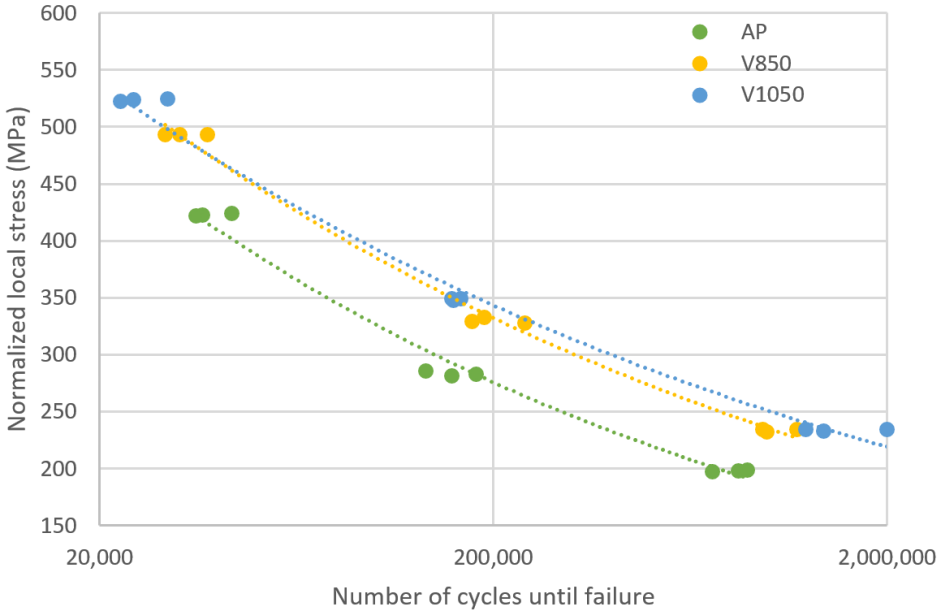

Figure 5.10: Normalised fatigue graph of as-processed, 850 °C and 1050 °C samples.

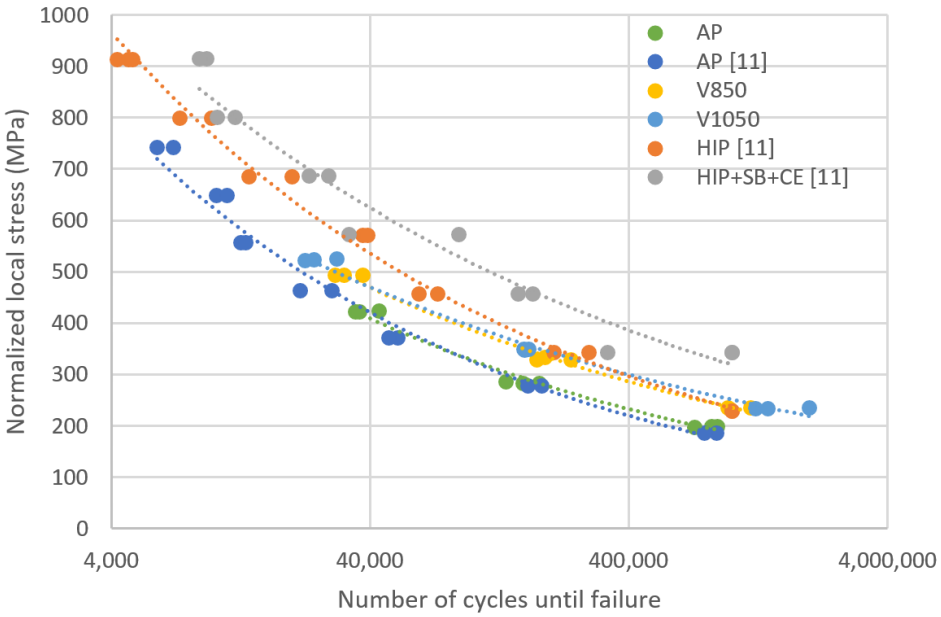

Figure 5.11: Normalised fatigue graph cylindrical samples.

the as-processed samples.

Finally, in Figure 5.13 the fatigue graphs of the samples which received a heat treatment without any surface treatment are shown. In this case a fatigue life lower that 100,000 cycles is studied as low cycle fatigue (LCF) and a fatigue life above 100,000 cycles is studied as high cycle fatigue (HCF) [49]. It can be seen that for LCF the fatigue life of the HIP heat treated samples is higher compared to the samples heat treated in a vacuum atmosphere. At 30,000 cycles the fatigue life of HIP heat treated samples is 15% higher. However, when looking at HCF no difference in fatigue life can be seen between all three heat treatments. At 1,000,000 cycles the fatigue life of HIP treated samples is 1% lower.

After 3D printing the material is expected to have a high amount of residual stress due to

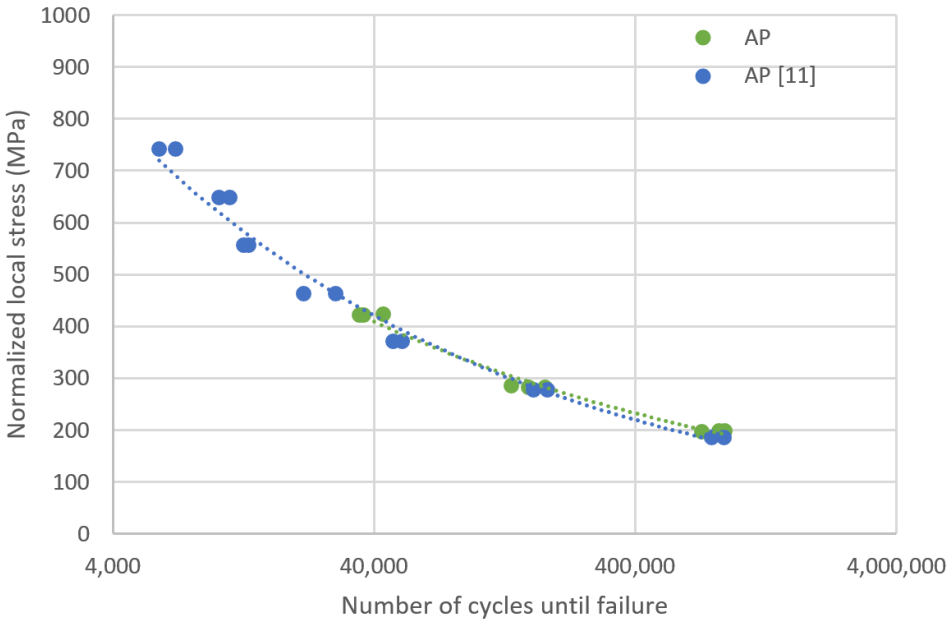

Figure 5.12: Normalised fatigue graph as-processed samples.

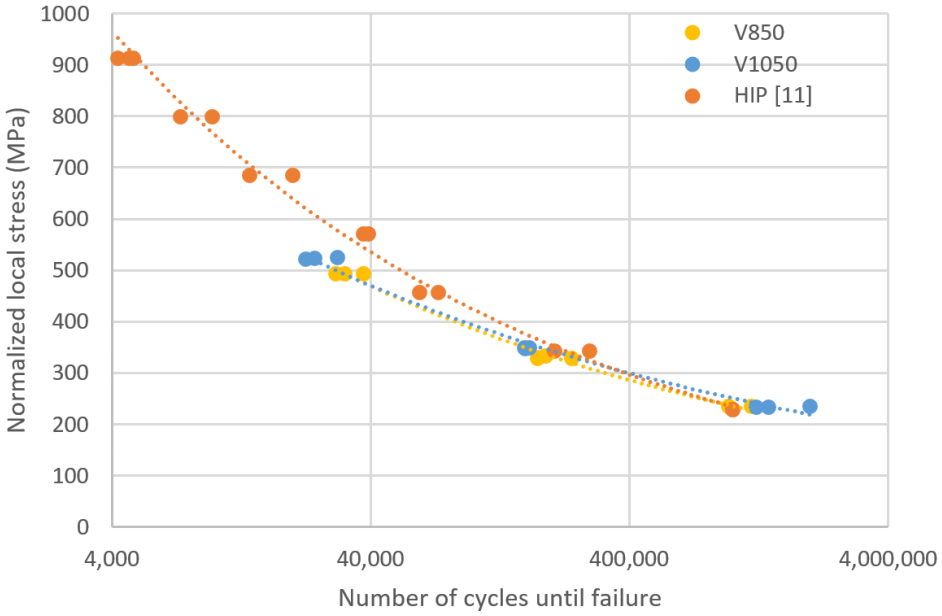

Figure 5.13: Normalised fatigue graph of heat treated cylindrical samples.

the large temperature gradients during 3D printing using SLM [117]. This residual stress will consist of compressive stresses and tensile stresses. The compressive stresses are actually beneficial to the fatigue life of the material, while the tensile stresses add additional driving forces for crack initiation and propagation. During heat treatment this residual stress will be removed. The removal of these residual stresses will decrease the crack growth rate which will increase the fatigue life of the material [96]. The applied heat treatment will not only remove residual stresses, but also the microstructure will change during heat treatment. The as-processed samples will have an 'α-martensite structure which will transform into an α + β microstructure during heat treatment. Small amounts of 'α-martensite can improve the fatigue life by reducing the crack propagation rate, but this effect is quickly removed when the

'α-martensite concentration increases. Also a fully α + β structure is required by the ASTM standards. The as-processed material is fully 'α-martensite which has a high fraction of dislocations. This will lead to a high concentration of micro cracks which could reach the main crack and increase the crack propagation velocity reducing the fatigue life. Finally, because of the transformation of 'α-martensite to an α + β microstructure the yield strength of the material will increase. Hosseini et al. [43] observed that an increase in strength will also lead to an increase in fatigue life [67]. In Figure 5.10 the effect of removing the residual stresses in combination with the change in microstructure can be seen. The fatigue life of the heat treated samples is increased significantly by 20%. It can not be seen what the effect of residual stress and microstructure is on the fatigue life separately. This will be interesting to further investigate to see if one has a more dominant effect on the fatigue life or if the effect is similar.

Looking again at Figure 5.10 there seem to be no significant difference between the fatigue life of the samples vacuum heat treated at 850 °C and 1050 °C. However, the big difference between the samples which was found, is the α grain thickness. The α grain thickness found at the samples heat treated at 850 °C was 1.3 $\pm$ 0.4 µm and at 1050 °C 3.7 $\pm$ 1.1 µm. Several papers indicate that an increasing amount of α phase will first increase the fatigue life and when the α concentration increases the fatigue life will decrease again. Wu et al. [111] found that an α phase concentration between 30 and 50 % will result in the best HCF life. Wu et al. [111] also indicate that a reduction in the width of the α grains will increase the fatigue life of the material [43][67][111]. A range between 2.8 to 20 µm was tested and a reduction of HCF life was observed with an increase in α grain thickness. This can be explained because this microstructure will induce crack deflection, branching and closure which will lower the crack propagation rate and this effect is increased with a reduction in α grain thickness. Zuo et al. [125] also mentioned that with HCF crack initiation will play a dominant role and not crack propagation. Comparing the two heat treatment there is a significant difference in the α grain thickness, so for the heat treatment at 850 °C a higher fatigue life is expected. This is not the case, which would indicate that the α grain thickness does not have a large effect on the fatigue life. An explanation for this could be the surface quality of the samples. It is generally known that a bad surface quality can drastically decrease the fatigue life of your samples. In this case the samples did not receive any form of post surface treatment in the form of sandblasting or chemically etching, which could improve the surface quality. Ahmadi et al. [3] tested the effect of sandblasting and chemical etching separately and looking back at Figure 2.13 in Chapter 2, it was shown that this did not have a positive effect on the fatigue life. However, in Figure 5.11 a combination of sandblasting and chemical etching was applied on HIP heat treated samples which did have a large positive effect on the fatigue life [11].

Looking at Figure 5.13 three graphs are shown, which are HIP heat treatment for 2 hours at 920 °C (orange line), vacuum heat treatment for 2 hours at 850 °C (yellow line) and vacuum heat treatment for 2 hours at 1050 °C (blue line). It can be seen that all samples are heat treated with the same duration, but at different temperatures. The main effect of this change in temperature will be the grain size. Vrancken et al. [103] found an increase in α grain thickness from 1.27 $\pm$ 0.13 µm to 2.23 $\pm$ 0.12 µm when the temperature is increased from 850 °C to 950 °C during vacuum heat treatment for 2 hours. From measurements performed in this report an increase in α grain thickness from 1.3 $\pm$ 0.4 µm to 3.7 $\pm$ 1.1 µm is found when the temperature is increased from 850 °C to 1050 °C during vacuum heat treatment for 2 hours. If the fatigue life is only determined by the microstructure it is expected that the fatigue life of the HIP heat treated samples will be between the fatigue life of the vacuum heat treated samples at 850 °C and 1050 °C. However, as discussed before there are no significant differences observed between the two vacuum heat treatments even though the resulting samples having a considerable difference in α grain thickness.

The main difference between the HIP heat treatment and the vacuum heat treatment is the internal pore size. Looking at Figure 5.13 again the reduction in internal pore size seems to improve the LCF, however, for HCF no significant difference in fatigue life is observed. Looking back at Figure 5.11 it was shown that adding sandblasting and etching to the post treatment improves the fatigue life. Taking a closer look at this improvement of fatigue life, it can be observed that the biggest improvements are made by comparing HCF and not LCF. This could indicate that the surface quality has a bigger influence at HCF compared to LCF, which explains why no difference is seen between the HCF of the two heat treatments, since the surface quality had a dominant influence on the fatigue life. Looking at literature it is found hat the crack propagation threshold (ΔK_{th}) is higher and the crack growth rate is lower for internal defects compared to surface defects. The internal defects and surface defects will compete with each other as primary crack initiation sites. Murakimi et al. [75] found that the internal defects should be at least 1,6 times bigger compared to the surface defects in order to become a crack initiation site [16][60]. This means that the internal defects will lose their effect on the fatigue life quicker compared to the surface defects when the applied load is reduced. This would explain why at LCF (higher loads) the HIP heat treatment outperforms the vacuum heat treatment, since at higher loads the fatigue life is determined by a combination of internal and surface defects. Due to the pressure used during HIP the effect of the internal defects is reduced. When looking at lower loads (HCF) the effect of internal defects is already reduced and the fatigue life of HIP heat treated samples and vacuum heat treated samples will be similar.

In this case the material is investigated to be used for a spinal cage and, because spinal cages will operate in the HCF range, the LCF is not as interesting when considering the material choice. When comparing the HCF of the HIP heat treated samples and the vacuum heat treated samples no difference in fatigue life is observed and it can be concluded that vacuum heat treatment is a good alternative for HIP. However, this will only be the case when the choice is made not to apply a surface treatment. As discussed only using chemical etching or sandblasting is not expected to improve the HCF life, but using a combination will. The difference in HCF should be investigated between HIP and vacuum heat treatment including both surface treatments. If there will be a difference now a new conclusion should be made if this difference is worth the high costs of HIP. The surface quality has a very dominant influence on the fatigue life because the surface area is very big due to the lattice structure. Back in Figure 2.12 the fatigue graphs of solid 3D printed Ti6Al4V showed that you can potentially have a large difference in fatigue life between HIP and argon heat treated material if the surface area is reduced. If improving the surface quality has the same effect as reducing the surface area and if vacuum heat treatment and argon heat treatment have a similar effect on the fatigue life, then a difference in HCF is expected.

5.2. PLIF spinal cage design

In Figure 5.14 the PLIF design provided by Amber Impants is shown. As discussed earlier there are three main problems with this design. First of all, the apparent Young's modulus is significantly higher compared to the surrounding bone reducing the performance of osseointegration [41]. The other problems are stress shielding and high stress concentrations, which are created by the design of the implant. During testing of the cylindrical samples, which have comparable dimensions to the PLIF, it was found that the cylindrical samples had a comparable yield strength and fatigue life compared to the PLIF design showed in Figure 5.14, but the apparent Young's modulus was a lot closer to the Young's modulus of the surrounding bone. These findings resulted in the idea that a completely porous implant with a suitable 3D printing process could have an acceptable fatigue life and strength while lowering the apparent

Young's modulus significantly. Moreover, as described in Chapter 2, it was found that a spinal cage will be able to perform a spinal fusion even without allo and auto graphs. Using this information the choice was made to remove the holes present for allo and auto graphs and fill these holes with porous material, which increases the strength of the spinal cage without increasing the apparent Young's modulus.

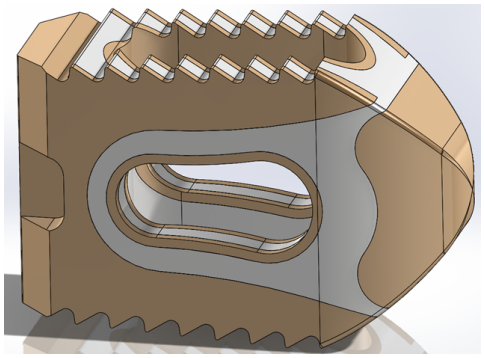

Figure 5.14: SolidWorks model original spinal cage design.

The other structural change is removing the teeth at the top and bottom surface of the implant. As mentioned before the teeth are there to provide additional grip because the vertebrae are inclined with respect to each other, loading the implant may cause movement of the implant. However, the porous structure will already provide a good grip due to the rough surface created.

At this point this leaves us with a completely porous implant without holes and without teeth, but apart from providing extra strength to the implant the solid material can also have different functional roles like preventing damage to the bone and providing a strong part used for insertion.

The teeth can be removed because the porous surface will already provide a good grip. However, this can also cause a lot of damage due to scraping during insertion of the implant. Two parts of the implant which will cause the majority of the damage are the tip of the implant and the edges. The easiest way to make the tip and the edges of the implant smoother is by applying a layer of solid material. The original design already worked with a separate tip to reduce scraping of the implant. For the new design similar tips are investigated. The edge will also be made from solid material and ideally the amount of solid material should be as little as possible. However to ensure a good connection between the solid material at the edge and the surrounding porous material the thickness of the solid material at the edge needs to be at least the size of a unit cell of the porous material. As visualised in Figure 5.15 the choice is made to not make a connection between the solid edges and the solid tip of the implant.

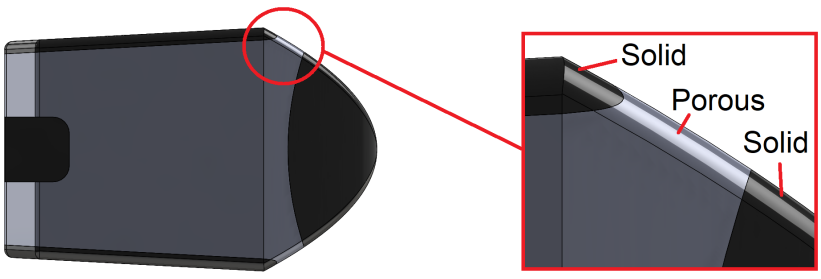

Figure 5.15: SolidWorks model of the new spinal cage design.

This choice will probably cause some damage to the bone during insertion because the porous material is exposed between the solid tip and the solid edge. However, connecting the solid sides to the tip will lead to the creation of a bridge of solid material between the top and the bottom of the material. Due to the higher apparent Young's modulus of this solid bridge a lot of stress will channel through this solid material, increasing the chance of failure in the solid material and causing stress shielding in the surrounding porous material which in turn leads to decreased chances of successful osseointegration.

Finally, there is one more location where solid material is required. To operate the spinal cage during insertion and positioning there are two ways to grip the implant using tweezers to clamp the implant or by attaching a screw in the threaded hole. This results in a block at the back of the implant with a hole and additional space surrounding this block to grip the implant. This block should have similar dimension compared to the original implant.

The implant can be separated in four different parts: the porous base of the implant, the solid tip, the solid edges and the solid block at the back. An example to visualise these parts is shown in Figure 5.16.

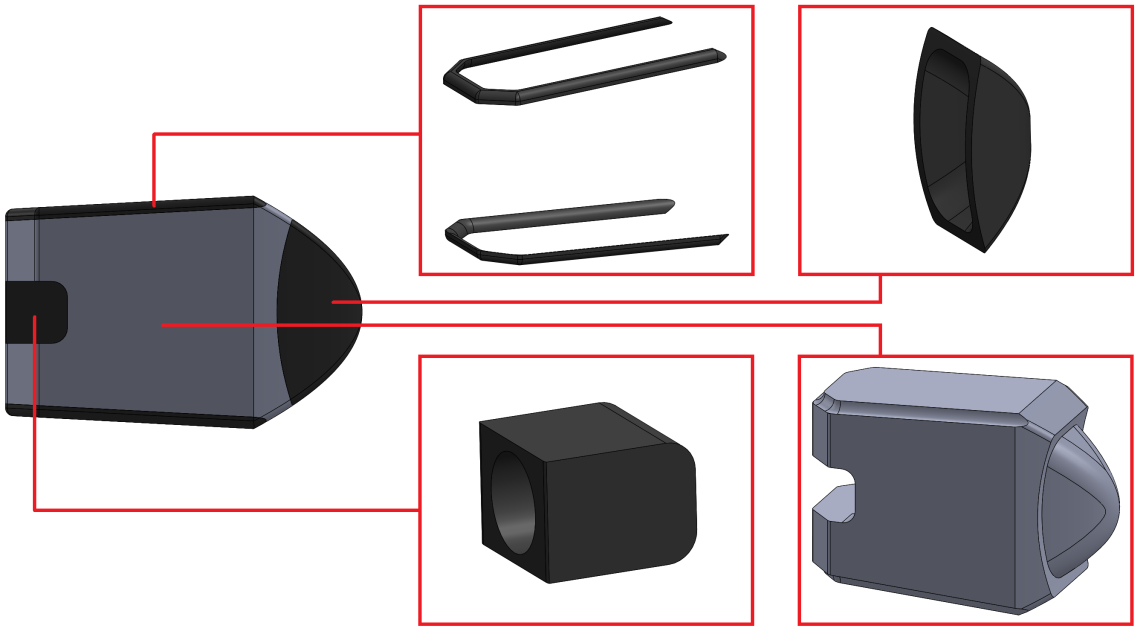

Figure 5.16: SolidWorks model of the new spinal cage design.

Now for each of these parts several designs can be tested and from these tested designs the best performing part can be selected. First of all, several designs for the tip are tested. To explain how these designs are generated the design limitations should be explained. As discussed earlier the choice was made not to change the outer dimensions of the implant. This results in the same outer shape of the different tip designs. Apart from this the choice was made not to change the height of the tip so the amount of exposed porous material between the tip and the edges will be the same. Now the two main changes which can be made are the shape of the tip at the solid porous interface and the wall thickness of the tip. Looking at Figure 5.17 several different designs are tested using a compression test in COMSOL. The second tip shown in Figure 5.17 is currently used for the original design. The large red areas in this design visualise large stress concentrations in the material produced due to the wave like shape of the tip. Looking at the other tips it is shown that these large stress concentrations can be reduced by either changing the shape of the tip or the wall thickness. It is important to

note that a thinner wall thickness will mean a lower apparent Young's modulus for the implant, because a smaller amount of solid material will be present. From these results it was decided to investigate the new shape visualised in Figure 5.17 as the fourth design from the left.

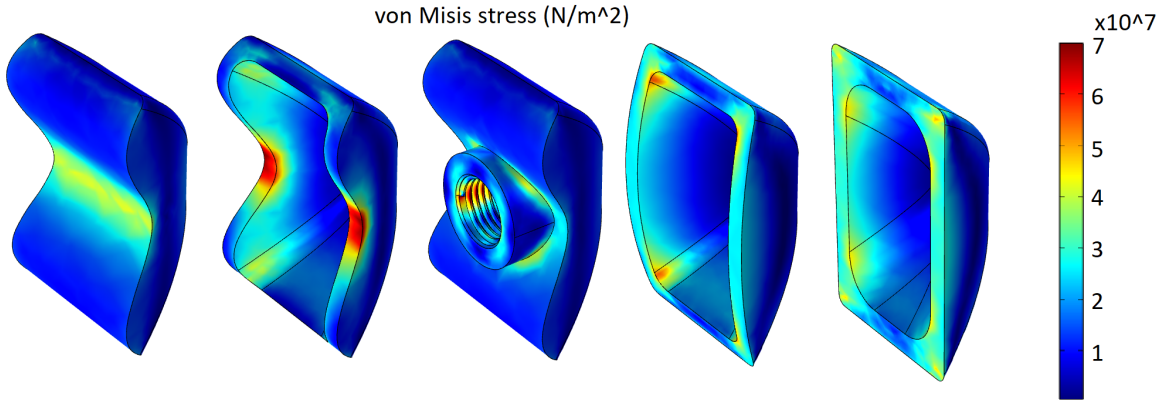

Figure 5.17: Simulated compression test of the tip of the spinal cage using COMSOL.

Looking at Figure 5.18 it is clear that the stress concentration in the material is dependent on the wall thickness of the tip. When the wall thickness increases the height of the von Mises stresses found in the material reduces. However, the lowest apparent Young's modulus in the implant will be found with the smallest wall thickness. Concluding the smallest wall thickness should be chosen where no high stress concentrations are found. Looking at Figure 5.18 the results shown for the third design look very promising, resulting in the third tip from the left being chosen to be used for the new design.

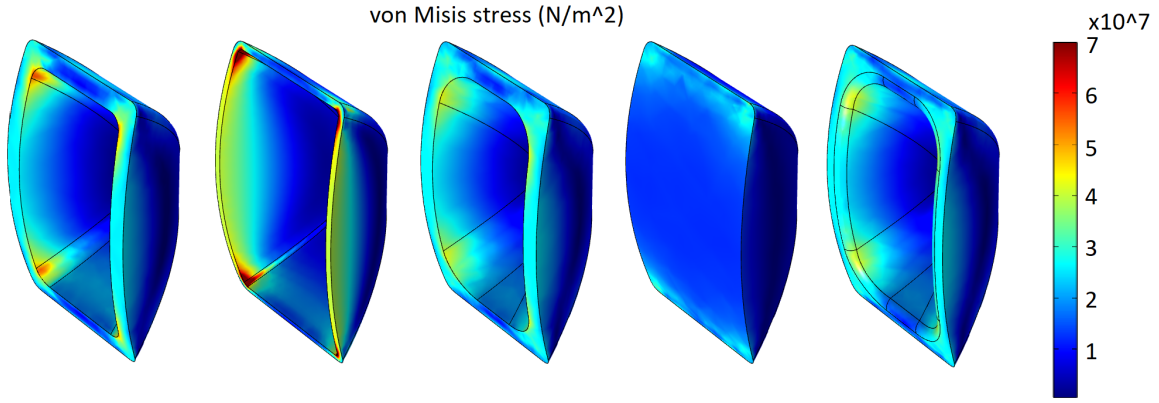

Figure 5.18: Simulated compression test of the tip of the spinal cage using COMSOL.

In Figure 5.19 two different designs are shown for the back of the implant. The design on the left is created by trying to create a solid part as small as possibly without losing functionality. To function properly the threaded hole should be surrounded by solid material and there should be enough space to grip the solid part with medical tweezers. Looking at the simulation on the left in Figure 5.19 no dark red colour is observed, meaning very high stresses are not expected. On the right another design is created with additional supporting solid material and it is clearly seen the peak stresses in the part are dropped significantly. For the new design the part show on the left in Figure 5.19 is chosen to achieve the lowest apparent Young's modulus for the spinal cage.

During testing of the implant low amounts of stress were found at the middle of the implant

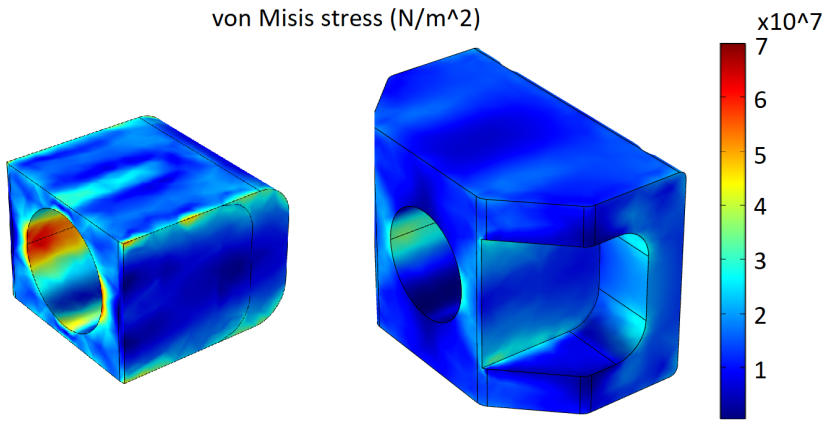

Figure 5.19: Simulated compression test of the back of the spinal cage using COMSOL.

as can be seen on the left in Figure 5.20. This resulted in the idea to test a spinal cage with additional holes for allo and auto grafts and how this will affect the surrounding material. If these holes would only have a small effect on the surrounding material this would result in a new design with a lower apparent Young's modulus and the option for allo and auto grafts. However, as seen in the right of Figure 5.20 the stress concentrations found in the material become significantly higher, resulting in the decision not to investigate this any further.

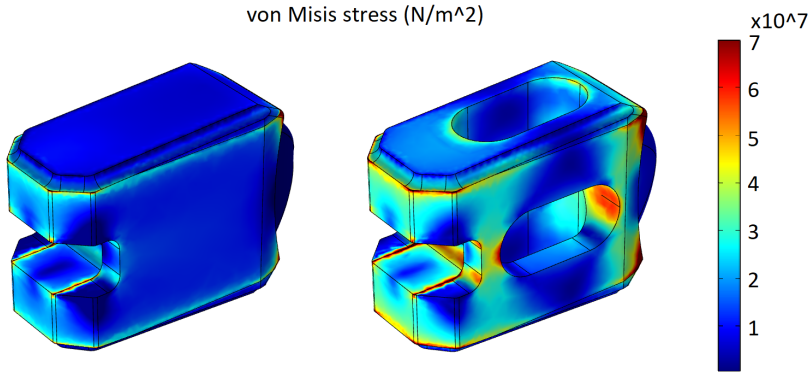

Figure 5.20: Simulated compression test of the porous part of the spinal cage using COMSOL.

Finally, 11 new design are tested and compared to find the optimal tip, back, edge and porous base. In Figure 5.21 three new designs and the original design are shown to provide a better understanding how the different designs affect the stress concentrations in the spinal cage. Combining all the knowledge gathered during the simulations one spinal cage design is chosen to provide as the base implant for the patient specific designs. This implant can be seen in Figure 5.21 as the third spinal cage.

5.3. PLIF simulations

COMSOL is used to simulate the stress in the material using a variable load and porosity. This load is also used to determine the fatigue life of the material. The spinal cage consists of solid material and porous material which both have different yield strengths. For the fatigue life of the implant only the porous material is taken into account and the fatigue life should be at least 5 million cycles.

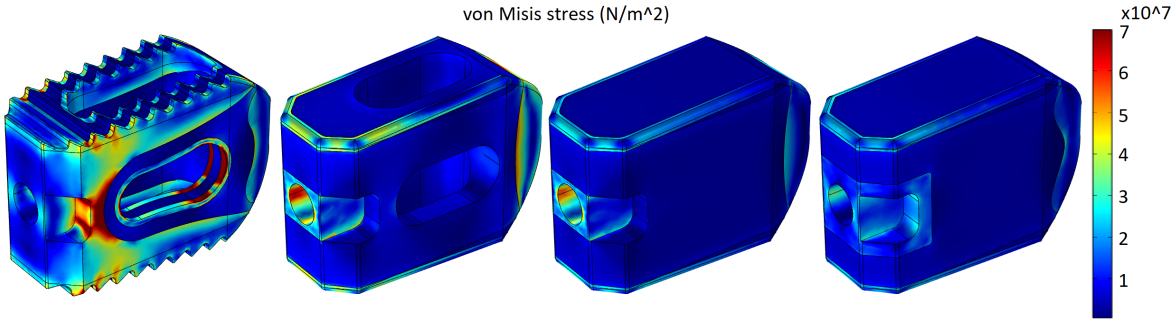

Figure 5.21: Simulated compression test of the spinal cage using COMSOL.

5.3.1. Quasi-static compression tests

Quasi-static compression tests are performed and the maximum von Mises stress is obtained from the porous and solid parts of the implant. In Figure 5.22 the applied load used is 2000 N and different porosities are used. For every porosity the maximum von Mises stress is plotted and by finding where the maximum von Mises stress intersects the yield stress, the maximum porosity can be found. It can be seen that the lower the relative density (which means a higher porosity), the more likely the material will fail.

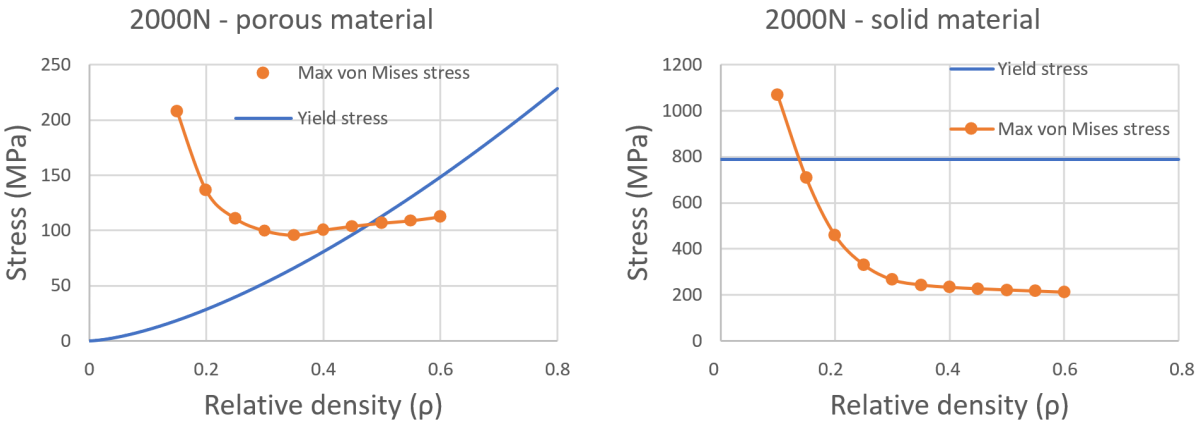

Figure 5.22: Maximum von Mises stress at different relative densities loaded with 2000 N.

This process is repeated for two more quasi-static compressive loads. For the next load, which is shown in Figure 5.23, a load of 1000 N is used. It can be seen that the point where the maximum von Mises stress crosses the yield strength of the material is at a lower relative density. The lower relative density results in a higher porosity and fewer material present in the porous part. It was expected that with a lower load a lower relative density is needed. Finally, this processes is repeated for a load of 900 N and the results are shown in Figure 5.24. An overview of the results is given in Table 5.7.

5.3.2. Fatigue properties

For every group a unique combination of a quasi-static compressive load and a cyclic load was taken. To find the relative density where, under a specific load, the fatigue life is a least 5 million cycles is investigated. 5 million cycles is taken, because this is one of the requirements the spinal cage needs to meet. These tests are performed under three different loads *i.e.* 600 N, 375 N and 350 N. After each simulations the minimal amount of cycles until failure in the porous material is gathered and plotted in the graphs shown in Figure 5.25.

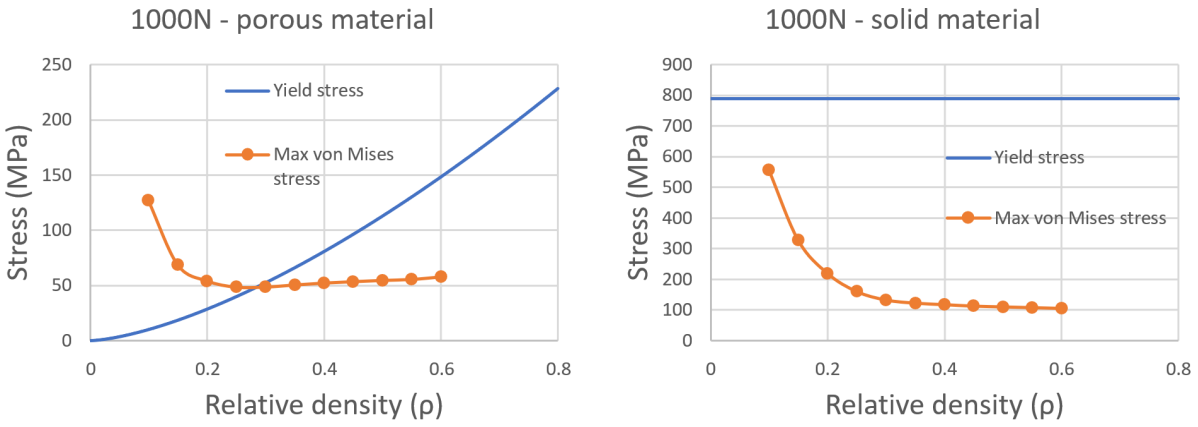

Figure 5.23: Maximum von Mises stress at different relative densities loaded with 1000 N.

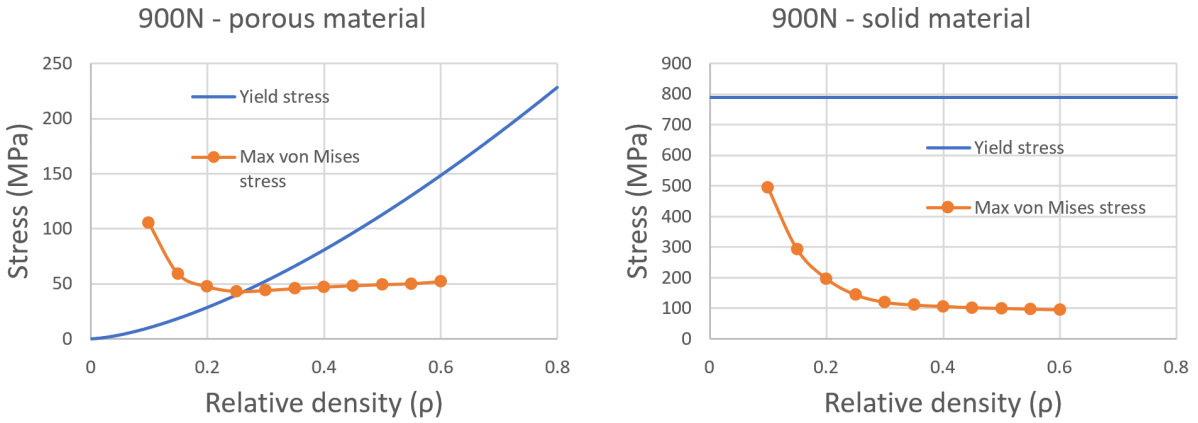

Figure 5.24: Maximum von Mises stress at different relative densities loaded with 900 N.

The same trend can be observed in these graphs compared with the quasi-static compressive tests, where the relative density needed to achieve a fatigue life of at least 5 million cycles decreases with a decreasing load.

5.3.3. Group specific porosity

The data from the simulations can be used to find the porosity range for the five different patient groups. To find this porosity range for each group three different graphs have to be investigated. When looking, for example, at group 1 it can be found that the maximum von Mises stress intersects the yield stress at a relative density of 0.48 in the porous material and 0.14 in the solid material. This means that for a relative density between 0.48 and 1, the porous material will not yield; and that for a relative density between 0.14 and 1, the solid material will not yield. Looking at the fatigue life, a fatigue life of at least 5 million cycles was found with a relative density between 0.36 and 1. The relation between the porosity and relative density is give in the following formula:

$$relative\ density = \frac{porosity}{100\%}. \tag{5.3}$$

For group 1 this results in porosity ranges of 0 - 52% for the porous material, 0 - 86% for the solid material and 0 - 64% for the fatigue life. It can now be seen that when increasing the porosity for group 1 the porous material under compression will fail first and the maximum porosity, which can be used for this group is 52%. This process is repeated for all groups and

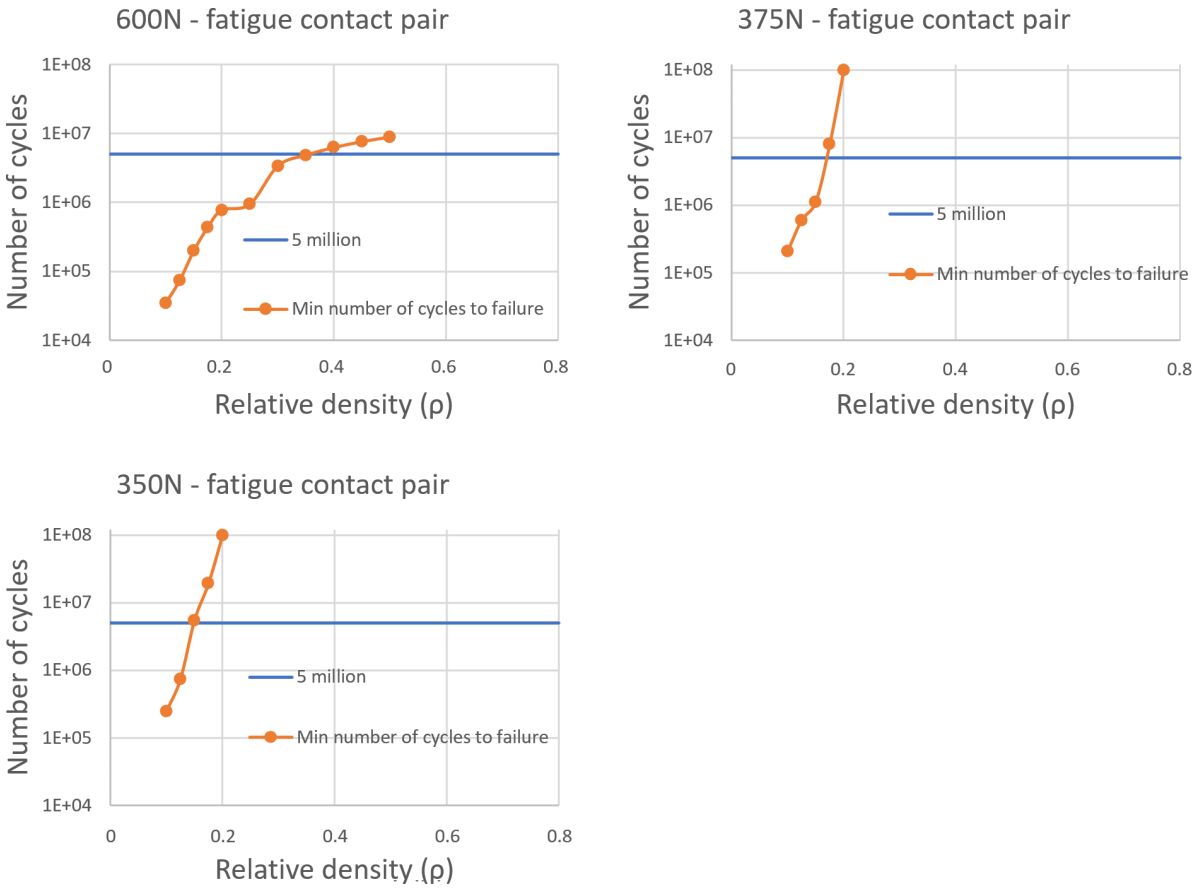

Figure 5.25: Minimum number of cycles until failure for different relative densities and loads.

the resulting porosity ranges can be seen in Table 5.7.

Table 5.7: Group specific porosity range for the PLIF spinal cage.

	Porous material	Solid material	Fatigue life porous material	Porosity range
Group 1 2000N & 600N	0 - 52%	0 - 86%	0 - 64%	0 - 52%
Group 2 2000N & 375N	0 - 52%	0 - 86%	0 - 83%	0 - 52%
Group 3 1000N & 600N	0 - 72%	-	0 - 64%	0 - 64%
Group 4 1000N & 375N	0 - 72%	-	0 - 83%	0 - 72%
Group 5 900N & 350N	0 - 74%	-	0 - 85%	0 - 74%

5.3.4. Group specific apparent Young's modulus

The main objective of testing different patient specific groups is to reduce the apparent Young's modulus to more closely resemble the Young's modulus of the vertebrae. The Young's modulus of a lumbar vertebrae is estimated to be between 400 and 700 MPa. When the apparent

Young's modulus of the implant is closer to the Young's modulus of the bone, the effect of stress shielding is reduced and osseointegration is improved [41]. For each group a maximum porosity is found and simulations are repeated with this porosity. The apparent Young's modulus of each group is calculated using the measured displacement, surface area and the applied load, and shown in Table 5.8.

Table 5.8: Group specific apparent Young's modulus for the PLIF spinal cage.

	Maximum porosity	apparent Young's modulus
Group 1 2000N & 600N	52%	3.17 GPa
Group 2 2000N & 375N	52%	3.17 GPa
Group 3 1000N & 600N	64%	2.19 GPa
Group 4 1000N & 375N	72%	1.63 GPa
Group 5 900N & 350N	74%	1.40 GPa

It can be seen that using patient specific groups can drastically reduce the apparent Young's modulus of the implant. Normally an implant will be designed to be used by (almost) every patient, which in this case would mean an implant with a apparent Young's modulus of 3.17 MPa. However, using patient groups, someone who would be in group 5 would get an implant with an apparent Young's modulus of 1.40 GPa instead of 3.17 GPa. This is a reduction of 56% and comparing this to the Young's modulus of the vertebra it is only twice as high instead of 4.5 times as high. The reduction of the Young's modulus mismatch is desired, because it will decrease the development of subsidence which can severely damage the surrounding bone and it will decrease the amount of stress shielding which can result in bone resorption. Finally Sturm et al. [94] found the ideal Young's modulus mismatch to stimulate bone growth is 5%. This is the ultimate goal to achieve for an optimal spinal fusion.

5.4. 3D printed PLIF spinal cages: experimental testing

In this chapter the mechanical properties of the new PLIF design are compared to the original PLIF design. Both spinal cages are produced using the same production process, but in different batches.

5.4.1. Microstructural and morphological characteristics

Looking at Figure 5.26 it can be observed that the strut thickness of the spinal cage are similar compared to the strut thicknesses found in the cylindrical samples.

The spinal cages did not undergo any post processing after 3D printing. Also the same design and printing process is used for the porous material compared to the cylindrical sample from earlier experiments. It is therefore expected that the internal porosity, and strut thickness of the porous part of the spinal cage is similar to the as-processed cylindrical samples. In Table 5.9 below it can be seen the Z-value for the spinal cage is below 1.96 meaning no significant difference is found.

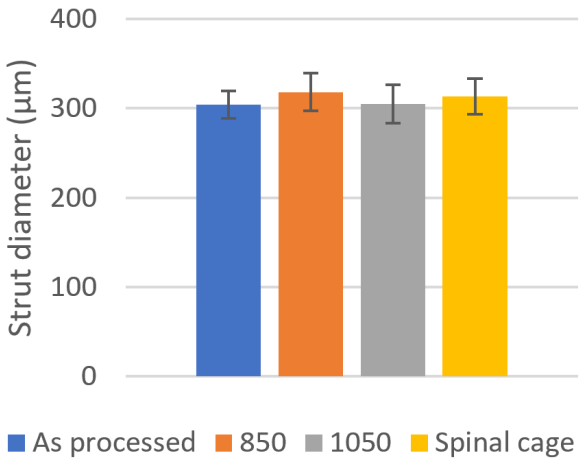

Figure 5.26: Average strut size for the three cylindrical samples, which were as-processed and heat treated at either 850 or 1050 °C, and the strut size of the spinal cage, shown in yellow.

Table 5.9: Z-score and p-value of the measured strut thickness for AP, V850, V1050 samples and the spinal cage.

	Z-score	p-value
AP	1.72	0.085
V850	2.29	0.022
V1050	1.55	0.121
Spinal cage	0.90	0.368

5.4.2. Quasi-static compression tests

In Figure 5.27 the PLIF samples are shown after a quasi-static compression test. It can be seen that the compression test was not a stable process because the resulting angle between the top an bottom of the the implant was random after every test. This is because the top plate used during compression is connected to the machine using a ball-socket joint, which is able to move in these angles. The first picture in Figure 5.27 is a sample before compression and the other pictures are of samples after compression. No sudden failure was detected during the compression test. The sample failed layer by layer slowly compressing the porous material. This was very similar to the results during the compression tests on the porous cylindrical samples.

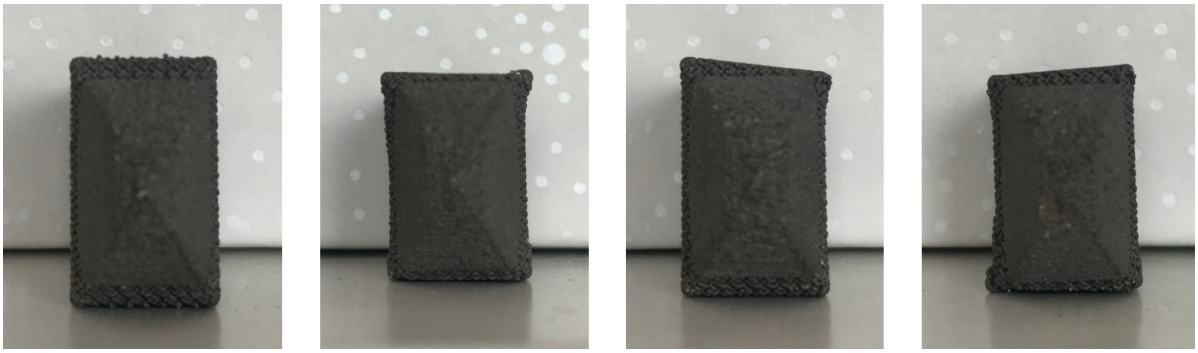

Figure 5.27: Front view of tested spinal cages using a quasi-static compression test and an original sample before compression at the left for reference.

One other type of failure which was detected is shown in Figure 5.28 where in the top right corner of the picture the solid edge is separated from the porous material. This is an area where high stress concentrations can be expected, and in combination with a high levels of deformation in the direction of H1 (see Figure 5.29), such failure can be explained. This type of failure was detected in only one of the six samples tested.

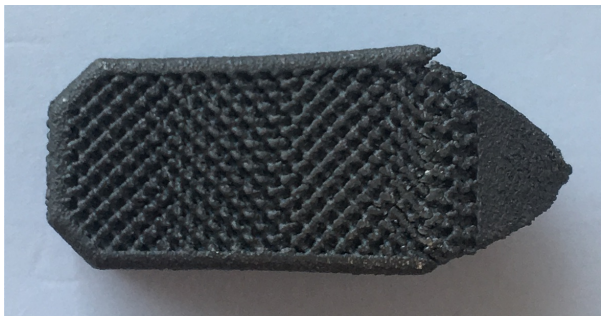

Figure 5.28: Top view of a tested spinal cage using a quasi-static compression test.

In Table 5.10 the width, length and the height at two places are measured for the design in SolidWorks, the PLIF samples after 3D printing and the PLIF samples after the compression test. In Figure 5.29 the location of these measurements are shown.

Table 5.10: Measurements of the spinal cages after 3D printing and after quasi-static compression tests.

	Height 1 (mm)	**Height 2 (mm)**	**Width (mm)**	**Length (mm)**
SolidWorks	15	13.33	9	23
3D printed spinal cage	15.06 $\pm$ 0.04	13.28 $\pm$ 0.05	8.99 $\pm$ 0.02	23.45 $\pm$ 0.05
After compression	14.03 $\pm$ 0.41	13.29 $\pm$ 0.02	9.45 $\pm$ 0.25	23.48 $\pm$ 0.08

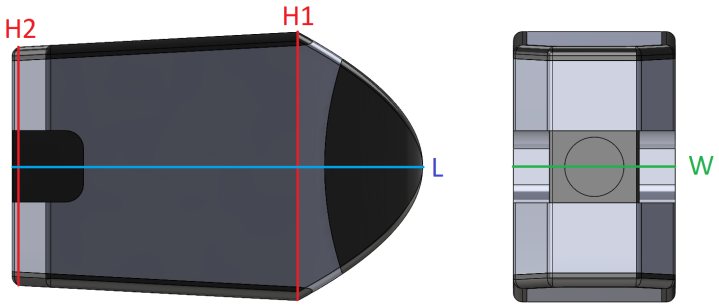

Figure 5.29: Side and back view of the spinal cage model in SolidWorks.

From Table 5.10 it can be seen that after compression there was little to no change in the height of the samples at location 2 and the length of the samples. Most of the deformation observed is the reduction in height at location 1 and the increase in the sample width. Looking at the side view on the left picture of Figure 5.29 the top and bottom of the implant are designed to have an angle of 6° relative to each other. After visual inspection of the samples it was noticed that this angle was reduced towards a more parallel position. This was due to more compressive strain in H1 compared to H2, which could be explained by the fact that less solid material is present in H1, meaning more compressive strain of the weaker porous material can take place.

In Figure 5.30 the stress-strain curves of the six tested samples are shown. Using these curves the apparent Young's modulus and the yield stress can be obtained. As shown the curves of each sample shows a different ultimate tensile strength and strain, which can be ascribed to the unstable failure as shown in Figure 5.27.

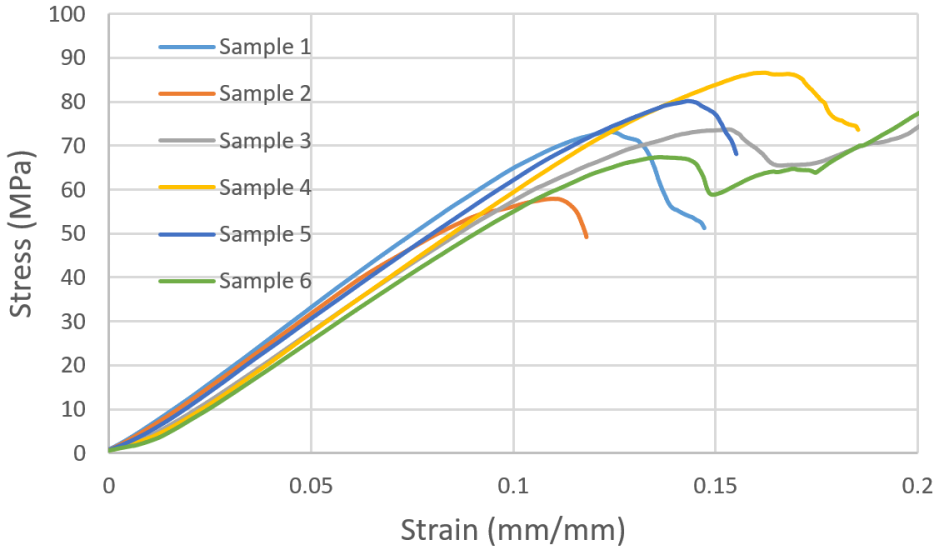

Figure 5.30: Stress-strain curve obtained after quasi-static compression tests of the spinal cages.

The stress-strain curves shown in Figure 5.30 also include the deformation of the set-up. The stiffness of the set-up was measured before the samples were tested and was found to be 14684 $\pm$ 30 N/mm. The stiffness of the tested samples including the stiffness of the machine was 10782 $\pm$ 269 N/mm. Knowing this information, the height and surface area of the sample the apparent Young's modulus can be calculated which is found to be 2.46 $\pm$ 0.22 GPa. The yield stress found for the new design is 65.1 $\pm$ 6.8 MPa.

Comparing this with the apparent Young's modulus of the original design, which was 10.03 $\pm$ 2.07 GPa, this is a large improvement. However, the yield stress found for the new design is 65.1 $\pm$ 6.8 MPa, which is lower compared to the yield stress of the original design of 123.3 MPa $\pm$ 4.8 MPa. In the literature it is advised to produce a spinal cage which will not yield when a force of 4 kN is applied [28][47]. The yield stress of 65.1 $\pm$ 6.8 MPa translates to a force 12.9 $\pm$ 1.4 kN, so the reduction in yield strength is not a problem in this case.

5.4.3. Fatigue properties

In Figure 5.31 9 different samples are shown after fatigue testing. The testing procedure of the samples is similar except for the applied load. The test is stopped after a displacement of 4 mm is reached. It is not possible to see where fatigue failure is initiated from these pictures, but it can be seen that most of the cracks are connected to a solid-porous interface.

Figure 5.32 displays the cross-head displacement against the number of cycles. In this curve it can be seen that critical failure initiates at around 750,000 cycles. This value will be used as the number of cycles until failure.

Finally, in Figure 5.33 the fatigue graph created using the fatigue tests is displayed as 'new spinal cage' and is compared to the fatigue graph of the original spinal cage called 'old spinal cage'. Comparing the fatigue graph of the different implants, it can be seen that the fatigue life of the new design is significantly improved compared to the fatigue life of the original implant. For the same fatigue life (number of cycles until failure) the new spinal cage requires a much higher force in order to fail. The fatigue life is improved by about 70% compared to the original

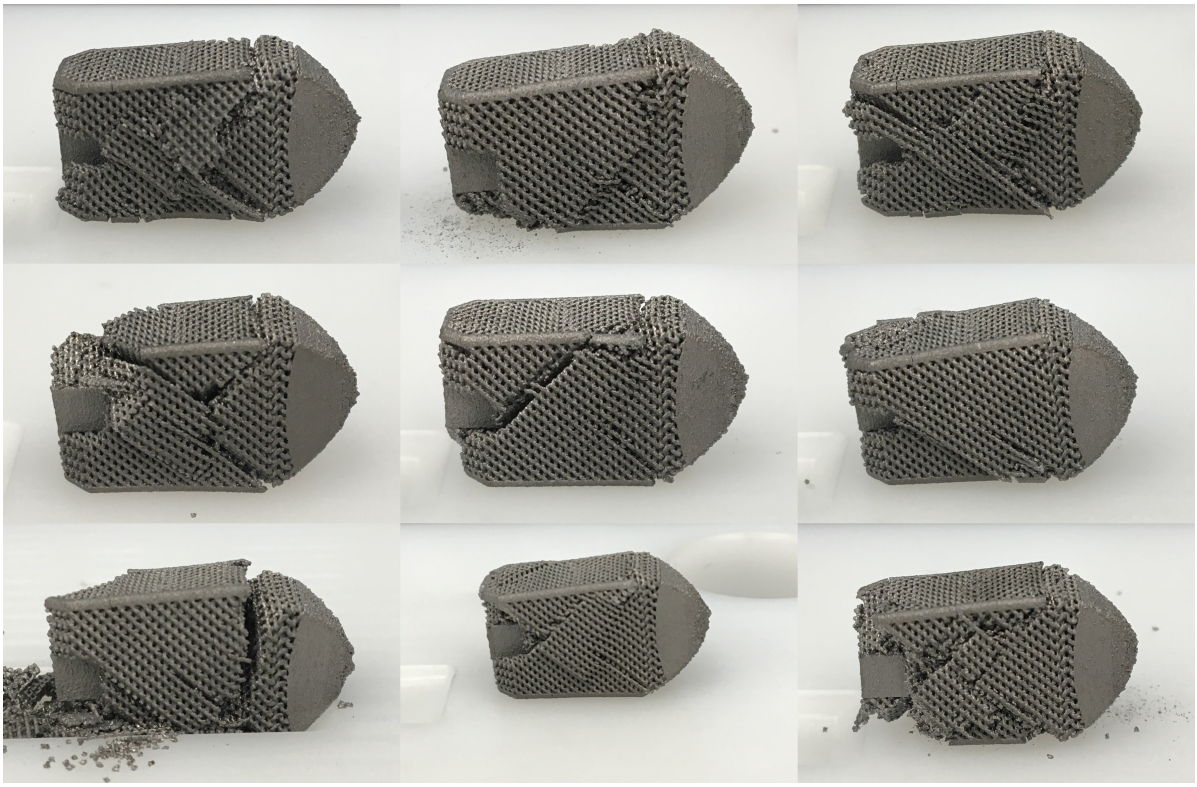

Figure 5.31: Spinal cages after fatigue tests.

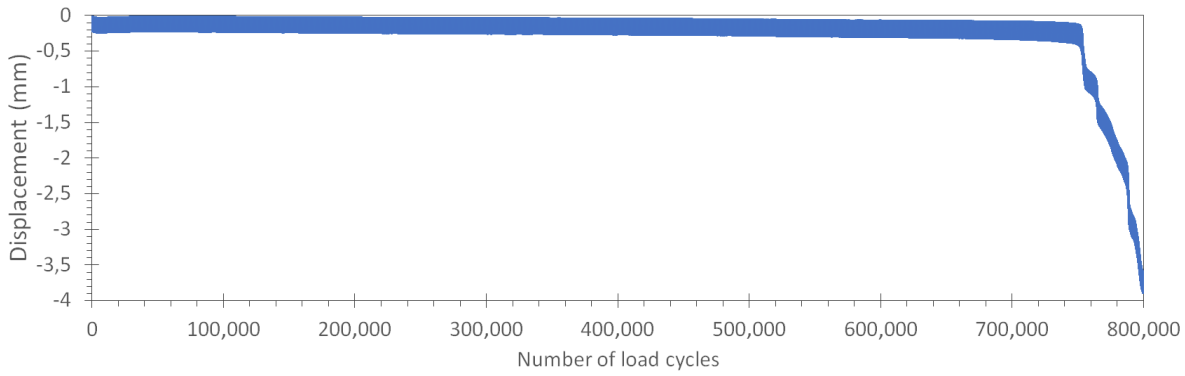

Figure 5.32: Cross-head displacement during a fatigue test on a spinal cage.

implant.

Usually a decrease in strength will result in a decrease in fatigue life. The reason why this is not the case is the change of the design, where the original design consisted of a lot more solid material. This caused the load to transfer through the solid material increasing the strength of the implant, but because of the large amount of porous-solid interfaces and the complex shapes, the fatigue life of the porous material is reduced. When looking at the failure of the original design the porous material fails first. The failure of the new design also seems to originate from the solid-porous interfaces, but because the amount of complex shapes and solid-porous interfaces is reduced the stress concentration also reduces, improving the fatigue life of the implant. The ASTM-F2077 standard advises to produce a spinal cage which survives 5,000,000 cycles under a load of 1200 N. Both spinal cages are not tested until 5,000,000 cycles, but are expected to survive 5,000,000 cycles under a load of 1200 N when extrapolating

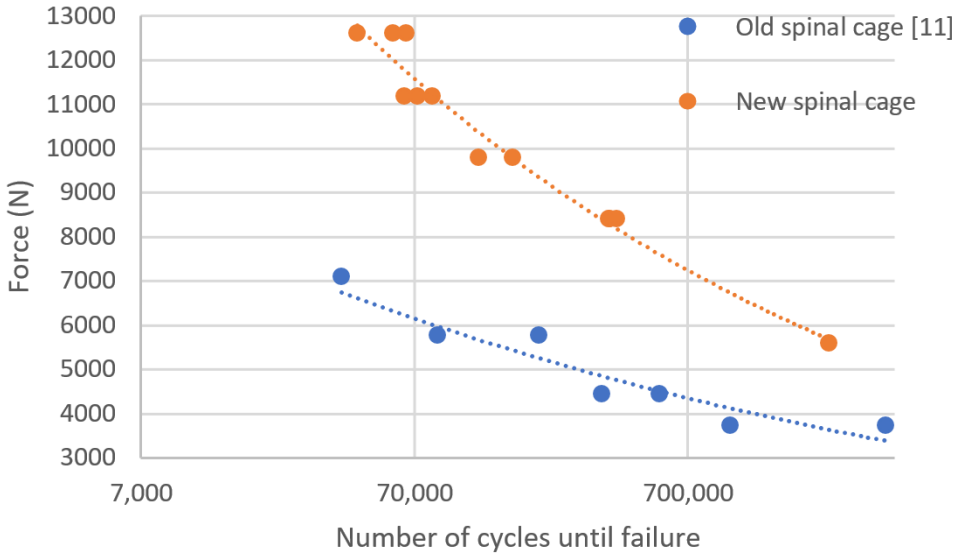

Figure 5.33: Fatigue curve of the original (data obtained from [11]) and newly designed spinal cage.

the curves in Figure 5.33. In Figure 5.34 the comparison between the old and the new spinal cage is made again, but this time the the force is normalised using the yield stress. This results in a even bigger difference between the spinal cages because the yield strength of the new spinal cage was found to be lower. The fatigue life was found to be 120% improved compared to the original spinal cage.

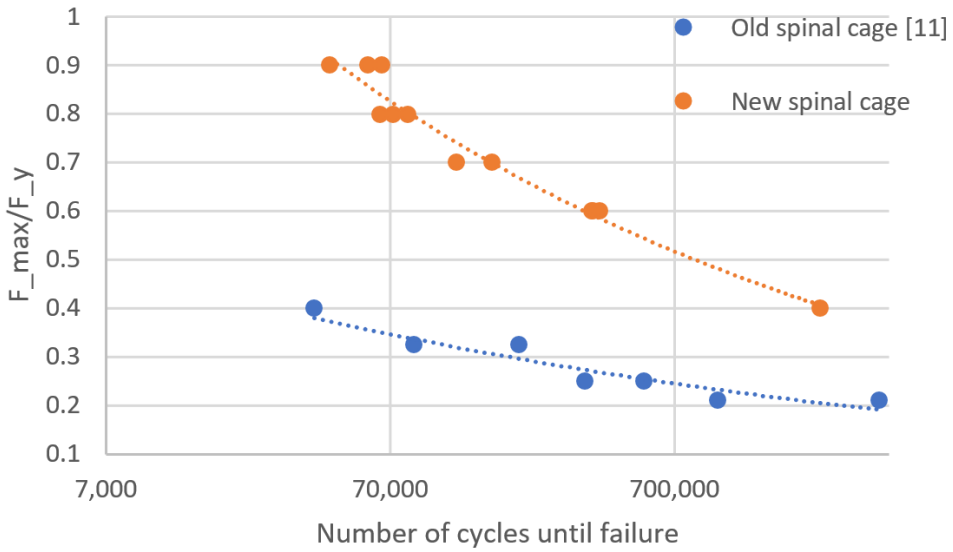

Figure 5.34: Fatigue curve of the original (data obtained from [11]) and newly designed spinal cage.

5.4.4. Simulations versus test data

The main purpose of the mechanical tests is to validate the simulations and because some data is available on the original spinal cage, simulations are also performed using the original spinal cage to improve the validation. The original spinal cage is simulated with a porosity of 63% which is also the expected porosity of the original spinal cage tested. The apparent Young's modulus found using the simulations is 21.72 GPa which is quite a lot higher compared to the measured apparent Young's modulus of 10.03 $\pm$ 2.07 GPa. The fatigue graph found

using the simulation displays a fatigue life of about 5 times lower compared to the fatigue life found using the mechanical fatigue tests which can be seen in Figure 5.35.

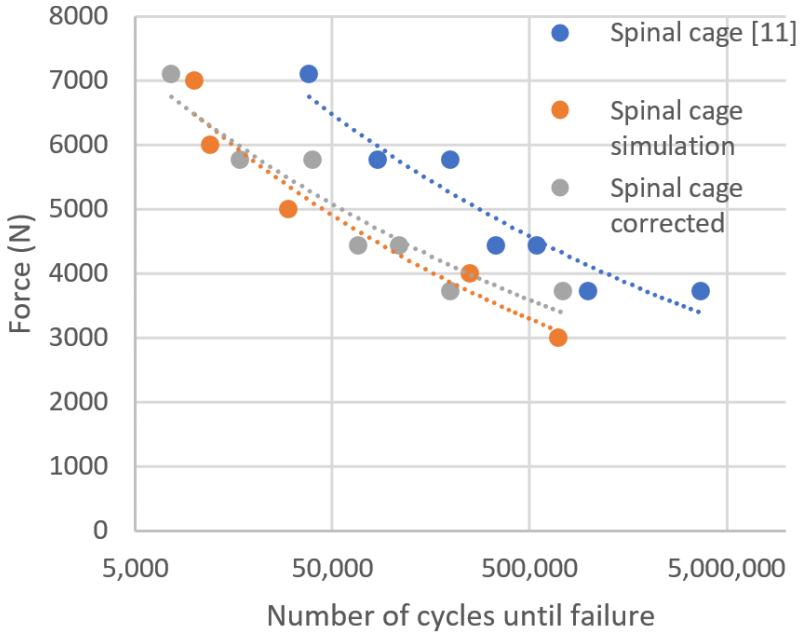

Figure 5.35: Fatigue curves of the original spinal cages, the corrected original spinal cage and the simulation of the original spinal cage, data obtained from [11].

The number of cycles until failure is measured when one of the end-of-test criteria is met, which was in this case after complete destruction of the implant. In Figure 5.36 it can be seen that the original spinal cage already failed at 1 million cycles instead of 5 million cycles. When correcting the data by reducing it five times the simulated data closely resembles the corrected data which can be seen in Figure 5.35.

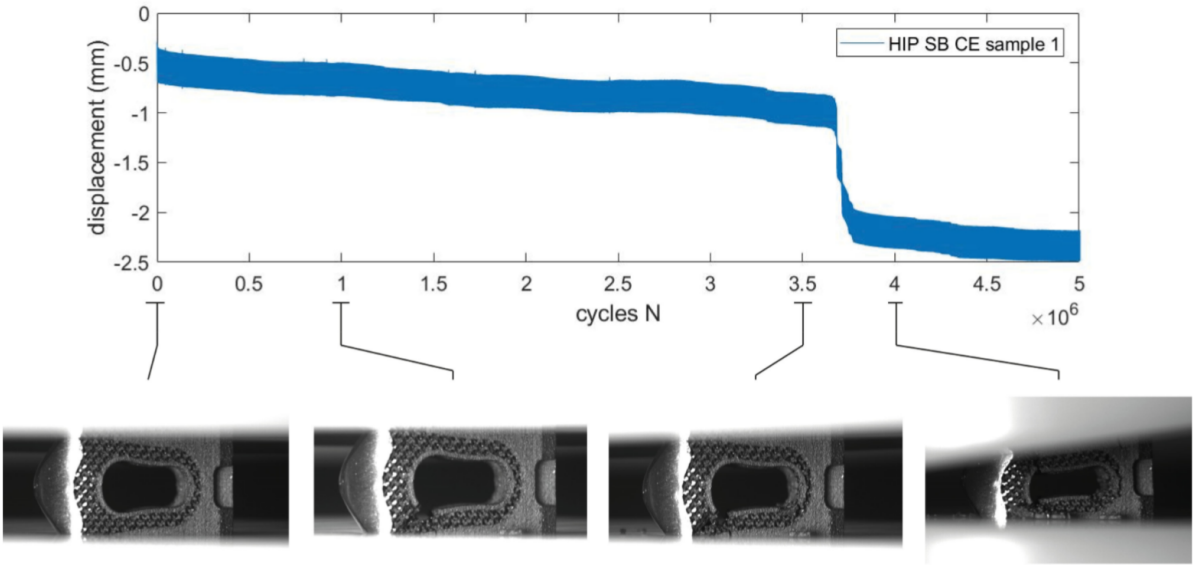

Figure 5.36: Cross-head displacement during a fatigue test on a spinal cage including time lapse [11].

This process is repeated with the new spinal cage. The simulated apparent Young's modulus found is 2.615 GPa which only differs 6.3% form the experimentally measured apparent

Young's modulus of 2.46 $\pm$ 0.22 GPa. The comparison of fatigue graph is shown in Figure 5.37, where the number of cycles of failure of the simulated implants is about 3 times lower compared to the mechanically fatigue tested samples.

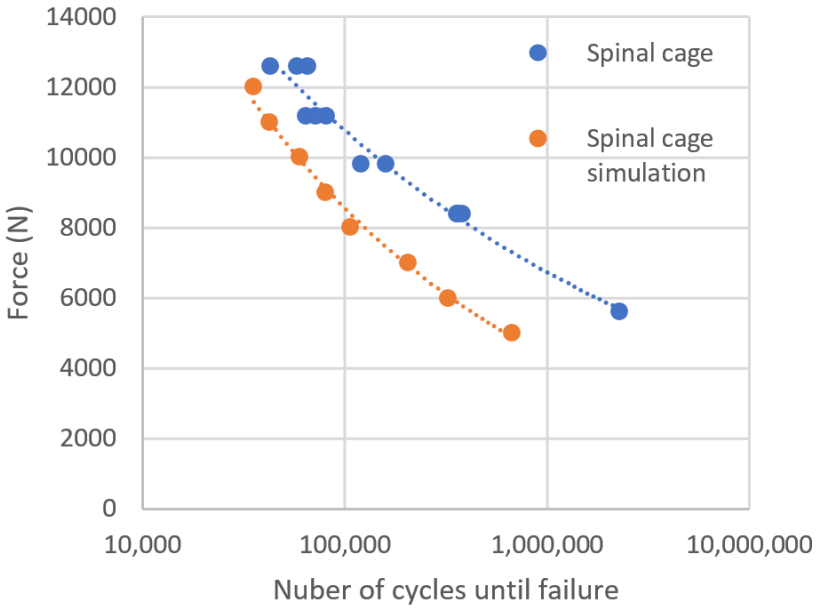

Figure 5.37: Fatigue curves of the new spinal cage and the simulations of the new spinal cage.

Apart from comparing data a visual inspection is also performed. Figure 5.38 shows at which location failure is initiated using the simulations. Comparing this to fatigue failure seen in Figure 5.31 it can be seen that most cracks are connected to one of these three failure sites.

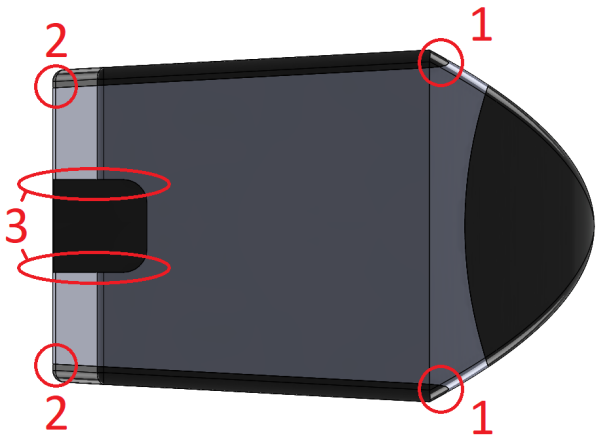

Figure 5.38: SolidWorks image showing at which locations failure initiated using COMSOL simulations.

After comparing both spinal cages with the simulations it can be seen that the simulations resemble the mechanical test, but there is still an error present. The new design resembles the simulations more closely, which is probably due to the reduced complexity of the design.

To make the simulations more reliable the data should be altered to match the mechanical data. For the new design this means reducing the apparent Young's modulus by 6.3% and increasing the fatigue life 3 times. Increasing the fatigue life 3 times sounds like a lot, but due to the exponential shape of the fatigue curve this effect is reduced. The new porosity ranges for an increase fatigue life are given in Table 5.11. It can be seen that the fatigue life is affected

quite a bit at a load of 600 N

Table 5.11: Corrected porosity range for fatigue simulations.

Cyclic load	Old porosity range	Corrected porosity range
600 N	0 - 64%	0 - 70%
375 N	0 - 83%	0 - 84%
350 N	0 - 85%	0 - 86%

In Table 5.12 it can be seen that only the porosity range of group 3 is affected by the change of the fatigue life. Also in Table 5.12 the corrected apparent Young's modulus is given.

Table 5.12: Group specific porosity range, corrected porosity range, apparent Young's modulus and the corrected apparent Young's modulus.

	Maximum Porosity	Maximum Corrected porosity	Apparent Young's modulus	Corrected apparent Young's modulus
Group 1 2000N & 600N	52%	52%	3.17 GPa	2.98 GPa
Group 2 2000N & 375N	52%	52%	3.17 GPa	2.98 GPa
Group 3 1000N & 600N	64%	70%	2.19 GPa	1.81 GPa
Group 4 1000N & 375N	72%	72%	1.63 GPa	1.53 GPa
Group 5 900N & 350N	74%	74%	1.40 GPa	1.32 GPa

Every spinal cage after 3D printing will not have exactly the same porosity. The corrected apparent Young's modulus is now calculated for the maximum porosity possible. If this porosity is too high after 3D printing the spinal cage is in danger of premature failure and can not be used. If the implant is printed at the maximum porosity it is expected 50% of the spinal cages will be rejected due to exceeding the porosity limit. To prevent this it is advised to add a confidence interval (CI) to the spinal cage. The standard deviation found when measuring the porosity of the 3D printed spinal cage was about 1%. When subtracting 2 times the standard deviation form the maximum porosity it will be expected that 97.7% of the spinal cages will not exceed the maximum porosity and can be approved for use. This reduction in porosity will cause an increase in the apparent Young's modulus which can be seen in Table 5.13.

A simulation will never be perfect, since it always involves making assumptions and considering the trade off between precision and computational power. In this case the first choice to make is which material properties to use. During mechanical testing the spinal cage will be placed between stainless steel plates for quasi-static compression tests and between POM for the fatigue tests. However, for the intended use of spinal fusion the spinal cage is placed between two vertebrae. For the simulation it is chosen to create a model based on the mechanical tests for two reasons: to give the opportunity to validate the simulation using these mechanical tests and because it is very hard to accurately simulate bone. The Young's modulus of bone will be different depending on direction, location, force and loading speed making

Table 5.13: Group specific apparent Young's modulus for the PLIF spinal cage.

	Max porosity + CI	apparent Young's modulus
Group 1 2000N & 600N	50%	3.13 GPa
Group 2 2000N & 375N	50%	3.13 GPa
Group 3 1000N & 600N	68%	2.00 GPa
Group 4 1000N & 375N	70%	1.81 GPa
Group 5 900N & 350N	72%	1.53 GPa

it almost impossible to simulate accurately. The simulated stainless steel and POM blocks are not expected to have a large effect on reducing the accuracy of the simulation due to the solid structure of the material and the basic design of the blocks.

The material used for the spinal cage is SLM 3D printed Ti6Al4V. The mechanical properties of this material depend on the 3D printing parameters. When altering the parameters, it is important to perform mechanical tests and use the properties found as input values for the simulations, as was done in this research. However, the spinal cage has a complex lattice structure. Although it is possible to simulate a complex lattice structure, it will significantly increase the amount of computational power needed in order to perform the simulation, up to the point where it can take days or weeks. Fortunately, Ahmadi et al. [2] found a solution to this problem by producing formulas which can be used to simulate the complex lattice structure as a solid, as discussed in Section 4.2.3. However, there are a few disadvantages when using these formulas: the formulas only seem to be accurate when working with porosities between 50% and 90%; the mechanical properties of the material are highly dependent on the production process; and the formulas only work for a diamond lattice structure. Fortunately, the production process used in this research is equal to the production process used to generate the formulas, although there is a small error found between the formulas and the cylindrical samples tested. This difference was used to correct the formulas to get a more accurate result. Since the correction took place by using samples with a porosity of 59%, it is expected that the simulations with a porosity of 59% are most accurate and the error will increase when moving away from this value. The porosity ranges used for the simulations are between 40% and 90% and it is expected that the values at porosities between 40% and 50% have a larger error because the formulas are not very accurate anymore in that porosity range.

The simulation is modelled based on the set-up used for the mechanical tests. Although, the simulation mimics the mechanical test, there are some noteworthy differences, which could affect the accuracy of the simulations. The lower block is fixated at the bottom, a force is applied on the top of the upper block and the blocks only have one degree of freedom, which is similar to the set-up used for the fatigue tests. However, for the compression test the top block is able to rotate when the spinal cage is deforming, which is different compared to the simulation. When the top block is fixed during compression the implant will be deformed equally across the length of the implant. When the upper block is able to rotate the contact area between the upper block and the implant is able to shift when yielding is initiated due to the rotation. This shift will happen towards the weakest part of the spinal cage, which will result in

accelerated failure. The friction between the sample and the blocks will cause strains around the contact points during the mechanical tests. For the simulation this will be different as there is no friction between the materials. This will lead to additional compression forces at the lowest and top corners of the implant instead of the shear stress at the contact area. These forces are expected to reduce the fatigue life of the simulated implant at these corners.

To simulate the implant COMSOL generates a mesh consisting of dots connected with rods creating many triangles. The minimum size of the triangles will determine how accurately the spinal cage is simulated. The smaller the size the more accurate, but this will also increase the computation time. A mesh study was performed to find when a reduction in mesh size stopped significantly changing the outcome of the simulation. Due to this mesh study it is expected that the limited mesh size will not have a large negative effect on the outcome of the simulation.

The simulations are used to find three specific data points for each patient specific group when a fixed load is applied. These three data points are: at which porosity the porous material starts to yield; at which porosity the solid material starts to yield; and finally at which porosity fatigue failure in the porous material is initiated. From these three points the lowest porosity is taken for that patient specific group to prevent failure. In Figures 5.22, 5.23, 5.24 and 5.25 several graphs are plotted to find these points. However, there is one big problem with the accuracy of these graphs. The model does not consider plastic deformation, strain hardening and failure. During mechanical loading high stress concentrations are created in the sample and when the load is increased this can lead to plastic deformation. The yielding will strengthen the material due to strain hardening, but it can also cause stress relief due to the deformation, shifting the highest stress concentration to another part of the implant. Since this will not happen in the simulation, the stress concentration keeps increasing at a specific location, influencing the stress in the surrounding material, making the simulation less accurate.

During the mechanical fatigue tests the strut with the highest stress concentrations will fail first, which removes the stress concentration found at that location. This will redistribute the stress in the sample and when continuing the fatigue test the strut where now the new highest stress concentration is found will fail and this process will continue until the whole sample fails. Because no fracture occurs during the simulation, no stress redistribution will take place, which results in a different progression of failure. Using this information it can be concluded that the graphs produced in Figures 5.22, 5.23, 5.24 and 5.25 are expected to be reliable below the yield strength or before fatigue failure. When exceeding the yield strength or continuing the fatigue life measurement after initial failure the error is expected to increase. It is also important to know that the solid and porous material will influence each other, so if one of those starts to yield or fail, it will make the data from the other also unreliable from that point onward.

When comparing the Young's modulus found during the simulations with the Young's modulus found using mechanical testing, some noticeable differences are found. The simulated Young's modulus of the original spinal cage is 21.72 GPa and from the mechanical tests a Young's modulus of 10.03 ± 2.07 GPa was found by A. Blok [11]. The error of the simulated Young's modulus is very high and can be explained by the highly complex spinal cage design used. Due to the complex structure the mesh is expected to have a low accuracy. As shown in Figure 5.39 this can result in lower strains measured compared to the actual strains. The strain is used to calculate the Young's modulus and a lower strain results in a higher Young's modulus.

Furthermore, as discussed before the upper block is able to rotate during the compression test. This makes it possible to have a larger amount of strain in a part of the implant where the stiffness is lower. As only the cross-head displacement is measured, no distinction can

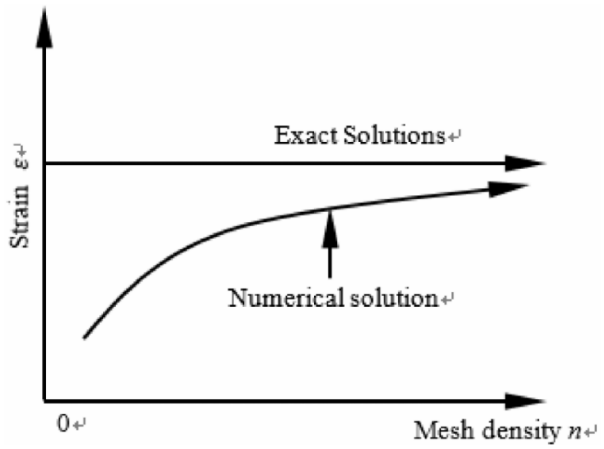

Figure 5.39: Relations between the accuracy of strain and mesh density [115].

be made between different 'stiffnesses' across the spinal cage. This could lead to measuring a lower apparent Young's modulus compared to using a fixed upper block such as in the simulations. Since the simulations does not consider plastic deformation, strain hardening and failure, no stress relieve can take place. Stress relieve can result in a reduction of the stiffness at that location, which can result in a lower measured apparent Young's modulus compared to the simulation. Comparing the Young's modulus of the new design (2.46 ± 0.22 GPa) with the simulated Young's modulus (2.62 GPa) only a difference of 6.3% is observed. Still, the Young's modulus is higher compared to the actual Young's modulus, but the error is greatly reduced. This is expected due to the largely simplified design.

In Figure 5.35 it can be observed that the fatigue graph found for the simulated original spinal cage is about 5 times lower compared to the fatigue life found during the mechanical tests. This can be partly explained by how fatigue failure is determined. For the simulated data the fatigue life is taken when fatigue failure is initiated. However, for the mechanical test the fatigue life is measured after 4 mm cross-head displacement, which is reached after extensive fatigue failure. To get a more accurate comparison it is advised to measure the number of cycles during the mechanical fatigue test when fatigue failure initiates. As discussed the simulation will lose its accuracy after initial failure because no fracture will take place during the simulation. This is the reason why it is not advised to use the simulation to measure extensive fatigue failure. Fortunately, A. Blok [11] produced a time laps which can be used to estimate the time of initial failure. From the time laps in Figure 5.36 it can be seen that fatigue failure is initiated 5 times earlier compared to the 4 mm cross-head displacement. Correcting the fatigue data by a factor 5 results in a fatigue graph very similar to the fatigue graph found using the simulation as shown in Figure 5.35.

Comparing the fatigue graphs of the new spinal cage, it can be seen that the fatigue life of the simulated data is about three times lower compared to the mechanical data. The same problem is present here compared to the old spinal cage where not the fatigue failure initiation is measured but a cross-head displacement of 4 mm. A time lapse was produced to find the point of failure initiation during the mechanical tests, but it was not possible to find an accurate estimation. Looking at Figure 5.38 three locations are pointed out where fatigue failure is expected to initiate. However, due to the design of the POM blocks locations 1 and 2 are not visible. Moreover, if further investigation will be performed for this design it is advised to change the design of the POM blocks in order to make visual inspection of fatigue failure initiation possible.

6

Conclusions and recommendations

The conclusions of this thesis will be presented in this chapter based on the research questions which were defined in Chapter 3.

How does an alternative heat treatment without added high pressure affect the fatigue life and strength, whilst still meeting the material requirements for spinal cages?

- The α grain thickness found after vacuum heat treatment for 2 hours at 850 °C is 1.3 $\pm$ 0.4 µm and for heat treatment at 1050 °C 3.7 $\pm$ 1.1 µm.
- Ti6Al4V with a lattice structure will not deform when a vacuum heat treatment is applied, as no significant difference in internal porosity and strut thickness is found.
- Vacuum heat treating Ti6Al4V for 2 hours at 850 °C will result in an increase of 13% of the Young's modulus compared to as-processed Ti6Al4V. This is due to the transformation of 'α-martensite to an α + β microstructure where the transformation to α is prevalent. Vacuum heat treating Ti6Al4V for 2 hours at 1050 °C result in a similar β concentration which would result in a similar Young's modulus. However, the Young's modulus is increased by 5% compared to the 850 °C heat treatment. The smaller size of α grain thickness at 850 °C results in a larger concentration of grain boundaries and triple junctions where the Young's modulus is around 75% compared to the surrounding material. This could explain the lower Young's modulus found at 850 °C.
- According to the Hall-Petch relationship the yield strength of the samples heat treated at 1050 °C should be lower compared to the heat treated samples at 850 °C because of the larger α grain thickness. However, the yield strength is found to be 7% higher. This could be explained by small amounts of 'α-martensite, which can be formed when the material is cooled from 1050 °C with a cooling rate of 10 °C/min.
- The fatigue life is increased by 20% when a vacuum heat treatment is performed compared to the as-processed samples. This is due to the removal of residual stresses and the transformation of the 'α-martensite to an α + β microstructure. Between the vacuum heat treatments at 850 °C and 1050 °C no difference in fatigue life is found. The difference in α grain thickness will influence the fatigue life, but is negligible compared to the influence of surface quality and internal porosity.
- Comparing the vacuum heat treatment and HIP it can be seen that the fatigue life for HIP outperforms the fatigue life of vacuum heat treatment at low cycle fatigue. At 30,000

cycles the fatigue life of HIP is 15% better. For high cycle fatigue the difference in fatigue life is negligible and at 1,000,000 cycles the fatigue life of HIP is 1% worse. The big difference between the heat treatments is the smaller internal porosity after HIP. This internal porosity will affect the fatigue life. However, the effect of internal porosity will reduce faster compared to the effect of surface quality resulting in a similar fatigue life at high cycle fatigue.

How will design changes of the spinal cage affect stress shielding, the apparent Young's modulus, yield stress and the fatigue life?

- It was found that a completely porous cylinder outperformed the original spinal cage in terms of a higher yield stress, lower apparent Young's modulus and higher fatigue life. This resulted in the conclusion that the added solid material, which was intended to strengthen the spinal cage, in fact weakened the spinal cage due to the added stress concentration caused by the complex shapes and solid porous interfaces.
- More importantly the new spinal cage design outperformed the original spinal cage significantly when comparing the fatigue life which is increased with 70%. The apparent Young's modulus of the new spinal cage is 4 times lower compared to that of the original spinal cage. However, the yield stress of the new design is 27% lower compared to the old spinal cage, but this was determined not to be a problem since it still meets the requirements.
- The new spinal cage has to meet three main requirements: have an α + β microstructure; no yielding when a force of 4 kN is applied; and no fatigue failure after 5 million cycles at 600 N with an R-ratio of 0.1. It has been shown that an α + β microstructure can be created using a vacuum heat treatment and the yield strength found was 12.9 $\pm$ 1.4 kN. It is not possible to say if this implant will survive 5 million cycles at 600 N because this was not tested. However, when looking at the trend-line of the available data the following formula can be generated: $F = 112,461 * x^{-0.204}$ where x is the number of cycles. This would mean that at 5 million cycles the implant can survive a load of 4835 N, so surviving a load of 600 N seems plausible.

How much does creating patient specific groups change the mechanical properties of the spinal cage to improve the spinal fusion process?

- Five different patient groups are defined based on a maximum variable peak load and cyclic load. Using these requirements five different spinal cages are designed based on different porosities.
- Using FEM software the minimum apparent Young's modulus which can be achieved for every patient group is found. The apparent Young's modulus found for every group ranges between 1.40 to 3.17 GPa, which is a large difference. This will make it possible for patients to get an implant with a lower apparent Young's modulus, which will improve the spinal fusion process.
- Finally, the fatigue graph and apparent Young's modulus obtained from the mechanical tests are used to validate the simulation. The simulated fatigue life was around three times lower compared to the actual fatigue life and the apparent Young's modulus was 6.3% higher compared to the actual apparent Young's modulus. These findings are used to correct the simulations and the new apparent Young's modulus for every patient group lies between 1.32 and 2.98 GPa which is even closer to the Young's modulus of the surrounding bone. The correction of three times the fatigue life did not affect the result much because of the exponential nature of the fatigue graph.

6.1. Further recommendations

Developing and designing a spinal implant is an enormous task, and this thesis has only grasped the tip of the iceberg. Therefore, there are plenty of recommendations to be made.

Heat treatment:

- The yield stress of the samples vacuum heat treated at 1050 °C was found to be higher compared to the the samples heat treated at 850°C. This is against the Hall-Petch relationship, but is explained due to the possibility of $'\alpha$-martensite formation during cooling. It would be interesting to find out the $'\alpha$-martensite concentration in the material.
- A 20% increase in fatigue life was observed between as-processed and vacuum heat treated samples. This is due to the removal of residual stresses and the transformation of $'\alpha$-martensite to $\alpha + \beta$. It would be interesting to test how much each of these two changes affect the fatigue life separately.
- During fatigue testing it was found that the fatigue life of vacuum heat treatment and HIP was similar at high cycle fatigue. This was explained by the reduced effect of the internal porosity on the fatigue life and a dominant effect of the surface quality. It was also observed that the fatigue life could be improved when comparing HIP to HIP + sandblasting + chemical etching. It would be interesting to see the possible fatigue life when adding these surface treatments after vacuum heat treatment and to see if the influence of internal porosity will increase at high cycle fatigue.
- Two sample groups from different batches are compared in terms of fatigue life in this report. All the data is normalised and the local stress is calculated. It was observed that the fatigue data of the as-processed samples from both batches aligned almost perfectly. However, this only compares two batches. It would be interesting to find the error between different batches, so this can be taken into account in future comparisons.

Design:

- High stress concentrations are created between the solid and the porous material. Even with the new design it could be seen that fatigue failure will initiate at the solid-porous interface. It would be interesting to look at redesigning this interface to reduce the stress concentrations and increase the fatigue life. Another option would be removing the solid-porous interface all together as it was shown that the solid material is not needed for strengthening of the spinal cage. The solid parts are needed for the implantation process, so by changing this process the solid parts can possibly be removed.
- One of the requirements of the spinal cage is no fatigue failure when applying a load of 600N for 5,000,000 cycles. As discussed the spinal cage is expected to meet this requirement, but should still be tested to validate this statement.
- 5 patient specific spinal cages are designed based on different porosities. However, mechanical tests are only performed for one porosity to validate the simulations. It would be interesting to 3D print all 5 patient specific spinal cages and mechanically test them.
- For the heat treatment a recommendation was made to apply surface treatments to vacuum heat treated samples to further improve the fatigue life. The spinal cage tested in this report did not receive any heat treatment or surface treatment and is considered as-processed. Applying these post treatments could significantly improve the fatigue life of the spinal cage.

- The current spinal cage is designed to fit between the L2 and L3 vertebra under an angle of 6°. It would be interesting to investigate the effect of changing the size, angle and location of the spinal cage to discover if this design is suitable for other situations where spinal fusion is needed.
- Test the speed of bone in-growth in the current lattice structure without allo- or autografts. Also investigate if a coating is needed to stimulate the bone growth.
- 5 patient specific groups are created based on the bone quality and lifestyle of the patients, but still a reliable method should be determined to find out which patient specific group is the most suitable for each patient.
- Perform a cadaver study to get a better image about how the implant will behave in the body. This could also provide information about possible damage to the bone from the implant and how the mechanical properties of the spinal cage will change with respect to the mechanical tests. Moreover, this test will show if the implant is fixated to the bone properly or if some movement will take place.

7

Acknowledgements

I would like to thank Dr. Jie Zhou and Dr. Vera Popovich for being my supervisors and being very involved during this project.

I would like to thank Mohamad Ahmadi, Banafsheh Sajadi and especially Pim Pellikaan from Amber Implants for their collaboration during this project.

I would like to thank Dr. Calvin Rans for making it possible for me to test at DASML and being involved in the later stages of this project.

Finally, this research would not be possible without the help of Elise Reinton, Dave Ruijtenbeek, Ton Riemslag, Richard Huizenga, Sander van Asperen, Luis Manuel de Almeida, and Ruud Hendrikx.

Bibliography

[1] Posterior lumbar interbody fusion. https://midwestbonejoint.com/lower-back/posterior-lumbar-interbody-fusion/. Accessed: 2020-04-17.

[2] Seyed Ahmadi, Saber Yavari, Ruebn Wauthle, Behdad Pouran, Jan Schrooten, Harrie Weinans, and Amir Zadpoor. Additively manufactured open-cell porous biomaterials made from six different space-filling unit cells: The mechanical and morphological properties. *Materials*, 8(4):1871–1896, 2015.

[3] SM Ahmadi, G Campoli, S Amin Yavari, B Sajadi, Ruben Wauthlé, Jan Schrooten, H Weinans, and AA Zadpoor. Mechanical behavior of regular open-cell porous biomaterials made of diamond lattice unit cells. *Journal of the mechanical behavior of biomedical materials*, 34:106–115, 2014.

[4] SM Ahmadi, RK Ashok Kumar Jain, AA Zadpoor, C Ayas, and VA Popovich. Effects of heat treatment on microstructure and mechanical behaviour of additive manufactured porous ti6al4v. In *IOP Conference Series: Materials Science and Engineering*, volume 293, page 012009. IOP Publishing, 2017.

[5] SM Ahmadi, R Kumar, EV Borisov, R Petrov, S Leeflang, Y Li, N Tümer, R Huizenga, C Ayas, AA Zadpoor, et al. From microstructural design to surface engineering: A tailored approach for improving fatigue life of additively manufactured meta-biomaterials. *Acta biomaterialia*, 83:153–166, 2019.

[6] T Ahmed and HJ Rack. Phase transformations during cooling in α+ β titanium alloys. *Materials Science and Engineering: A*, 243(1-2):206–211, 1998.

[7] Rizwan Arshad, Lorenza Angelini, Thomas Zander, Francesca Di Puccio, Marwan El-Rich, and Hendrik Schmidt. Spinal loads and trunk muscles forces during level walking–a combined in vivo and in silico study on six subjects. *Journal of biomechanics*, 70: 113–123, 2018.

[8] Xavier Banse, TJ Sims, and AJ Bailey. Mechanical properties of adult vertebral cancellous bone: correlation with collagen intermolecular cross-links. *Journal of bone and mineral research*, 17(9):1621–1628, 2002.

[9] Ioannis Bantounas, David Dye, and Trevor C Lindley. The role of microtexture on the faceted fracture morphology in ti–6al–4v subjected to high-cycle fatigue. *Acta materialia*, 58(11):3908–3918, 2010.

[10] Arno Bisschop, Margriet G Mullender, Idsart Kingma, Timothy U Jiya, Albert J van der Veen, Jan C Roos, Jaap H van Dieën, and Barend J van Royen. The impact of bone mineral density and disc degeneration on shear strength and stiffness of the lumbar spine following laminectomy. *European Spine Journal*, 21(3):530–536, 2012.

[11] A Blok. The effects of post process treatments on biomechanical properties of additively manufactured ti6al4v metamaterials to apply as bone implants, 2019.

[12] Julius Bonini, Kaitlyn Calaluca Mazza, and Joan Morra. Cleanliness and microstructural issues related to additive layer manufactured porous surface structured titanium medical and dental implants. In *Proceedings of the 13th World Conference on Titanium*, pages 1751–1759. Wiley Online Library, 2016.

[13] Annabel Braem, Amol Chaudhari, Marcio Vivan Cardoso, Jan Schrooten, Joke Duyck, and Jozef Vleugels. Peri-and intra-implant bone response to microporous ti coatings with surface modification. *Acta biomaterialia*, 10(2):986–995, 2014.

[14] Raymond R Brodeur and L DelRe. Stiffness of the thoracolumbar spine for subjects with and without low back pain. *JNMS-BALTIMORE-*, 7(4):127–133, 1999.

[15] Alexander G Bruno, Kerry E Broe, Xiaochun Zhang, Elizabeth J Samelson, Ching-An Meng, Rajaram Manoharan, John D'Agostino, L Adrienne Cupples, Douglas P Kiel, and Mary L Bouxsein. Vertebral size, bone density, and strength in men and women matched for age and areal spine bmd. *Journal of Bone and Mineral Research*, 29(3):562–569, 2014.

[16] Fei Cao, Tiantian Zhang, Matthew A Ryder, and Diana A Lados. A review of the fatigue properties of additively manufactured ti-6al-4v. *JOM*, 70(3):349–357, 2018.

[17] E Cendre, D Mitton, J-P Roux, ME Arlot, F Duboeuf, B Burt-Pichat, C Rumelhart, G Peix, and PJ Meunier. High-resolution computed tomography for architectural characterization of human lumbar cancellous bone: relationships with histomorphometry and biomechanics. *Osteoporosis International*, 10(5):353–360, 1999.

[18] Harry K Charles Jr, Michelle H Chen, Thomas S Spisz, Thomas J Beck, Howard S Feldmesser, Thomas C Magee, and Barry P Huang. Ampdxa for precision bone loss measurements on earth and in space. *Johns Hopkins APL technical digest*, 25(3):187, 2004.

[19] Cen Chen, Ya Hao, Xue Bai, Junjie Ni, Sung-Min Chung, Fan Liu, and In-Seop Lee. 3d printed porous ti6al4v cage: Effects of additive angle on surface properties and biocompatibility; bone ingrowth in beagle tibia model. *Materials & Design*, 175:107824, 2019.

[20] Hong Chen, Dianming Jiang, Yunsheng Ou, Jian Zhong, and Fajin Lv. Geometry of thoracolumbar vertebral endplates of the human spine. *European Spine Journal*, 20 (11):1814, 2011.

[21] E Chudinova, M Surmeneva, A Koptyug, K Loza, O Prymak, M Epple, and R Surmenev. Surface modification of ti6al4v alloy scaffolds manufactured by electron beam melting. In *Journal of Physics: Conference Series*, volume 1145, page 012030. IOP Publishing, 2019.

[22] H Chung, FW Wehrli, JL Williams, and SD Kugelmass. Relationship between nmr transverse relaxation, trabecular bone architecture, and strength. *Proceedings of the National Academy of Sciences*, 90(21):10250–10254, 1993.

[23] Luiz Henrique Fonseca Damasceno, SILVIO RICARDO GUARNIERI Catarin, ANTÔNIO DORIVAL Campos, and HELTON LUIS APARECIDO Defino. Lumbar lordosis: a study of angle values and of vertebral bodies and intervertebral discs role. *Acta Ortop Bras*, 14(4):193–8, 2006.

[24] P Edwards and M Ramulu. Fatigue performance evaluation of selective laser melted ti–6al–4v. *Materials Science and Engineering: A*, 598:327–337, 2014.

[25] Firas El Masri, Emilie Sapin de Brosses, Khadija Rhissassi, Wafa Skalli, and David Mitton. Apparent young's modulus of vertebral cortico-cancellous bone specimens. *Computer Methods in Biomechanics and Biomedical Engineering*, 15(1):23–28, 2012.

[26] Emerging implant technologies. Eit plif cage. `http://www.macromed.co.uk/wp-content/uploads/2015/06/EIT_brochure_PLIFcage_en_rev-A.pdf`. Accessed: 2020-08-13.

[27] Zhechao Fan and Hongwei Feng. Study on selective laser melting and heat treatment of ti-6al-4v alloy. *Results in Physics*, 10:660–664, 2018.

[28] J Obedt Figueroa-Cavazos, Eduardo Flores-Villalba, José A Diaz-Elizondo, Oscar Martínez-Romero, Ciro A Rodríguez, and Héctor R Siller. Design concepts of polycarbonate-based intervertebral lumbar cages: finite element analysis and compression testing. *Applied bionics and biomechanics*, 2016, 2016.

[29] GE healthcare. Ge healthcare brochure composer patient reports. `http://www3.gehealthcare.de/~/media/documents/us-global/products/bone-health/brochures/gehealthcare-brochure_composer-patient-reports.pdf`. Accessed: 2019-10-30.

[30] JD Giallonardo, U Erb, KT Aust, and G Palumbo. The influence of grain size and texture on the young's modulus of nanocrystalline nickel and nickel–iron alloys. *Philosophical Magazine*, 91(36):4594–4605, 2011.

[31] Lorna J Gibson and Michael F Ashby. *Cellular solids: structure and properties*. Cambridge university press, 1999.

[32] FJ Gil, MP Ginebra, JM Manero, and JA Planell. Formation of α-widmanstätten structure: effects of grain size and cooling rate on the widmanstätten morphologies and on the mechanical properties in ti6al4v alloy. *Journal of Alloys and Compounds*, 329(1-2): 142–152, 2001.

[33] Rolando A Gittens, Rene Olivares-Navarrete, Zvi Schwartz, and Barbara D Boyan. Implant osseointegration and the role of microroughness and nanostructures: lessons for spine implants. *Acta biomaterialia*, 10(8):3363–3371, 2014.

[34] Vijay K Goel, Manohar M Panjabi, Avinash G Patwardhan, Andrew P Dooris, and Hassan Serhan. Test protocols for evaluation of spinal implants. *JBJS*, 88(suppl_2):103–109, 2006.

[35] Prashanth Konda Gokuldoss, Sri Kolla, and Jürgen Eckert. Additive manufacturing processes: Selective laser melting, electron beam melting and binder jetting—selection guidelines. *Materials*, 10(6):672, 2017.

[36] Haijun Gong, Khalid Rafi, Hengfeng Gu, GD Janaki Ram, Thomas Starr, and Brent Stucker. Influence of defects on mechanical properties of ti–6al–4 v components produced by selective laser melting and electron beam melting. *Materials & Design*, 86: 545–554, 2015.

[37] Haijun Gong, Venkata Karthik Nadimpalli, Khalid Rafi, Thomas Starr, and Brent Stucker. Micro-ct evaluation of defects in ti-6al-4v parts fabricated by metal additive manufacturing. *Technologies*, 7(2):44, 2019.

[38] He Gong, Ming Zhang, and Ling Qin. Mechanical properties of vertebral trabeculae with ageing evaluated with micro-ct. In *Advanced Bioimaging Technologies in Assessment of the Quality of Bone and Scaffold Materials*, pages 463–473. Springer, 2007.

[39] Stéphane Gorsse, Christopher Hutchinson, Mohamed Gouné, and Rajarshi Banerjee. Additive manufacturing of metals: a brief review of the characteristic microstructures and properties of steels, ti-6al-4v and high-entropy alloys. *Science and Technology of advanced MaTerialS*, 18(1):584–610, 2017.

[40] Henry Gray and Warren Harmon Lewis. *Anatomy of the human body*. Lea & Febiger, 1942.

[41] Robert F Heary, Naresh Parvathreddy, Sujitha Sampath, and Nitin Agarwal. Elastic modulus in the selection of interbody implants. *Journal of spine surgery*, 3(2):163, 2017.

[42] Dirk Herzog, Vanessa Seyda, Eric Wycisk, and Claus Emmelmann. Additive manufacturing of metals. *Acta Materialia*, 117:371–392, 2016.

[43] Shabnam Hosseini. Fatigue of ti-6al-4v. 2012.

[44] Fu J Hou, Susan M Lang, Susan J Hoshaw, David A Reimann, and David P Fyhrie. Human vertebral body apparent and hard tissue stiffness. *Journal of biomechanics*, 31 (11):1009–1015, 1998.

[45] Nikolas Hrabe, Ryan White, and Enrico Lucon. Effects of internal porosity and crystallographic texture on charpy absorbed energy of electron beam melting titanium alloy (ti-6al-4v). *Materials Science and Engineering: A*, 742:269–277, 2019.

[46] John W Hutchinson. Stresses and failure modes in thin films and multilayers. *Notes for a Dcamm Course. Technical University of Denmark, Lyngby*, 1, 1996.

[47] Sravisht Iyer, Blaine A Christiansen, Benjamin J Roberts, Michael J Valentine, Rajaram K Manoharan, and Mary L Bouxsein. A biomechanical model for estimating loads on thoracic and lumbar vertebrae. *Clinical biomechanics*, 25(9):853–858, 2010.

[48] Milan T Jovanović, Srđan Tadić, Slavica Zec, Z Mišković, and Ilija Bobić. The effect of annealing temperatures and cooling rates on microstructure and mechanical properties of investment cast ti–6al–4v alloy. *Materials & design*, 27(3):192–199, 2006.

[49] K Karami, A Blok, L Weber, SM Ahmadi, R Petrov, Ksenija Nikolic, EV Borisov, S Leeflang, C Ayas, AA Zadpoor, M Mehdipour, E Reinton, and V Popovich. Continuous and pulsed selective laser melting of ti6al4v lattice structures: effect of post-processing on microstructural anisotropy and fatigue behaviour. *Additive Manufacturing*, page 101433, 2020.

[50] Shima Karimi, Tirdad Nickchi, and Akram M Alfantazi. Long-term corrosion investigation of aisi 316l, co–28cr–6mo, and ti–6al–4v alloys in simulated body solutions. *Applied Surface Science*, 258(16):6087–6096, 2012.

[51] Ramji Karpagavalli, Anhong Zhou, Prithiviraj Chellamuthu, and Kytai Nguyen. Corrosion behavior and biocompatibility of nanostructured tio2 film on ti6al4v. *Journal of Biomedical Materials Research Part A: An Official Journal of The Society for Biomaterials, The Japanese Society for Biomaterials, and The Australian Society for Biomaterials and the Korean Society for Biomaterials*, 83(4):1087–1095, 2007.

[52] Dong-Soo Kim, Yong-Min Kim, Eui-Sung Choi, Hyun-Chul Shon, Kyung-Jin Park, Gee-Kang Park, Eun-Myung Lee, and Hu-Shan Cui. Shape and motion of each lumbar segment in normal korean adults. *Journal of the Korean Orthopaedic Association*, 43 (5):595–600, 2008.

[53] HS Kim and STS Al-Hassani. A morphological model of vertebral trabecular bone. *Journal of biomechanics*, 35(8):1101–1114, 2002.

[54] Tae-Yeon Kim, John E Dolbow, and Eliot Fried. Numerical study of the grain-size dependent young's modulus and poisson's ratio of bulk nanocrystalline materials. *International Journal of Solids and Structures*, 49(26):3942–3952, 2012.

[55] Youngmoo Kim, Eun-Pyo Kim, Young-Beom Song, Sung Ho Lee, and Young-Sam Kwon. Microstructure and mechanical properties of hot isostatically pressed ti–6al–4v alloy. *Journal of alloys and compounds*, 603:207–212, 2014.

[56] KM Knapp, GM Blake, TD Spector, and I Fogelman. Multisite quantitative ultrasound: precision, age-and menopause-related changes, fracture discrimination, and t-score equivalence with dual-energy x-ray absorptiometry. *Osteoporosis International*, 12(6): 456–464, 2001.

[57] C Anil Kumar, C Ashok Kumar, and KS Shivakumar Aradhya. Characteristics of singular stress field around a crack in a smart material–a finite element study.

[58] Shrawan Kumar. Posteroanterior spinal stiffness at t5, t10, and l3 levels in normal subjects. *PM&R*, 4(5):342–348, 2012.

[59] Open learn. Hot isostatic pressing (hip). `https://www.open.edu/openlearn/science-maths-technology/engineering-technology/manupedia/hot-isostatic-pressing-hip`. Accessed: 2020-01-31.

[60] Stefan Leuders, M Thöne, Andre Riemer, T Niendorf, T Tröster, HA a Richard, and HJ Maier. On the mechanical behaviour of titanium alloy tial6v4 manufactured by selective laser melting: Fatigue resistance and crack growth performance. *International Journal of Fatigue*, 48:300–307, 2013.

[61] JP Li, SH Li, CA Van Blitterswijk, and K De Groot. A novel porous ti6al4v: characterization and cell attachment. *Journal of Biomedical Materials Research Part A: An Official Journal of The Society for Biomaterials, The Japanese Society for Biomaterials, and The Australian Society for Biomaterials and the Korean Society for Biomaterials*, 73(2): 223–233, 2005.

[62] Y Li, J Zhou, P Pavanram, MA Leeflang, LI Fockaert, B Pouran, N Tümer, K-U Schröder, JMC Mol, H Weinans, et al. Additively manufactured biodegradable porous magnesium. *Acta biomaterialia*, 67:378–392, 2018.

[63] Zulei Liang, Zhonggang Sun, Wenshu Zhang, Shikai Wu, and Hui Chang. The effect of heat treatment on microstructure evolution and tensile properties of selective laser melted ti6al4v alloy. *Journal of Alloys and Compounds*, 782:1041–1048, 2019.

[64] Lindare Medical. Clia spinal cage. https://www.lindaremedical.co.uk/product/clia-spinal-cage/. Accessed: 2020-08-13.

[65] P Linez-Bataillon, F Monchau, M Bigerelle, and HF Hildebrand. In vitro mc3t3 osteoblast adhesion with respect to surface roughness of ti6al4v substrates. *Biomolecular engineering*, 19(2-6):133–141, 2002.

[66] Shunyu Liu and Yung C Shin. Additive manufacturing of ti6al4v alloy: A review. *Materials & Design*, 164:107552, 2019.

[67] JJ Lucas and PP Konieczny. Relationship between alpha grain size and crack initiation fatigue strength in ti–6al–4v. Technical report, Sikorsky Aircraft, Stratford, Conn., 1971.

[68] Lumitex. Spinal implants: Types, usage and options. https://www.lumitex.com/blog/spinal-implants. Accessed: 2020-08-13.

[69] G Lutjering and A Gysler. Fatigue–a critical review. *Titanium–Science and Technology.*, 4:2065–2083, 1984.

[70] Garrett J Marshall, W Joseph Young, Scott M Thompson, Nima Shamsaei, Steve R Daniewicz, and Shuai Shao. Understanding the microstructure formation of ti-6al-4v during direct laser deposition via in-situ thermal monitoring. *Jom*, 68(3):778–790, 2016.

[71] Hiroshige Masuo, Yuzo Tanaka, Shotaro Morokoshi, Hajime Yagura, Tetsuya Uchida, Yasuhiro Yamamoto, and Yukitaka Murakami. Influence of defects, surface roughness and hip on the fatigue strength of ti-6al-4v manufactured by additive manufacturing. *International Journal of Fatigue*, 117:163–179, 2018.

[72] Metal AM. German Additive Manufacturing company receives FDA clearance to supply spinal cages to US market. https://www.metal-am.com/german-additive-manufacturing-company-receives-fda-clearance/. Accessed: 2020-5-25.

[73] Lis Mosekilde. Sex differences in age-related changes in vertebral body size, density and biomechanical competence in normal individuals. *Bone*, 11(2):67–73, 1990.

[74] Lis Mosekilde. Age-related changes in bone mass, structure, and strength–effects of loading. *Zeitschrift für Rheumatologie*, 59(1):I1–I9, 2000.

[75] Yukitaka Murakami. *Metal fatigue: effects of small defects and nonmetallic inclusions*. Academic Press, 2019.

[76] Palla Murali, Tanmay K Bhandakkar, Wei Li Cheah, Mark H Jhon, Huajian Gao, and Rajeev Ahluwalia. Role of modulus mismatch on crack propagation and toughness enhancement in bioinspired composites. *Physical Review E*, 84(1):015102, 2011.

[77] Shariq Najeeb, Muhammad S Zafar, Zohaib Khurshid, and Fahad Siddiqui. Applications of polyetheretherketone (peek) in oral implantology and prosthodontics. *Journal of prosthodontic research*, 60(1):12–19, 2016.

[78] Magnus Neikter. *Microstructure and texture of additive manufactured Ti-6Al-4V*. PhD thesis, Luleå University of Technology, 2017.

[79] Magnus Neikter, A Huang, and X Wu. Microstructural characterization of binary microstructure pattern in selective laser-melted ti-6al-4v. *The International Journal of Advanced Manufacturing Technology*, 104(1-4):1381–1391, 2019.

[80] PATRICK HF Nicholson, XG Cheng, G Lowet, Steven Boonen, MWJ Davie, Jan Dequeker, and Georges Van der Perre. Structural and material mechanical properties of human vertebral cancellous bone. *Medical engineering & physics*, 19(8):729–737, 1997.

[81] H Oguma and T Nakamura. The effect of microstructure on very high cycle fatigue properties in ti–6al–4v. *Scripta Materialia*, 63(1):32–34, 2010.

[82] Orthopedics this week. 3d print this! `https://ryortho.com/2016/12/3d-print-this/`. Accessed: 2020-08-13.

[83] Material property data. Matweb. `https://matweb.com`. Accessed: 2020-04-18.

[84] Qichun Ran, Weihu Yang, Yan Hu, Xinkun Shen, Yonglin Yu, Yang Xiang, and Kaiyong Cai. Osteogenesis of 3d printed porous ti6al4v implants with different pore sizes. *Journal of the mechanical behavior of biomedical materials*, 84:1–11, 2018.

[85] Elizabeth J Samelson, Blaine A Christiansen, Serkalem Demissie, Kerry E Broe, Qiong Louie-Gao, L Adrienne Cupples, Benjamin J Roberts, Rajaram Manoharam, John D'Agostino, Thomas Lang, et al. Qct measures of bone strength at the thoracic and lumbar spine: the framingham study. *Journal of Bone and Mineral Research*, 27(3): 654–663, 2012.

[86] William J Sames, FA List, Sreekanth Pannala, Ryan R Dehoff, and Sudarsanam Suresh Babu. The metallurgy and processing science of metal additive manufacturing. *International Materials Reviews*, 61(5):315–360, 2016.

[87] Albert Schultz, Gunnar Andersson, R Ortengren, K Haderspeck, and A Nachemson. Loads on the lumbar spine. validation of a biomechanical analysis by measurements of intradiscal pressures and myoelectric signals. *The Journal of bone and joint surgery. American volume*, 64(5):713–720, 1982.

[88] Jan Schwerdtfeger, Robert F Singer, and Carolin Körner. In situ flaw detection by ir-imaging during electron beam melting. *Rapid Prototyping Journal*, 18(4):259–263, 2012.

[89] Alfred T Sidambe. Biocompatibility of advanced manufactured titanium implants—a review. *Materials*, 7(12):8168–8188, 2014.

[90] Marlo Simonelli, Yau Yau Tse, and Christopher Tuck. The formation of [alpha]+[beta] microstructure in as-fabricated selective laser melting of ti-6al-4v. *Journal of Materials Research*, 29(17):2028, 2014.

[91] Uwe Spetzger, Miles Frasca, and Stefan Alexander König. Surgical planning, manufacturing and implantation of an individualized cervical fusion titanium cage using patient-specific data. *European Spine Journal*, 25(7):2239–2246, 2016.

[92] Spine Health. What are cages and why is your surgeon putting one in your spine. `https://www.spine-health.com/blog/what-are-cages-and-why-your-surgeon-putting-one-your-spine`. Accessed: 2020-08-13.

[93] G Straffelini, V Fontanari, and A Molinari. True and apparent young's modulus in ferrous porous alloys. *Materials Science and Engineering: A*, 260(1-2):197–202, 1999.

[94] Stefan Sturm, Shiwei Zhou, Yiu-Wing Mai, and Qing Li. On stiffness of scaffolds for bone tissue engineering—a numerical study. *Journal of biomechanics*, 43(9):1738–1744, 2010.

[95] Taku Sugawara, Yasunobu Itoh, Yoshitaka Hirano, Naoki Higashiyama, and Kazuo Mizoi. Long term outcome and adjacent disc degeneration after anterior cervical discectomy and fusion with titanium cylindrical cages. *Acta neurochirurgica*, 151(4):303–309, 2009.

[96] Abdul Khadar Syed, Bilal Ahmad, Hua Guo, Thays Machry, David Eatock, Jonathan Meyer, Michael E Fitzpatrick, and Xiang Zhang. An experimental study of residual stress and direction-dependence of fatigue crack growth behaviour in as-built and stress-relieved selective-laser-melted ti6al4v. *Materials Science and Engineering: A*, 755: 246–257, 2019.

[97] Sarah Thelen, François Barthelat, and L Catherine Brinson. Mechanics considerations for microporous titanium as an orthopedic implant material. *Journal of Biomedical Materials Research Part A: An Official Journal of The Society for Biomaterials, The Japanese Society for Biomaterials, and The Australian Society for Biomaterials and the Korean Society for Biomaterials*, 69(4):601–610, 2004.

[98] M Thöne, S Leuders, A Riemer, T Tröster, and HA Richard. Influence of heat-treatment on selective laser melting products–eg ti6al4v. In *Solid freeform fabrication symposium SFF, Austin Texas*, 2012.

[99] Félix Tomé-Bermejo, Angel R Piñera, and Luis Alvarez. Osteoporosis and the management of spinal degenerative disease (ii). *Archives of Bone and Joint Surgery*, 5(6):363, 2017.

[100] Alexander R. Vaccaro. 3 things you need to know about spinal fusion recovery. `https://rothmanortho.com/stories/news-and-blog/3-things-you-need-to-know-about-spinal-fusion-recovery`. Accessed: 2019-10-30.

[101] Brecht Van Hooreweder, Yanni Apers, Karel Lietaert, and Jean-Pierre Kruth. Improving the fatigue performance of porous metallic biomaterials produced by selective laser melting. *Acta biomaterialia*, 47:193–202, 2017.

[102] Fabio Variola, Ji-Hyun Yi, Ludovic Richert, James D Wuest, Federico Rosei, and Antonio Nanci. Tailoring the surface properties of ti6al4v by controlled chemical oxidation. *Biomaterials*, 29(10):1285–1298, 2008.

[103] Bey Vrancken, Lore Thijs, Jean-Pierre Kruth, and Jan Van Humbeeck. Heat treatment of ti6al4v produced by selective laser melting: Microstructure and mechanical properties. *Journal of Alloys and Compounds*, 541:177–185, 2012.

[104] L Wagner. Mechanical surface treatments on titanium, aluminum and magnesium alloys. *Materials Science and Engineering: A*, 263(2):210–216, 1999.

[105] Fude Wang, Junfa Mei, Hui Jiang, and Xinhua Wu. Laser fabrication of ti6al4v/tic composites using simultaneous powder and wire feed. *Materials science and Engineering: A*, 445:461–466, 2007.

[106] Xiaojian Wang, Shanqing Xu, Shiwei Zhou, Wei Xu, Martin Leary, Peter Choong, M Qian, Milan Brandt, and Yi Min Xie. Topological design and additive manufacturing of porous metals for bone scaffolds and orthopaedic implants: A review. *Biomaterials*, 83:127–141, 2016.

[107] Thomas J Webster and Jeremiah U Ejiofor. Increased osteoblast adhesion on nanophase metals: Ti, ti6al4v, and cocrmo. *Biomaterials*, 25(19):4731–4739, 2004.

[108] WHO Scientific Group on Prevention and Management of Osteoporosis and World Health Organization. *Prevention and management of osteoporosis: report of a WHO scientific group*. Number 921. World Health Organization, 2003.

[109] Hans-Joachim Wilke, Peter Neef, Barbara Hinz, Helmut Seidel, and Lutz Claes. Intradiscal pressure together with anthropometric data–a data set for the validation of models. *Clinical Biomechanics*, 16:S111–S126, 2001.

[110] JL Woodman, JJ Jacobs, JO Galante, and RM Urban. Metal ion release from titanium-based prosthetic segmental replacements of long bones in baboons: A long-term study. *Journal of Orthopaedic Research*, 1(4):421–430, 1983.

[111] GQ Wu, CL Shi, W Sha, AX Sha, and HR Jiang. Effect of microstructure on the fatigue properties of ti–6al–4v titanium alloys. *Materials & Design*, 46:668–674, 2013.

[112] Su-Hua Wu, Yi Li, Yong-Quan Zhang, Xiao-Kang Li, Chao-Fan Yuan, Yu-Lin Hao, Zhi-Yong Zhang, and Zheng Guo. Porous titanium-6 aluminum-4 vanadium cage has better osseointegration and less micromotion than a poly-ether-ether-ketone cage in sheep vertebral fusion. *Artificial organs*, 37(12):E191–E201, 2013.

[113] Xinhua Wu, Jing Liang, Junfa Mei, C Mitchell, PS Goodwin, and W Voice. Microstructures of laser-deposited ti–6al–4v. *Materials & design*, 25(2):137–144, 2004.

[114] Bartłomiej Wysocki, Piotr Maj, Ryszard Sitek, Joseph Buhagiar, Krzysztof Kurzydłowski, and Wojciech Święszkowski. Laser and electron beam additive manufacturing methods of fabricating titanium bone implants. *Applied Sciences*, 7(7):657, 2017.

[115] Liu Xiao-bao, Li Xin, and Zhang Hai-feng. A new static strain measurement method of young's modulus based on the theory of the finite element. In *2017 9th International Conference on Modelling, Identification and Control (ICMIC)*, pages 516–520. IEEE, 2017.

[116] Wei Xu, M Brandt, S Sun, J Elambasseril, Q Liu, K Latham, K Xia, and M Qian. Additive manufacturing of strong and ductile ti–6al–4v by selective laser melting via in situ martensite decomposition. *Acta Materialia*, 85:74–84, 2015.

[117] Igor Yadroitsev and Ina Yadroitsava. Evaluation of residual stress in stainless steel 316l and ti6al4v samples produced by selective laser melting. *Virtual and Physical Prototyping*, 10(2):67–76, 2015.

[118] Katsuhisa Yamada, Manabu Ito, Toshiyuki Akazawa, Masaru Murata, Toru Yamamoto, and Norimasa Iwasaki. A preclinical large animal study on a novel intervertebral fusion cage covered with high porosity titanium sheets with a triple pore structure used for spinal fusion. *European Spine Journal*, 24(11):2530–2537, 2015.

[119] Ming Yan and Peng Yu. An overview of densification, microstructure and mechanical property of additively manufactured ti-6al-4v—comparison among selective laser melting, electron beam melting, laser metal deposition and selective laser sintering, and with conventional powder. In *Sintering techniques of materials*. IntechOpen, 2015.

[120] Xingchen Yan, Shuo Yin, Chaoyue Chen, Chunjie Huang, Rodolphe Bolot, Rocco Lupoi, Min Kuang, Wenyou Ma, Christian Coddet, Hanlin Liao, and Min Lui. Effect of heat treatment on the phase transformation and mechanical properties of ti6al4v fabricated by selective laser melting. *Journal of Alloys and Compounds*, 764:1056–1071, 2018.

[121] Thomas Zander, Antonius Rohlmann, and Georg Bergmann. Influence of ligament stiffness on the mechanical behavior of a functional spinal unit. *Journal of biomechanics*, 37(7):1107–1111, 2004.

[122] A Zargarian, M Esfahanian, J Kadkhodapour, and S Ziaei-Rad. Numerical simulation of the fatigue behavior of additive manufactured titanium porous lattice structures. *Materials Science and Engineering: C*, 60:339–347, 2016.

[123] Xiang-Yu Zhang, Gang Fang, Sander Leeflang, Amarante J Böttger, Amir A Zadpoor, and Jie Zhou. Effect of subtransus heat treatment on the microstructure and mechanical properties of additively manufactured ti-6al-4v alloy. *Journal of Alloys and Compounds*, 735:1562–1575, 2018.

[124] Y Zhou, U Erb, KT Aust, and G Palumbo. Young's modulus in nanostructured metals. *Zeitschrift für Metallkunde*, 94(10):1157–1161, 2003.

[125] JH Zuo, ZG Wang, and EH Han. Effect of microstructure on ultra-high cycle fatigue behavior of ti–6al–4v. *Materials Science and Engineering: A*, 473(1-2):147–152, 2008.

Appendices

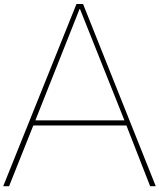

PLIF and XLIF drawings

See next page.

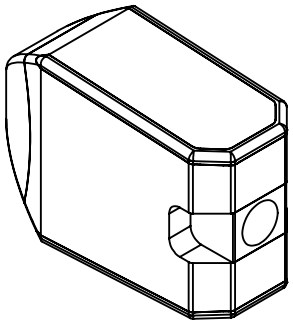

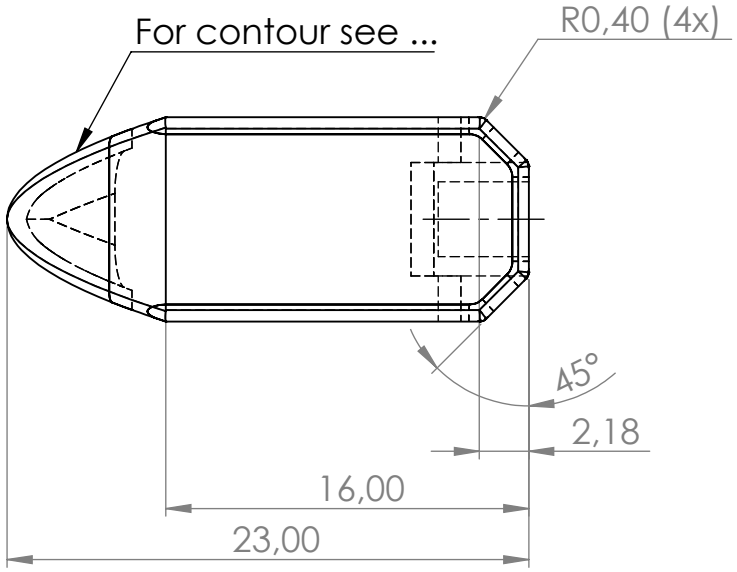

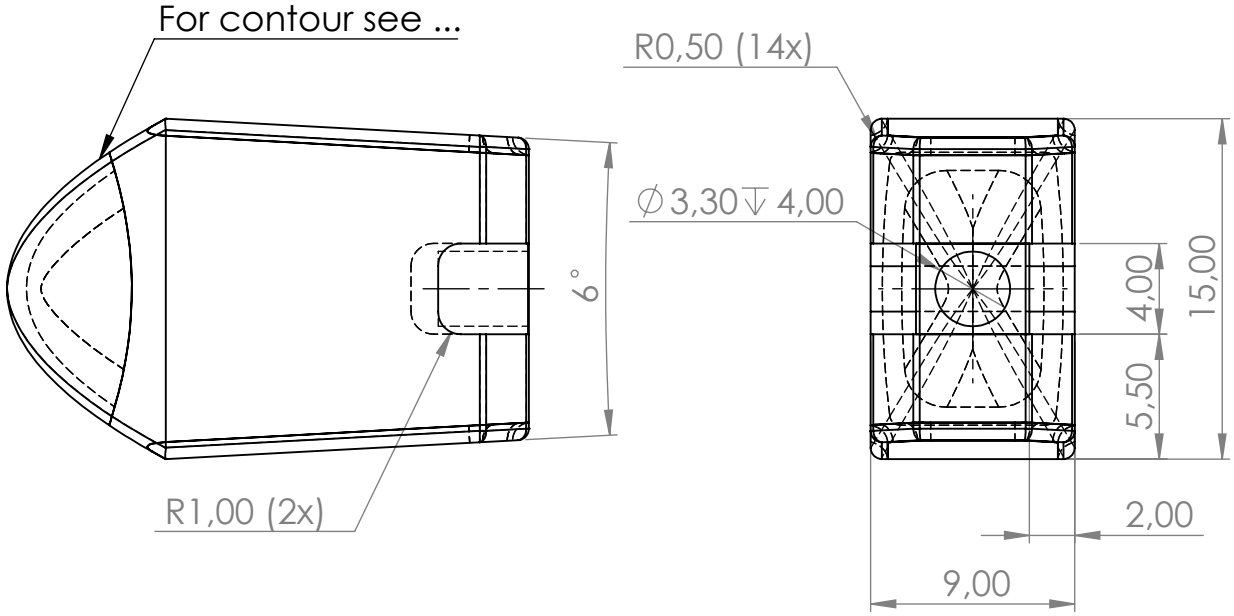

UNLESS OTHERWISE SPECIFIED: DIMENSIONS ARE IN MILLIMETERS SURFACE FINISH: TOLERANCES: LINEAR: ANGULAR:		FINISH:		DEBURR AND BREAK SHARP EDGES		DO NOT SCALE DRAWING	REVISION
	NAME	SIGNATURE	DATE				TITLE:
DRAWN							
CHK'D							
APPV'D							
MFG							
Q.A				MATERIAL:		DWG NO.	A4
						PLIF draw	
				WEIGHT:		SCALE:2:1	SHEET 1 OF 1

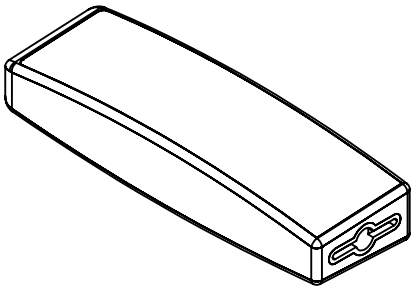

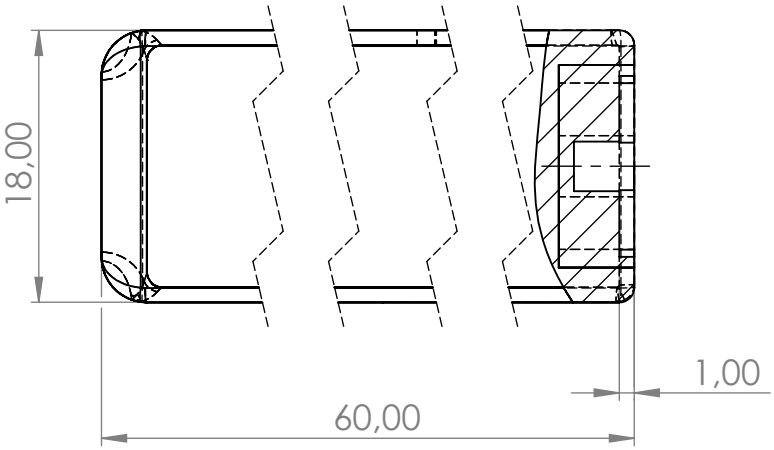

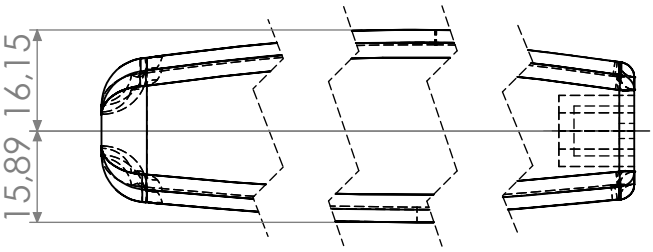

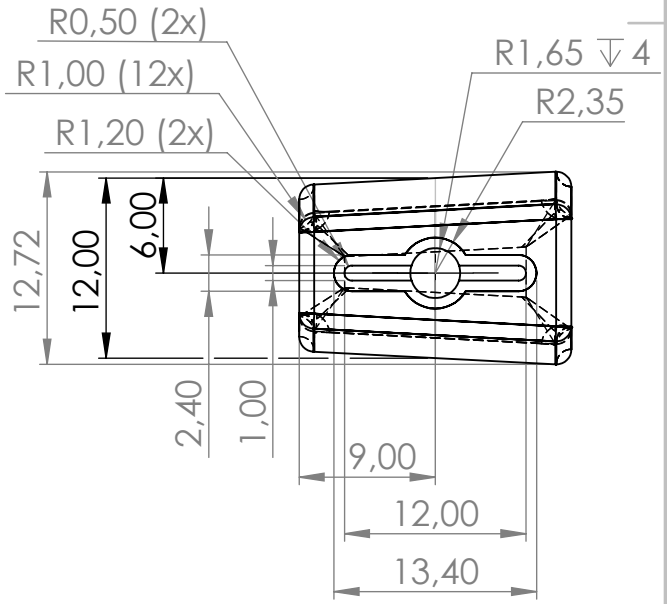

UNLESS OTHERWISE SPECIFIED: DIMENSIONS ARE IN MILLIMETERS SURFACE FINISH: TOLERANCES: LINEAR: ANGULAR:	FINISH:	DEBURR AND BREAK SHARP EDGES	DO NOT SCALE DRAWING / REVISION

	NAME	SIGNATURE	DATE
DRAWN			
CHK'D			
APPV'D			
MFG			
Q.A			

TITLE:

MATERIAL:

DWG NO. XLIF draw

A4

WEIGHT:

SCALE:1:1

SHEET 1 OF 1

B

XLIF implant

B.1. XLIF design

For the XLIF design no pre-existing design was available. The dimensions of the XLIF design are based on design limitations recommended in literature. The width of the implant is advised to be 18 or 22 mm, the height of the implant is advised to be 8, 10 or 12 mm and the length of the implant is advised to be 50, 55 or 60 mm. For the design produced in this report the height and length are taken to be 12 mm and 60 mm. The maximum values are taken here because the intended area for implantation is the lumbar area and taking the maximum values here will ensure a more universal fit. The width of the implant is taken to be 18 mm. Here the minimal value is taken, because during implantation the implant is inserted through a tube and in this case the width will determine the diameter of the tube. A smaller tube will be less invasive and will leave a smaller scar.

Similar to the PLIF design the angle between the top and the bottom of the implant will be 6° to ensure a good fit in between the L2 and L3 vertebrae. Finally, the top and bottom surface of the implant are designed to fit the shape of the surface of the vertebrae. The surface of the vertebrae will be slightly hollow as can be seen in Figure B.1. The angle found on the inferior end-plate of the L2 vertebrae is 171.3° and the angle of the posterior end-plate of the L3 vertebrae is 173.8°.

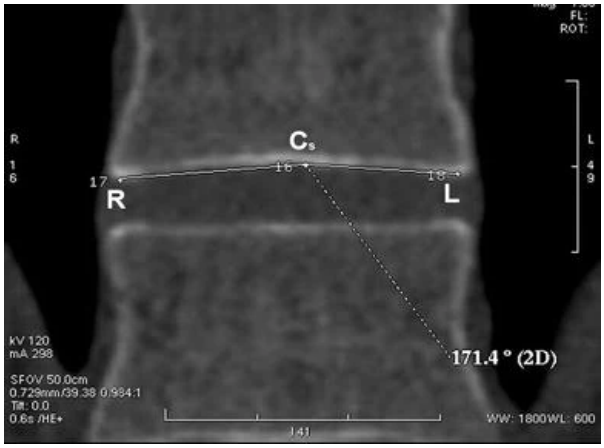

Figure B.1: Angle given between the most left and right point of the end-plate and the most concave point [20].

B.2. XLIF simulations

Exactly the same process is used to investigate the XLIF implant. There is only one difference, namely for spinal fusion only one XLIF implant is used compared to two PLIF implants. This results in the applied load for the quasi-static compression tests and the fatigue tests to be doubled. The applied loads are shown in Table B.1.

Table B.1: Group specific compressive and cyclic loads for the XLIF spinal cage.

	Compressive load	Cyclic load
Group 1	4000 N	1200 N
Group 2	4000 N	750N
Group 3	2000 N	1200 N
Group 4	2000 N	750 N
Group 5	1800 N	700 N

B.2.1. Quasi-static mechanical properties

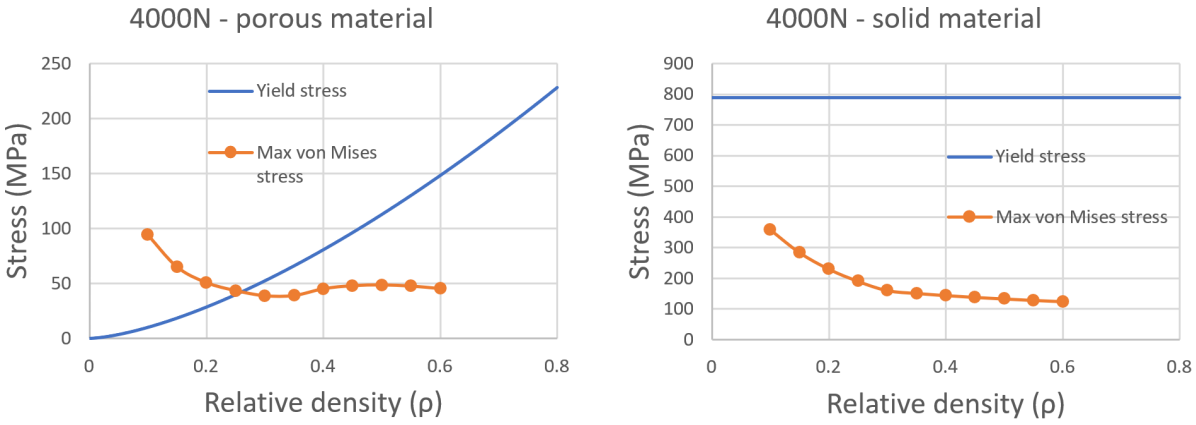

Figure B.2: Maximum von Mises stress at different relative densities loaded with 4000 N.

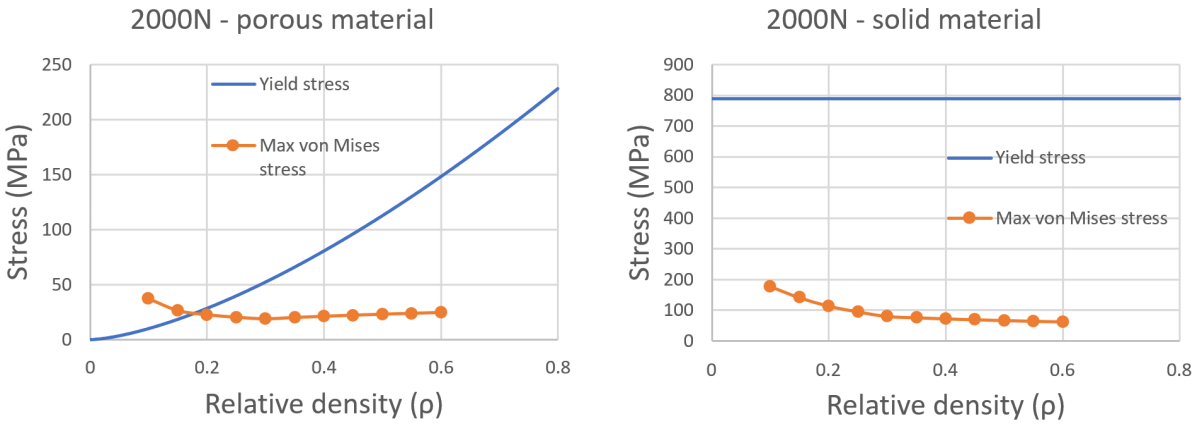

Figure B.3: Maximum von Mises stress at different relative densities loaded with 2000 N.

B.2.2. Fatigue properties

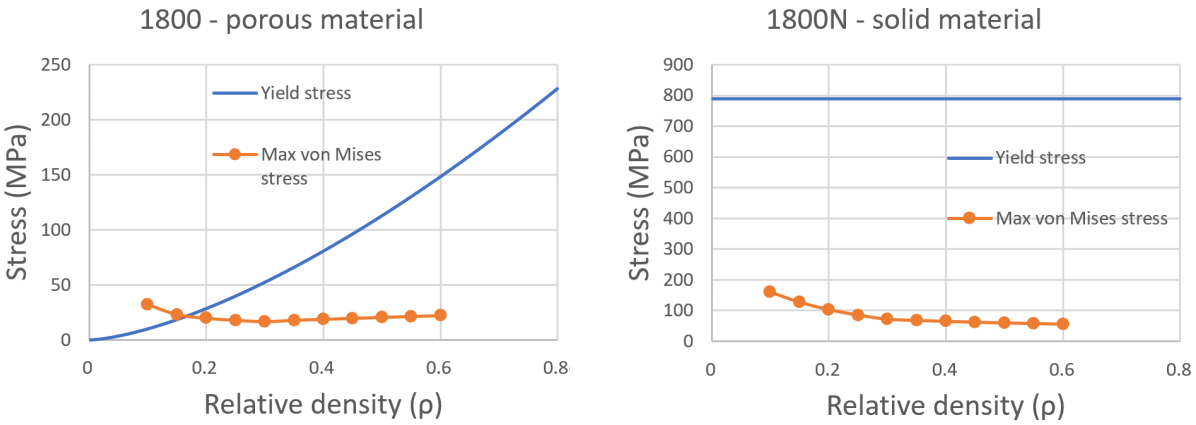

Figure B.4: Maximum von Mises stress at different relative densities loaded with 1800 N.

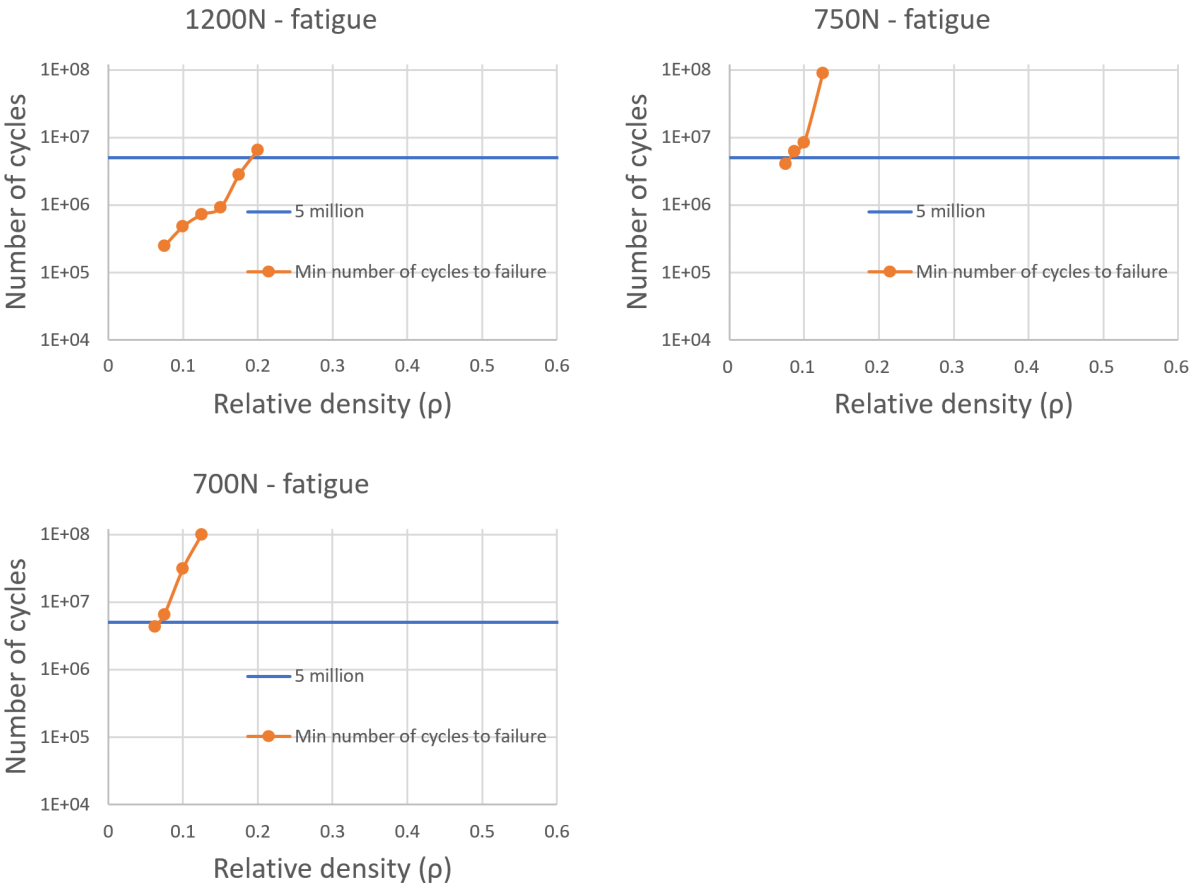

Figure B.5: Minimum number of cycles until failure for different relative densities and loads.

B.2.3. Group specific porosity

Table B.2: Group specific porosity range for the XLIF spinal cage.

	Porous material	Solid material	Fatigue life porous material	Porosity range
Group 1 4000N & 1200N	0 - 74%	-	0 - 81%	0 - 74%
Group 2 4000N & 750N	0 - 74%	-	0 - 92%	0 - 74%
Group 3 2000N & 1200N	0 - 82%	-	0 - 81%	0 - 81%
Group 4 2000N & 750N	0 - 82%	-	0 - 92%	0 - 82%
Group 5 1800N & 700N	0 - 84%	-	0 - 94%	0 - 84%

B.2.4. Group specific apparent Young's modulus

Table B.3: Group specific apparent Young's modulus for the XLIF spinal cage.

	Maximum porosity	apparent Young's modulus
Group 1 2000N & 600N	74%	3.17 MPa
Group 2 2000N & 375N	74%	3.17 MPa
Group 3 1000N & 600N	81%	2.19 MPa
Group 4 1000N & 375N	82%	1.63 MPa
Group 5 900N & 350N	84%	1.40 MPa

C

XRD results

See next page.

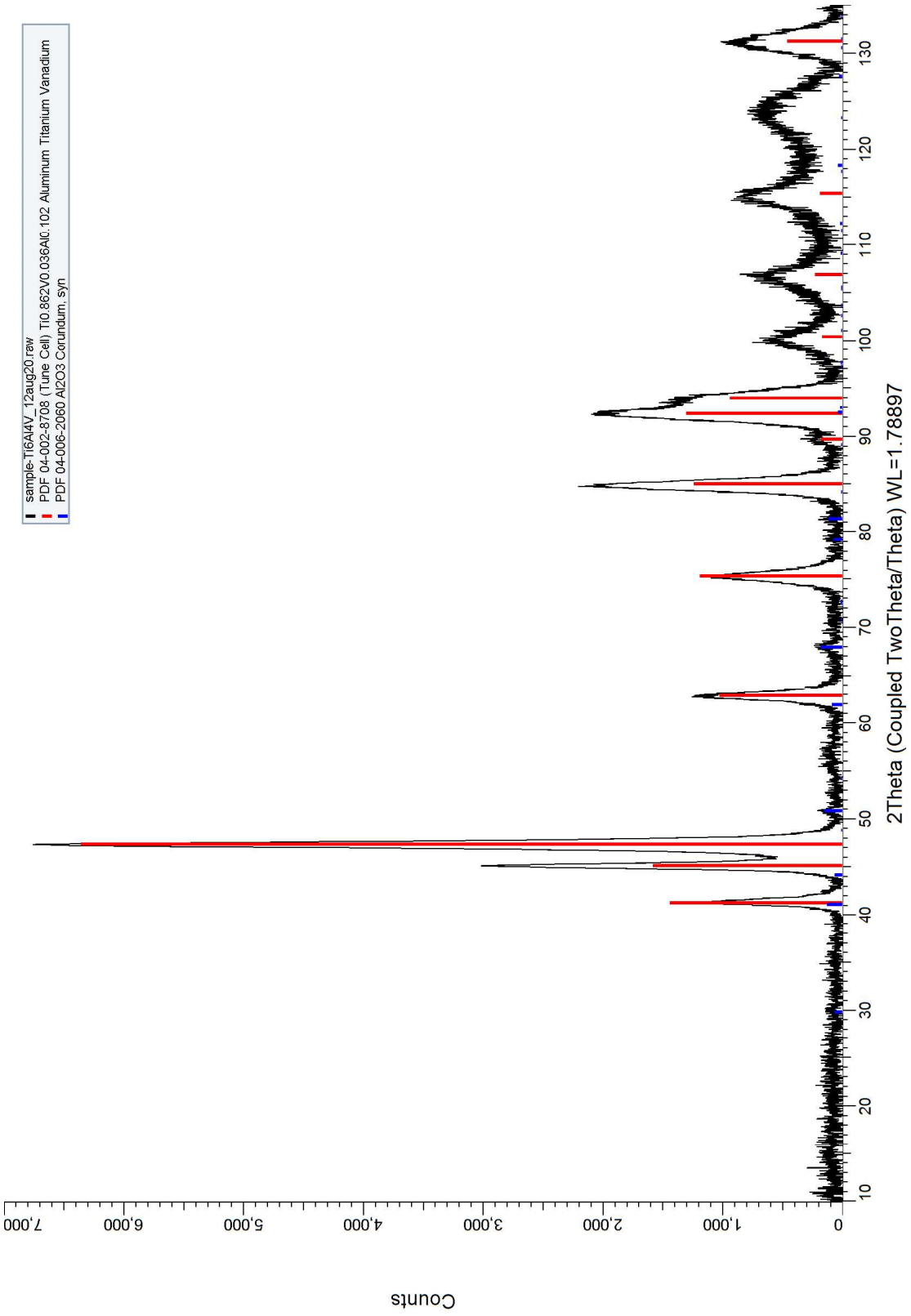

Figure 1 XRD pattern sample "Ti6Al4V "

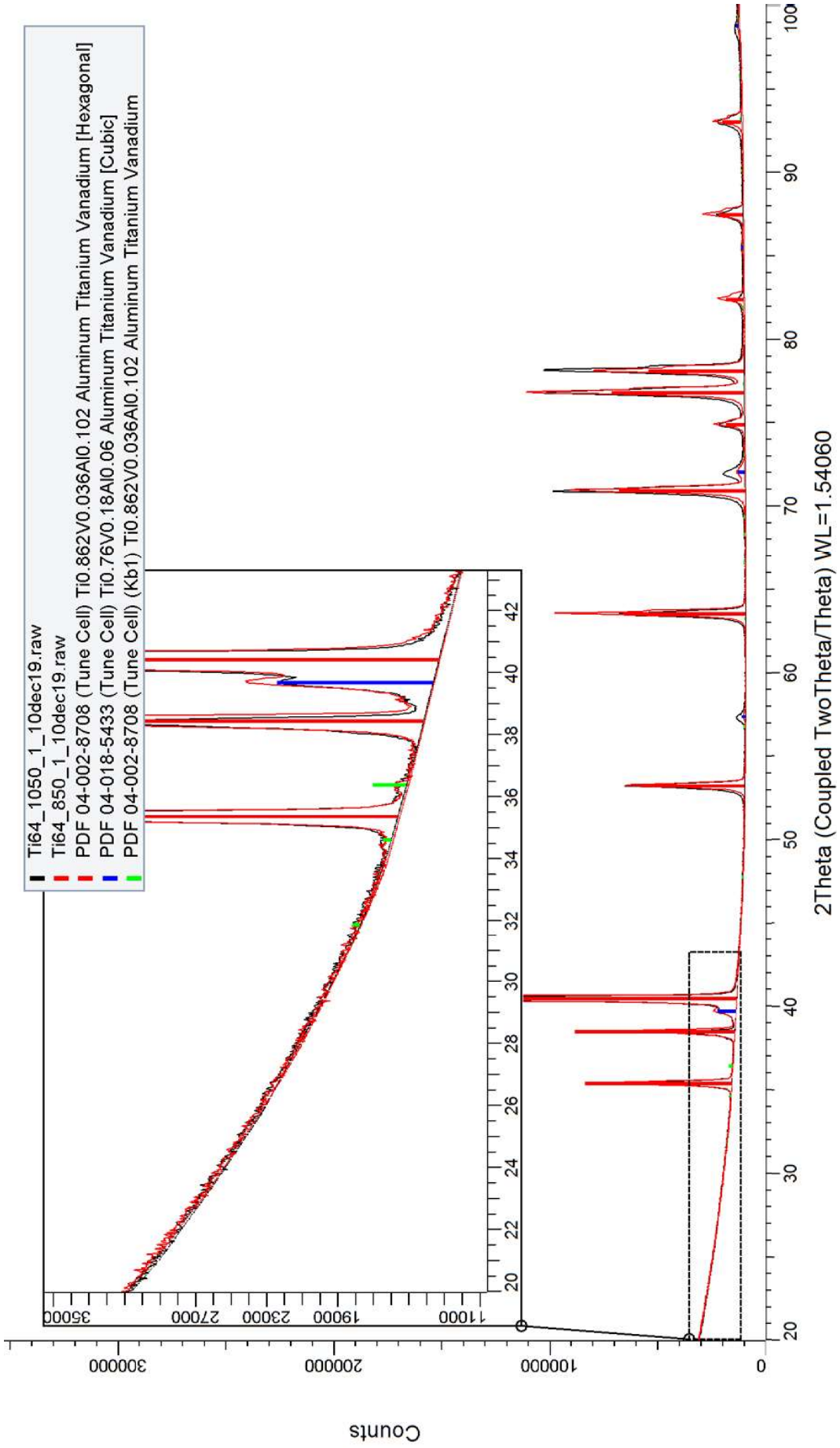

Figure 1. Overview of XRD patterns of all samples.

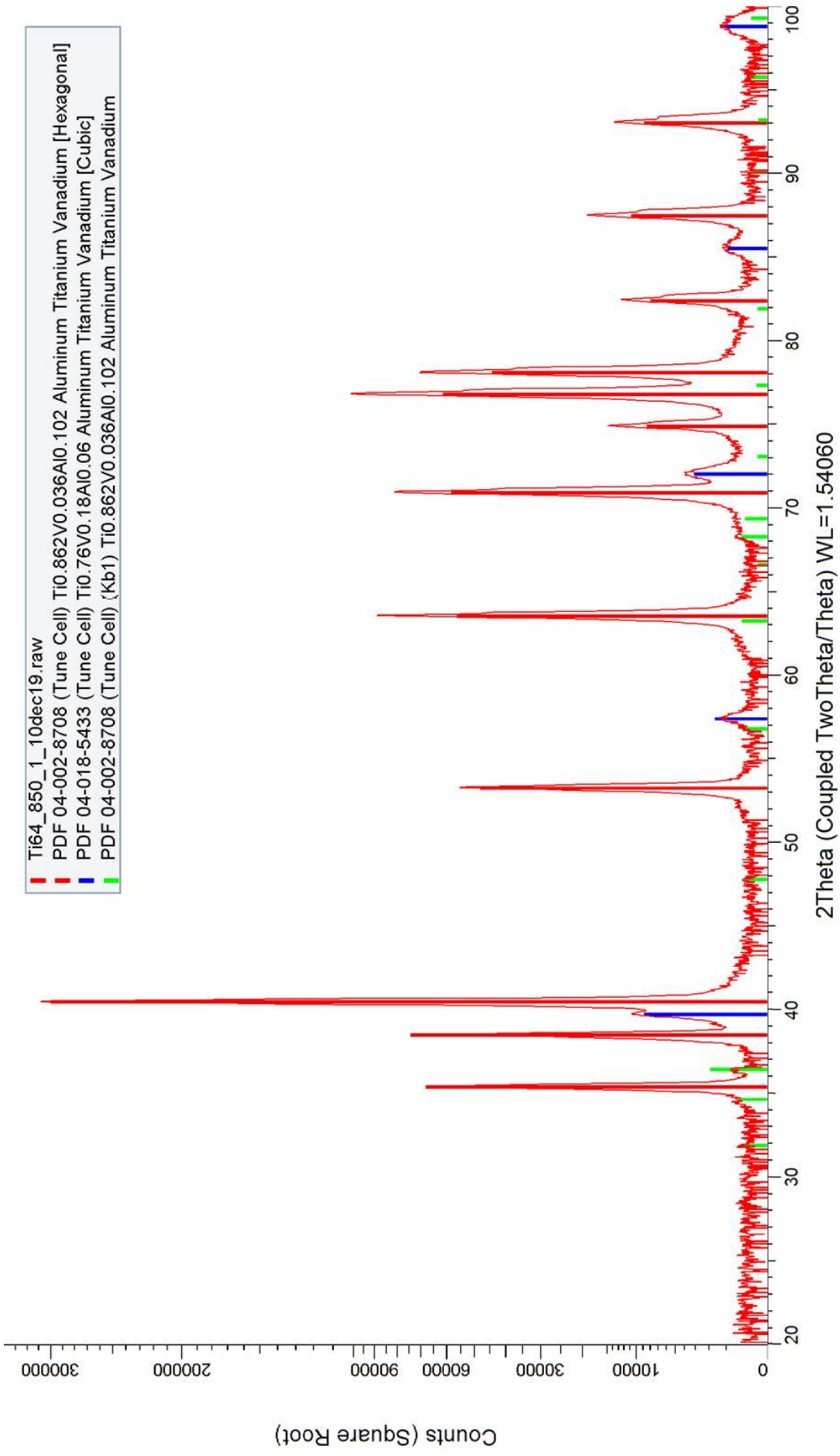

Figure 2. XRD pattern of sample 850 (background subtracted and square root scale).

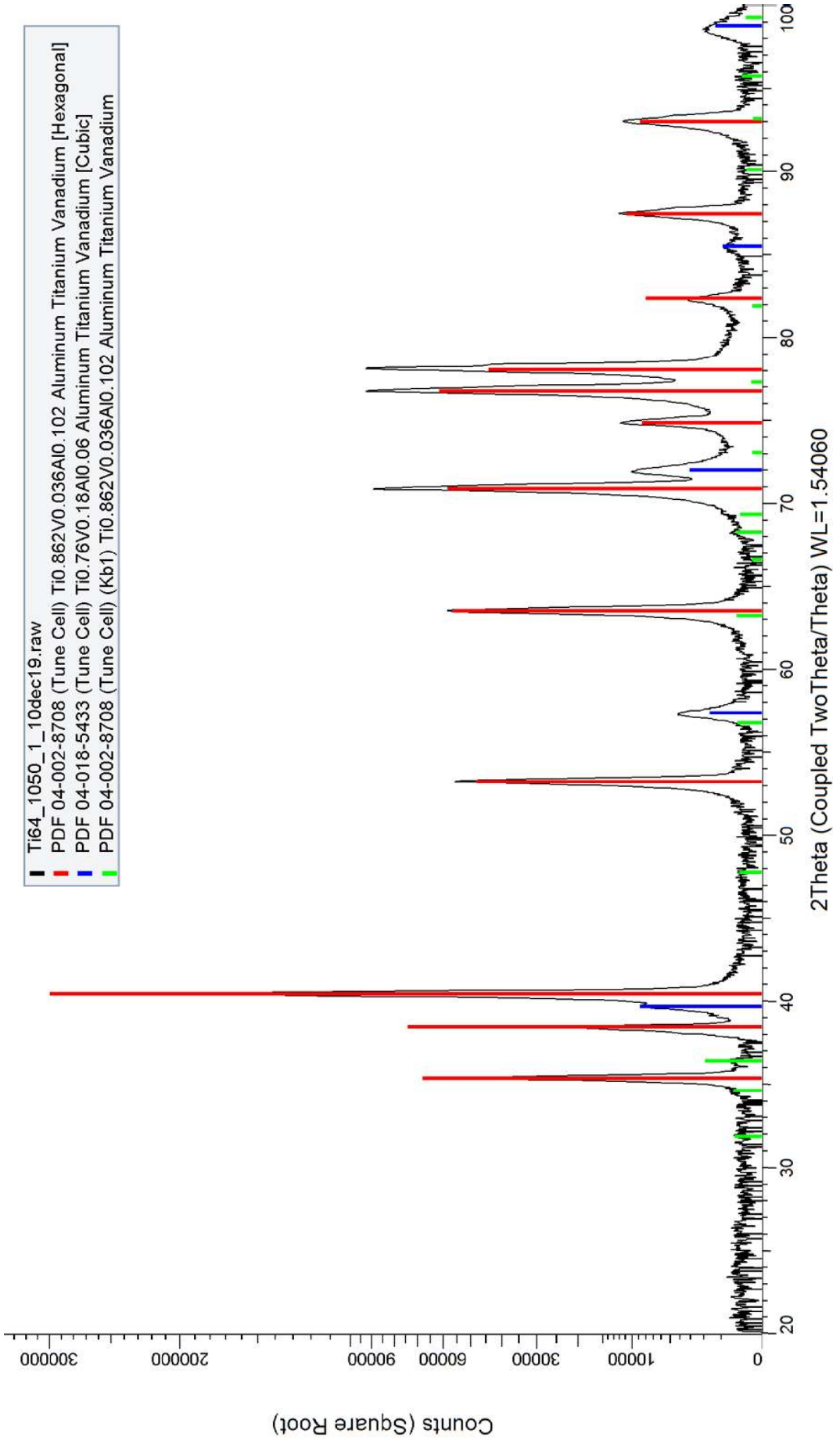

Figure 3. XRD pattern of sample 1050 (background subtracted and square root scale).